

NASA TM X-76

Declassified by authority of NASA
Classification Change Notices No. 113
and 6/22/67

NASA

DECLASSIFIED-AUTHORITY-MEMO.US:
2313. TAINÉ TO SHAUKLAS
DATED JUNE 15, 1967

TECHNICAL MEMORANDUM

X-76

AN EXPERIMENTAL PRESSURE-DISTRIBUTION INVESTIGATION OF
INTERFERENCE EFFECTS PRODUCED AT A MACH NUMBER OF 3.11
BY WEDGE-SHAPED BODIES LOCATED UNDER

A TRIANGULAR WING

By Lowell E. Hasel

Langley Research Center
Langley Field, Va.

N67-31960

(ACCESSION NUMBER)

(THRU)

116
(PAGES)1
(CODE)TMX-76
(NASA CR OR TMX OR AD NUMBER)01
(CATEGORY)

This material contains information affecting
the national defense of the United States within the meaning of the espionage laws, and its transmission or the revelation of its contents in any manner to an unauthorized person is prohibited by law.

NATIONAL AERONAUTICS AND SPACE ADMINISTRATION
WASHINGTON

October 1959

CONFIDENTIAL

NATIONAL AERONAUTICS AND SPACE ADMINISTRATION

TECHNICAL MEMORANDUM X-76

AN EXPERIMENTAL PRESSURE-DISTRIBUTION INVESTIGATION OF
INTERFERENCE EFFECTS PRODUCED AT A MACH NUMBER OF 3.11

BY WEDGE-SHAPED BODIES LOCATED UNDER

A TRIANGULAR WING*

By Lowell E. Hasel

SUMMARY

An investigation has been made of the interference effects which are produced at a Mach number of 3.11 by wedge-shaped bodies, simulating nacelles, located under a triangular wing. The effects of the basic variables of wedge angle and height, of internal air flow, and of modifications to the basic shapes were studied by measuring and integrating the pressures on the bodies and on the bottom wing surface. The results were analyzed both from nacelle considerations, where the base-pressure effects were neglected, and from volume considerations, where the base-pressure effects must be included in the drag. The data and discussion do not include the forces generated by the top surface of the wing since the body pressures were generally felt only on the lower wing surface.

Location of the basic body shapes under the wing did not produce a favorable interference effect on the maximum lift-drag ratio, even when the base-pressure drag was neglected. The maximum lift-drag ratio of the configuration with the smallest body was about equal to the value of the isolated wing, but the use of larger bodies resulted in lower maximum lift-drag ratios. Modification of the basic body shape by rounding the outboard edge or by maintaining a constant width over the rear portion of the body improved the maximum lift-drag ratio. Modification of the basic body shape to incorporate a supersonic nose inlet did not alter the interference characteristics of the basic shape. The agreement between the linear theory and experimental results was fairly good at low lift coefficients for the smaller basic bodies. As the body size and angle of attack increased, the discrepancies became larger.

When the bodies were considered from the viewpoint of drag per unit volume, and the base drag was included, none of the bodies were as efficient as an isolated, equal-volume, Haack body of fineness ratio 18.1.

* Title, Unclassified.

CONFIDENTIAL

INTRODUCTION

At both subsonic and supersonic speeds, the drag of an aircraft may be reduced by arranging or shaping the various components to utilize or to produce favorable pressure-interference effects. These effects at supersonic speeds have received considerable study. In one phase of the study, the concern has been with the effects of placing a body under a wing so that the positive pressure field of the body may produce lifting pressures on the wing. (See refs. 1 to 3.) The body might be the airplane fuselage, an external store, or a powerplant installation. For a powerplant installation made up of a series of engines, a rectangular shaped nacelle might be used. Configurations incorporating this type of engine installation are presented in references 4 and 5.

The interference effects produced by thin rectangular shaped bodies have been studied theoretically, and this study is discussed in reference 1. The effect on overall lift-drag characteristics of placing flat-sided, wedge-shaped bodies under a triangular wing was calculated by means of linear theory. This study was limited to plane-sided shapes which lent themselves to theoretical analysis. It was shown that at optimum conditions the drag of the wing-body combination may be less than that of the wing alone; however, the analysis neglected the effects of the skin-friction drag due to the body and of the base drag, and no correlation was made with experimental results.

It was the purpose of the present investigation to study experimentally the interference effects at a Mach number of 3.11 resulting from the location of wedge-shaped bodies (simulating engine-nacelle installations) under a triangular wing. The effects of the basic variables of wedge angle and height, air flow, and modification of the basic wedge shapes were investigated. Pressure distributions were measured on the wedge and lower surface of the wing at angles of attack from 0° to 6° . The Reynolds number was 21.9×10^6 based on the wing root chord. The pressure distributions were integrated to obtain the undersurface lift-drag characteristics for comparison with linear theory and with the wing-alone characteristics. The effects of skin friction and base drag are discussed. Since the bodies might be used for fuel cells or storage of equipment, the results are also discussed from the standpoint of volume considerations. The data and discussion do not include the forces generated by the top surface of the wing since the body pressures were generally felt only on the lower wing surface.

L
2
5
4

DECLASSIFIED

CONFIDENTIAL

3

SYMBOLS

b	span
c_o	root chord
C_L	lift coefficient
ΔC_L	lift-coefficient increment at a given angle of attack between any wing-body configuration and wing alone
C_D	drag coefficient
C_f	skin-friction coefficient
$(\Delta C_D)_v$	incremental-drag coefficient based on body volume raised to the two-thirds power
C_p	pressure coefficient
h	maximum body height
L/D	lift-drag ratio
R	Reynolds number
x	chordwise distance measured from wing apex
y	spanwise distance measured from vertical center line of wing
z	local height on body measured from surface of wing
α	angle of attack
δ	body or wedge half-angle
θ	angular position (see fig. 16(m))
$\beta = \sqrt{M^2 - 1}$	
Λ	wing-leading-edge angle of sweep
ϵ	shock-wave angle
$\eta = \beta \cot \Lambda$	

031712201030

CONFIDENTIAL

Subscripts:

B	body
b	base
p	pressure forces, excluding base pressure
f	total force, excluding base pressure
t	total force
w	wing
α	angle of attack
2D	two-dimensional

L
2
5
4

APPARATUS AND TESTS

Apparatus

The semispan model used in this investigation was mounted as shown schematically in figure 1 in a Langley gas dynamics laboratory blowdown jet having a test section which was 9 inches high and 10 inches wide. The wing had a root chord c_0 of 8.66 inches and a semispan of 5.00 inches. The wing surface to which the bodies were attached was flat and the angle of attack was measured with respect to this surface. The opposite surface had a wedge angle of 5° , measured in the stream direction. This angle was held constant to the trailing edge, as illustrated by the typical section detail. A wing trailing-edge extension of 1 inch was used during all of the tests in an attempt to minimize interaction between the blunt bases of the wing and body. The wing was mounted on a circular turntable which rotated to give the desired angle of attack. Boundary-layer thickness on the reflection-plane surface was minimized by use of a boundary-layer scoop and by keeping the distance from the scoop leading edge to the wing as short as possible.

The fourteen bodies which were studied are shown schematically in figure 2. The pertinent dimensions are tabulated and the dimensionless volumes of the half-bodies which were tested are given for all bodies except 8 and 9. For clarity the trailing-edge extension just discussed has been omitted in figure 2.

Bodies 1 to 7 were designed to investigate the effects of the basic variables of wedge angle and body height, and to provide data for

CONFIDENTIAL

DECLASSIFIED

CONFIDENTIAL

5

comparison with linear theory. The wedge half-angle δ was varied from 3° to 9° and the body height h/c_0 was varied from 0.0525 to 0.158 of the wing root chord. The smallest and largest of these bodies are shown in figure 2.

L
2
5
4

Bodies 8 and 9 were designed to determine the effects which internal air flow might have on the body characteristics. These bodies were geometrically similar to bodies 3 and 4 as far as wedge half-angle δ and body height h are concerned. An air inlet was located in the front of these bodies. The inlet was designed to capture a stream tube of air having a width of $0.0525c_0$ and a height equal to the body height h . The leading edge of the side of these bodies was located so as to be in the same plane as the theoretical, two-dimensional shock wave generated by bodies 3 and 4 at an angle of attack of 0° . The air captured by each inlet was directed through the reflection-plane surface and dumped into the atmosphere. Bodies 8 and 9 may be considered as inlet-nacelle installations operating at a mass-flow ratio of 1.

Bodies 10, 11, and 12 were designed to study the effects of altering the rear portions of the basic wedge-shaped bodies. The forward portions of these bodies were identical to body 4. On body 10 the bottom rear section was cut back along a Mach line to duplicate the type of body studied in reference 1. Bodies 11 and 12, respectively, had sections of constant width over the rear half- and quarter-body lengths as shown in figure 2.

Bodies 13 and 14 were designed to study the effects of replacing the square outboard corner by a circular or elliptical corner. These bodies were similar to body 4 in two aspects. The leading-edge half-angle was 6° and the volumes were made the same as that of body 4 by increasing the body heights. On body 13 the radius of the corner at every chordwise station was equal to the local width established by the 6° half-angle of the wedge. The same criterion was used to establish the major axes of the local ellipses which form the edge of body 14. In figure 2 the conical and elliptical portions of these bodies have been shaded for illustrative purposes.

A typical orifice installation is illustrated in figure 3. In general the orifices on both the wing and body were located in 11 chordwise stations. Several additional orifices were located near the wing leading edge to assist in determining the location of the shock wave produced by the body. A total of 47 orifices were located on the wing with varying numbers being covered by the different bodies. There were 43 to 57 orifices installed in the bodies. This relatively large number of body orifices, compared with that of the wing installation, was considered necessary to determine with sufficient accuracy the pressure distributions on the bodies. The base pressures on the bodies were measured by 2 to 4 orifices.

[REDACTED]

CONFIDENTIAL

Tests

The tests were conducted in a blowdown jet at a Mach number of 3.11. The stagnation pressure was 210 pounds per square inch absolute. The Reynolds number based on the length of the wing root chord was 21.9×10^6 . The angle of attack was varied from 0° to 6° . Model pressures were indicated on mercury manometer boards and were photographically recorded. All tests were conducted with free transition.

REDUCTION AND ACCURACY OF DATA

In an investigation of the type presented herein, the method of reducing the data may have an important effect upon the overall accuracy of the results. The reduction and accuracy of data are, therefore, discussed concurrently. The accuracy of the individual pressure coefficients C_p is about ± 0.003 . It is difficult to determine the overall accuracy of the integrated results. It is believed, however, that the following discussion indicates that the errors due to data-reduction techniques are small and that the overall accuracy is, therefore, good.

The general procedure for determining the normal-force coefficients was to fair and integrate the basic data at each chordwise station. These integrated results were then plotted against x/c_o and integrated to obtain the final results. A typical fairing of the basic data is shown in figure 3. These data were obtained at an angle of attack of 0° and a value of x/c_o of 0.798 on wing-body configuration 4. The symbols indicate the surfaces on which the pressures were obtained. It will be noted that one pressure from the side of the wedge (measured by orifice in row closest to wing surface) has been included in the data and that this wedge pressure is about equal to a nearby pressure measured on the wing surface. At other chordwise stations a wing pressure is usually not measured close to the wedge, and at these stations the wing pressure at the wing-body juncture is assumed to equal the pressure measured nearby on the vertical surface of the wedge. This assumption is more accurate over the rear 60 to 70 percent of the configuration where the wedge side pressures do not vary rapidly over the height of the wedge. It was assumed for fairing purposes that the pressure rise across the shock wave from the leading edge of the body was discontinuous. From boundary-layer considerations, one might expect the pressure rise to occur over a small but finite region, and the data indicate this fact to be true. It is not thought, however, that the assumption of a discontinuous rise results in any significant error in the final results. The location of the body shock wave was determined by the procedure which follows. The approximate location at each chordwise station was determined by comparing the pressures on the wing-body combinations with the pressures on the wing

CONFIDENTIAL

L
2
5
4

L
2
5
4

alone. A consideration of these approximate locations over the whole wing and the fact that the shock wave must be a continuous line enabled the shock position to be established within relatively narrow limits. Further refinements were possible by correlating the shock positions of the various bodies at the four angles of attack. The estimated shock location at $\alpha = 0^\circ$ for body 4 is shown in figure 3 to illustrate that when the shock is known to be between two orifices at each station the shock location is established within small limits. The pressure distribution outboard of the body shock was assumed to be equal to the wing-alone distributions. The fairing of the data is probably the least accurate over the forward 20 to 30 percent of each configuration because of the rapidly changing pressures and the limited number of orifices. As these data were faired, consideration was given to the theoretical pressures which would be expected in these regions. It is believed that these fairings are reasonably accurate and the resultant errors in the final data are small. Since the data were all faired from similar considerations, the relative errors between the configurations should be especially small.

The chord-force coefficients for all bodies except 13 and 14 were obtained by plotting as a function of x/c_o , fairing, and integrating the data obtained at the three body heights z/c_o . A second integration along the body height was performed to obtain the final force coefficients. For bodies 13 and 14 the forces on the curved surfaces were obtained by integrating first along a radial line and then around the curved surface. On the flat surfaces the integrations were made first along the body height and then along the body length.

The fairing of the chord-force data, as with the normal-force data, is less accurate over the forward part of the bodies because of the relatively rapidly changing pressures caused by the wing pressure field and the expansion around the corner of the body. The data were all faired to a value equal to the two-dimensional pressure at the leading edge of each body. It is thought that the accuracy of the chord-force data is the same as the accuracy of the normal-force data.

RESULTS AND DISCUSSION

General Remarks

Throughout the discussion the configurations incorporating bodies 1 to 7 are considered to be the basic configurations since these bodies include the primary variables of body height and half-angle. Comparisons with linear theory are limited to the results from these seven bodies. The remainder of the bodies are considered to be variations of the basic

CONFIDENTIAL

CONFIDENTIAL


shape, and their effects are discussed from this viewpoint. Bodies 9 to 14 are all variations of basic body 4. The characteristics of all configurations are discussed both from a consideration of engine-nacelle installations, in which case it is assumed that the engine exhaust occupies the base area so that the base-pressure drag is zero, and from a consideration that the bodies provide needed volume. In the latter case the base-pressure drag must be charged to the configurations. The data and discussion do not include the forces generated by the top surface of the wing. For most of the configurations the forces on this surface are independent of the body and, therefore, a consideration of these forces would not alter the general conclusions; however, the absolute values of the lift-drag ratio will be changed to some extent. For those configurations in which the body shock moves ahead of the wing leading edge under some test conditions, a consideration of the forces on the top surface of the wing would decrease the value of L/D . These conditions occur at an angle of attack of 6° for bodies 3, 4, and 5 and at angles of attack of 2° and above for bodies 6 and 7. The lift and drag coefficients obtained from the measured pressure distributions are given in table I.

Basic Data

General remarks.— The lifting pressure distributions measured on the bottom surface of the wing alone are presented in figure 4. The data were obtained at angles of attack varying from 0° to 6° and at 11 chordwise stations. The pressure distributions are generally faired through the data points although some inconsistency in data fairing results. This fairing was used to facilitate comparison with data from the wing-body configurations in later figures.

The pressure distributions measured on the lower lifting surfaces of the wing-body configurations are presented in figures 5 to 13. The data have been grouped in the figures to illustrate the effects of various changes in body shape on the pressure distributions. The effects of the basic body variables of wedge height h/c_o and wedge half-angle δ are illustrated in figures 5 to 7. Figures 8 to 13 illustrate the effects of modifying the basic body shapes. All of these modifications, excepting body 8, are based on body 4. The pressure distributions presented in figures 5 to 13 are based on pressures measured on the sides of the bodies as well as pressures measured on the bottom surfaces of wing and body. A detailed discussion of the origin of the data and method of fairing is presented in the section entitled "Reduction and Accuracy of Data." The basic pressure distributions are discussed herein in only a general manner. Details of the distributions are not considered.

The body orifices on configuration 5 were not located in the same chordwise stations as the wing orifices. The body data presented in figure 6 for configuration 5 were, therefore, obtained from faired curves.



DECLASSIFIED

No pressure distributions are presented for the bottom surface of body 7 (fig. 7) because of inconsistencies in the measured pressures. These inconsistencies are believed to have been caused by a localized, small air leak at the junction of the body and splitter plate. This leak did not significantly affect the pressures on the wing or side of the body. The integrated pressure forces for configuration 7 were obtained by assuming that the pressure distributions on the bottom surfaces of bodies 6 and 7 were identical. The resultant error in the pressure forces should be small since the pressure distributions on the bottoms of the bodies were affected very little by body height (figs. 5 and 6).

The shock locations from the data for bodies 1 to 7 are shown in figure 14. The front portions of bodies 10, 11, and 12 are the same as body 4 and the shock locations are, therefore, the same. A study of the data from bodies 13 and 14 did not indicate any change in shock location from that of body 4 although the heights of bodies 13 and 14 and the curved edges might have been expected to produce some changes. For bodies 8 and 9 the shock waves were slightly outboard from the shock waves of bodies 3 and 4, respectively. This location of the shock waves would be expected because the origin of the shock wave was moved outboard from the wing center line.

Lifting pressure distributions for bodies 1 through 7.- The data presented in figures 5, 6, and 7 indicate the effects which the wedge-shaped bodies have on the wing pressure distributions. Near the wing apex the pressures are a function of the body half-angle. Farther back on the wing the pressures decrease significantly since the body heights are not sufficient to maintain a two-dimensional flow field over the wing. The magnitude of the pressure decrease is larger for the smaller body heights, as would be expected. The interference pressure rise on the bottom of the body is smaller than on the wing and appears to be independent of the body height. Near the edge of the body the pressures on the bottom surface become more negative, probably because of an over-expansion around the square edges of the bodies. It may be noted in figure 12 that the overexpansion of pressures does not occur on body 13, which has the rounded edge.

Interference lift coefficients of bodies 1 to 7.- The lift coefficients produced at an angle of attack of 0° by bodies 1 to 7 are given at the top of figure 15. These values vary from 0.0077 for body 1 to 0.0532 for body 7. (At $\alpha = 4^\circ$ the lift coefficient of the isolated wing is 0.0545.) The average interference-lift coefficients over the angle-of-attack range ($\Delta C_{L,p,average}$) are from 0.001 to 0.005 higher than the values at $\alpha = 0^\circ$. The variation of the interference lift with body height h/c_0 is due to the fact that none of the body heights were large enough to produce completely two-dimensional flow on the wing. The

CONFIDENTIAL

height of body 7 ($\frac{h}{c_o} = 0.158$), for example, was about 39 percent of the

two-dimensional height (based on the Mach angle of the flow after the 9° compression). It is of interest to examine (fig. 15) the variation with body height of the ratio of the measured lift coefficients at 0° angle of attack and a calculated lift coefficient based on the two-dimensional pressure rise ($C_{p,2D}$) created by the various wedge half-angles. This two-dimensional pressure was assumed to act on all the wing and body lifting surfaces behind the wedge shock wave. Over the experimental range of h/c_o the measured lift varies almost linearly with

h/c_o . At larger body heights than $\frac{h}{c_o} = 0.158$ the rate of increase of the measured lift probably decreases significantly for $\delta = 3^\circ$ and to a smaller degree for $\delta = 6^\circ$ since at $\frac{h}{c_o} = 0.158$ these bodies are less than 50 percent of the two-dimensional heights but have already developed a larger portion of the two-dimensional lift. At a given value of h/c_o the bodies develop a smaller percentage of the two-dimensional lift as δ increases. It thus appears that the interference pressures are relieved relatively faster by three-dimensional effects as the body half-angle increases.

Lifting pressure distributions and interference-lift coefficients of modified bodies.- Modification of bodies 3 and 4 to provide an air inlet at the nose of bodies 8 and 9 does not appear to significantly affect the pressure distributions over the rear portion of the wing (figs. 8 and 9). This similarity of the pressure distributions is, in part, due to the fact that the leading edges of the sides of bodies 8 and 9 were located in the plane of the theoretical two-dimensional shocks produced by bodies 3 and 4. Over the forward portion of the wing the pressure distributions created by bodies 8 and 9 differ from those of bodies 3 and 4 because the regions of two-dimensional flow created by the bodies start in different locations.

The shapes of bodies 10, 11, and 12 were identical to body 4 back to values of x/c_o of 0.682, 0.50, and 0.75, respectively. The pressure distributions over the major portions of the wing should, therefore, be the same for the four configurations (figs. 10 and 11). The expansion on the bottom of body 10 appears to be felt over the inboard section of the wing at $\frac{x}{c_o} = 0.971$. This expansion results in a negative lift on

the rear of the body such that the overall lift coefficient at each angle of attack is about 0.010 less than for body 4. The expansions produced by the sides of bodies 11 and 12 affect the wing pressures as shown in figure 11. These expansion fields reduce the lift coefficients by about 0.010 and 0.004, respectively, over the angle-of-attack range.

L
2
5
4

The pressure distributions which are produced by bodies 13 and 14 (figs. 12 and 13) are quite similar to those of body 4. At the forward station, bodies 13 and 14 produce slightly higher pressures, probably because of the slightly greater heights. Over the inboard rear stations the wing pressures are less than with body 4. This effect probably is obtained because of the rounded corners. On the bottom of body 13 the reduction of pressure which occurred near the edge of body 4 appears to have been eliminated. The interference lifts of these two bodies are from 0.002 to 0.006 higher than for body 4.

Pressure distributions on the sides of the bodies.- The pressures on the side surfaces of the bodies are presented in figure 16. In general, the pressures were measured at three heights z/c_o on the sides of the bodies, and the pressures are plotted as a function of x/c_o . Portions of the surfaces of bodies 13 and 14 were curved. For these two bodies the pressures on the curved surfaces have been plotted as a function of angular position and on the flat surfaces as a function of z/c_o for each of the 11 chordwise stations (figs. 16(m) to 16(t)). The pressures change rapidly near the front of all the bodies because of the effects of the wing flow field and the expansion around the corner of the body. At the body leading edge the measured pressure coefficients should be equal to the two-dimensional, calculated values of 0.039, 0.086, and 0.142 for the body half-angles of 3° , 6° , and 9° , respectively. The pressures are relatively uniform over the rear half of each body except for bodies 10, 11, and 12 which have abrupt changes of shape. On bodies 8 and 9 it was impossible to locate orifices near the leading edge because of the internal air passages. The pressure distributions in these regions have been estimated by a consideration of the wing pressure field and the expansion field around the corner of the body.

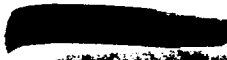
Comparison of Experimental Results With Linear Theory

Wing alone.- The comparison of the experimental lift-drag variation on the bottom surface of the wing alone with the variation predicted by linear theory is presented in figure 17. The experimental increase of drag with lift was less than predicted by linear theory. These differences, however, are small. At a lift coefficient of 0.05 the measured drag is about 0.0003 less than the calculated drag. This drag reduction is due to the fact that the variation of the forces with angle of attack is greater than predicted by the linear theory. The reason for the difference is evident in figure 4 where the experimental and linear-theory pressure distributions may be compared at the typical x/c_o stations of 0.278 and 0.971. The experimental results show the same variation with spanwise location as the theoretical results out to the location of the free-stream Mach angle originating from the wing apex. Outboard of this point the linear theory predicts a constant pressure, but the

experimental results show a continuously increasing pressure. It is these large increases in outboard pressures which are primarily responsible for the larger forces at a given angle of attack.

Wing-body configurations.- This discussion of the wing-body configurations is limited to the results obtained from the configurations with bodies 1 to 7 since these bodies are amenable to analysis by linear theory and the results indicate the effects of the basic variables of body height and body half-angle. The equations used for the calculations are presented in appendix A. In these equations it is assumed that the body pressures are felt only on that portion of the wing enclosed by the Mach lines from the apex of each body; whereas, for some configurations at angles of attack, the body shock waves move ahead of the wing leading edge. A comparison of the experimental and calculated results at an angle of attack of 0° is presented in figure 18, where $C_{L,p}$ and $C_{D,p}$ are each plotted as a function of body height h/c_0 . As would be expected, the forces increase as the body height and half-angle become larger. The experimental lift values (fig. 18(a)) are from 20 to 30 percent higher than the theoretical values for all bodies except that at $\frac{h}{c_0} = 0.105$, where the increase is only about 15 percent. The drag results (fig. 18(b)) indicate that at small body angles the linear theory provides acceptable accuracy. With $\delta = 6^\circ$, the experimental values of drag are about 0.0003 higher than calculated values. At $\delta = 9^\circ$ the differences are appreciably larger. It must be remembered, of course, that the larger bodies violate the small-disturbance assumptions of the linear theory. At $\delta = 9^\circ$ the two-dimensional pressure rise at the body apex is 0.142, which is about 33 percent larger than predicted by linear theory, and both the lift and drag forces might, therefore, be expected to be larger than the calculated forces. Another factor contributing to the larger lift coefficients, as previously mentioned, is the fact that the body pressures are felt over a larger portion of the wing surface than is assumed in linear theory.

The experimental and calculated variations of drag coefficient with lift coefficient are compared over the angle-of-attack range in figure 19. The unlabeled ticks and symbols in figure 19 denote conditions at angles of attack of 2° and 4° . At values of lift at angles of attack near 0° , the drags are equal to or larger than those calculated. The differences between the calculated and experimental results are larger for the larger bodies. As the lift increases, the drags become less than the calculated values. This trend is similar to the trend for the wing alone (fig. 17). At the higher angles of attack the measured forces are considerably larger than the calculated values.



Effects of Bodies on Lift-Drag Ratio

The variation of lift-drag ratio with lift coefficient is presented in figure 20 for all the wing-body configurations. Three curves are presented for most configurations. The curve labeled $(L/D)_p$ includes only pressure forces on the wing lower surface and forebody, $(L/D)_f$ includes the pressure forces and a skin-friction drag on the corresponding surfaces, $(L/D)_t$ includes the previous forces and the measured base-pressure drag. The skin-friction drag is based on a turbulent skin-friction coefficient of 0.0013, which is a typical value for a large, bomber-type aircraft ($R = 80 \times 10^6$). For the configuration with body 10 the pressures on the closing surface of the body were considered to be a part of the forebody pressures; therefore, no $(L/D)_f$ is presented in figure 20(j). $(L/D)_t$ has been omitted for nacelle configurations 8 and 9 since the base area would be filled by a jet exhaust. The variation of $(L/D)_f$ for the wing alone has been included in figure 20 for purposes of comparison.

It is of interest to first compare the performance of the seven basic wing-body configurations with the wing-alone configuration, while considering only the pressures on the wing and forebody. This comparison may be conveniently made by the use of figure 21. It is apparent from figure 21 that, at typical operating lift coefficients (about 0.05 since the lift of only the lower wing surface is involved), only the configurations with the smaller bodies (1, 2, and 3) equal the performance of the isolated wing, and none of these three configurations possess characteristics substantially superior to the isolated wing, even though the effects of the additional body skin friction have been neglected. The maximum reduction of drag is about 0.0003.

When the skin friction and base drag are considered, none of the basic wing-body configurations has a maximum lift-drag ratio equal to that of the lower surface of the isolated wing. This fact is shown in figure 22, where the maximum lift-drag ratios are presented as a function of body height. A turbulent skin-friction coefficient of 0.0013 was used in preparing the figure. Two sets of curves are included to illustrate the effect of base pressure. When the nacelle application is

considered (no base drag), the smallest body ($\delta = 3^\circ$; $\frac{h}{c_o} = 0.0525$) has a maximum lift-drag ratio of 12.1, which is essentially the same as that of the isolated wing. As the half-angle or height increases, the maximum lift-drag ratio decreases appreciably. For configuration 7 the maximum value is 5.9. The trend of curves seems to indicate that it may be possible to exceed the maximum lift-drag ratio of the isolated wing by use of bodies which have a small height and a small angle. The favorable increment, however, is probably small. These small bodies might be

CONFIDENTIAL


considered to produce the same effect as wing camber. From a practical point of view, it would appear difficult to obtain an installation where the nacelle height was less than 4 to 5 percent of the wing root chord unless the airplane is very large or the engines are partly buried in the wing. The maximum lift-drag ratio is reduced by 2 to 3 units (fig. 22) when the base pressure force is taken into account.

The lift coefficients corresponding to the data of figure 22 are presented in figure 23. As the maximum lift-drag ratio decreases, the corresponding lift coefficient increases. It is probable that for some of the larger basic configurations the maximum lift-drag ratio could not be utilized because of the high lift values.

The effects of modifying bodies 3 and 4 to represent air inlets were studied with bodies 8 and 9 (fig. 2). These bodies captured the full stream tube ahead of the body opening; therefore, the shock wave producing the interference pressure fields originated at the cowl side lip. As previously mentioned, the cowl side lip lay in the plane of the two-dimensional, theoretical shock wave produced by bodies 3 and 4. The results presented in figure 24 indicate that the modifications just described had no measurable effect on the interference characteristics of the basic bodies. It thus appears that the interference effects of rectangular nacelles which operate at a mass-flow ratio of 1 may be simulated by similar bodies without air flow. As the width of the air inlet becomes greater, it is possible that the degree of simulation may decrease.

The effects of replacing the square outboard corner of body 4 with a circular or elliptical corner are shown in figure 25 where the lift-drag ratios of configurations 4, 13, and 14 are plotted as a function of the lift coefficient. For either a nacelle or a volume installation, the modified corner increases the maximum lift-drag ratio. The increments are larger for the nacelle application (no base drag). For this case the circular edge shape increases the maximum lift-drag ratio from 8.7 for configuration 4 to 9.8. If the comparison is made at a constant body height of $0.12c_o$, the lift-drag ratio is increased from 8.3 to 9.8. (See fig. 22.) The increase in performance obtained with body 13 is partly due to the fact that the frontal area of the body is less than for body 4, and also the pressures over the rear portion of the body are less than for body 4. The pressure reduction may be seen by comparing figures 16(d) and 16(m) to 16(p).

The results of other modifications to body 4 are shown in figure 26. For a nacelle installation, small gains in maximum lift-drag ratio may result from maintaining a constant width over the rear portions of the body (bodies 11 and 12). These increments are small when compared with the results of rounding the outboard edge of the nacelle (body 13). For a volume installation, reduction of the maximum body width results in a



significant increase in maximum lift-drag ratio, primarily because the base drag is reduced. Removing the bottom of the basic body along a Mach line (body 10) improves the lift-drag ratio $(L/D)_t$ of the basic body by a small amount.

Interference Effects Based on Volume Considerations

In the previous section it has been shown that the overall lift-drag ratio of the isolated wing is not improved by the type of wing-body interference discussed herein. This conclusion does not eliminate the possibility that the volume contained in these bodies may be obtained at a relatively small drag penalty when compared with noninterference-type bodies. In this section the interference characteristics of the bodies are evaluated on a volume basis by means of an incremental drag coefficient $(\Delta C_D)_v$ which is based on the body volume raised to the two-thirds power. The drag increment is equal to the difference at a given lift between the drag of a wing-body configuration and the drag of the isolated wing and includes the skin-friction drag. The base-pressure drag is included in $(\Delta C_{D,t})_v$ and the discussion is based on these values. The corresponding drag values for zero base drag $(\Delta C_{D,f})_v$ are also presented as a matter of general interest.

The reference body chosen as a basis for comparing the volume efficiency of the various configurations was an isolated Haack body having a minimum drag for a given volume and length (ref. 6). For a skin-friction coefficient of 0.0013 the optimum fineness ratio of the reference body was 18.1. The calculated drag coefficient based on volume to the two-thirds power was 0.0195. This type of reference body was chosen because it approximates an optimum fuselage shape and its drag coefficient should be representative of the drag penalty incurred when volume is provided by use of a conventional fuselage.

The volume efficiencies for configurations 1 to 7 are presented in figure 27 where $(\Delta C_{D,t})_v$ is plotted as a function of the lift coefficient. None of the configurations has a volume drag coefficient which is as low as that of the isolated Haack body. Configuration 1, which had the highest maximum lift-drag ratio for configurations 1 to 7, has the lowest value of $(\Delta C_{D,t})_v$ of about 0.026, as compared with the value of 0.0195 for the isolated Haack body. For the remaining configurations the volume drag coefficient is from two to five times as large as the value for the Haack body. It is of interest to note that a large part of the drag penalty is caused by the base drag. This fact is shown at the bottom of figure 27 where the volume drag coefficient $(\Delta C_{D,f})_v$, which neglects the base-pressure force, has been plotted. Under these

CONFIDENTIAL


conditions the drags of all configurations except with body 7 are less than the drag of the isolated Haack body. It should be noted that since the fineness ratio of the reference body was fixed at 18.1, the length as well as the diameter of the reference body must necessarily vary as the volume of the experimental bodies varied. The reference bodies were always longer than the wing-root chord c_0 and varied from $1.25c_0$ for configuration 1 to $2.59c_0$ for configuration 7.

The effects of modifying the shape of body 4 are shown in figure 28. Maintaining a constant width over the rear 50 percent of the body (body 11) reduced the volume drag coefficient from that of configuration 4 by 30 to 40 percent. Smaller improvements were obtained by rounding the out-board edge of the body and by maintaining a constant width over the rear 25 percent of the body length. The volume drag of the basic body was increased by cutting off the bottom of the body along a Mach line. If the base drag does not have to be charged to the configurations, then the results of the volume efficiency comparison change and configuration 13 becomes the most desirable with an incremental volume drag of less than half that of the Haack body.

The results just presented indicate that the volume drag of the basic wedge-shaped bodies may be reduced by altering the basic shape. The magnitude of the changes would be expected to vary with the size of the basic body. It is not possible, however, to generalize these results and to determine which body shape (a basic wedge-shaped body at given values of δ and h/c_0 or a modified shape at other values of δ and h/c_0) would have the minimum volume drag for a required volume. Configurations 2, 6, and 11 had equal volumes and their volume drags may be compared in figure 29. When the base drag is taken into account the modified configuration 11 is better than either of the basic configurations 2 or 6. It might be possible, however, to improve the characteristics of configuration 2 by rounding its edges (similar to configuration 13) and perhaps have a lower volume drag than that of configuration 11. Additional experimental results would be required to determine this point.

CONCLUSIONS

An investigation has been made of the interference effects which are produced at a Mach number of 3.11 by wedge-shaped bodies, simulating nacelles, located under a triangular wing. The effects of the basic variables of wedge angle and height, of air flow, and of modifications to the basic shapes were studied by measuring and integrating the pressures on the bodies and on the bottom wing surface. The results were analyzed both from nacelle considerations where the base-pressure effects may be neglected and from volume considerations where the base-pressure effects



DECLASSIFIED

17

must be included in the drag. The data and discussion do not include the forces generated by the top surface of the wing since the body pressures are generally felt only on the lower wing surface. The tests were made in the Langley gas dynamics laboratory in a blowdown jet at angles of attack from 0° to 6° . The following conclusions were reached:

1. The use of the basic body shapes under the triangular wing did not result in a maximum lift-drag ratio which was larger than that of the isolated wing, even when the base-pressure drag was neglected. The maximum lift-drag ratio of the configuration with the smallest body was about equal to that of the wing alone, but the use of larger bodies resulted in lower values. Use of bodies smaller than those tested might produce maximum lift-drag ratios larger than that of the wing alone, but the increment probably would be small.

2. The agreement between the linear theory and the experimental results was fairly good at low lift coefficients for the smaller basic bodies. The discrepancies increased as the body size increased. At high lift coefficients the linear theory predicted more drag than was measured but underestimated the forces at a given angle of attack.

3. Modification of the basic body shape by rounding the outboard edge of the body or by maintaining a constant width over the rear portion of the body reduced the body drag and improved the maximum lift-drag ratio of the basic wedge-shaped body.

4. Modification of the basic body shape to incorporate a supersonic nose inlet did not alter the interference characteristics of the basic shape.

5. When the bodies were considered from the viewpoint of drag per unit volume, and the base-drag effects were included, it was shown that none of the bodies were as efficient as an isolated Haack body of fineness ratio 18.1 which was used as a reference.

Langley Research Center,
National Aeronautics and Space Administration,
Langley Field, Va., July 7, 1959.



031712201030
CONFIDENTIAL

APPENDIX A

The linear-theory equations from which the calculated results were obtained are presented herein. These equations were obtained from the Langley Theoretical Mechanics Division.

The lift coefficient induced on the lower wing surface by the bodies is independent of angle of attack and is expressed by the equation

$$C_{L,B} = \frac{2\delta}{\beta\eta} \left[\beta \frac{h}{c_o} \left(2 - \frac{\beta h}{c_o} \right) \right]$$

The total lift coefficient on the body and lower wing surface at angles of attack is expressed by the equation

$$C_{L,p} = C_{L,B} + \frac{2\alpha}{\beta}$$

The drag coefficient $C_{D,B}$ of the body is induced by the pressure field of the body itself and is expressed by the equation

$$C_{D,B} = \frac{4\delta^2}{\pi\beta\eta} \left\{ \frac{2\beta h}{c_o} \sin^{-1} \left(\frac{2\beta h}{c_o} \right) + 2 \left(\frac{\beta h}{c_o} \right)^2 \log \left[\frac{c_o}{2\beta h} + \sqrt{\left(\frac{c_o}{2\beta h} \right)^2 - 1} \right] + \frac{1}{2} \sqrt{1 - \left(\frac{2\beta h}{c_o} \right)^2} - \frac{1}{2} \right\}$$

The drag coefficient of the wedge $C_{D,B,w}$ is caused by the pressure field of the wing and is expressed by the equation

$$C_{D,B,w} = \frac{2\alpha\delta}{\pi\beta\sqrt{\eta^2 - 1}} \left\{ \frac{4\beta h}{c_o} \cos^{-1} \frac{1}{\sqrt{\eta^2 - (\eta^2 - 1)\left(\frac{\beta h}{c_o}\right)^2}} - \pi \left(\frac{\beta h}{c_o}\right)^2 \frac{\sqrt{\eta^2 - 1}}{\eta} \right. \\ \left. + \left[\frac{2\left(\frac{\beta h}{c_o}\right)^2 (\eta^2 - 1) + 2\eta^2}{\eta\sqrt{\eta^2 - 1}} \right] \left[\tan^{-1} \frac{\frac{\beta h}{c_o}}{\eta\sqrt{1 - \left(\frac{\beta h}{c_o}\right)^2}} \right] - \frac{2}{\sqrt{\eta^2 - 1}} \sin^{-1} \frac{\beta h}{c_o} \right\}$$

The total-pressure drag, with base drag neglected, is expressed by the equation

$$C_{D,p} = C_{D,B} + C_{D,B,w} + (C_{L,p})\alpha$$

031710201030

CONFIDENTIAL

REFERENCES

1. Ferri, Antonio, Clarke, Joseph H., and Casaccio, Anthony: Drag Reduction in Lifting Systems by Advantageous Use of Interference. PIBAL Rep. No. 272 (Contract No. AF 18(600)-694), Polytechnic Inst., Brooklyn, May 1955.
2. Rossow, Vernon J.: A Theoretical Study of the Lifting Efficiency at Supersonic Speeds of Wings Utilizing Indirect Lift Induced by Vertical Surfaces. NACA RM A55L08, 1956.
3. Eggers, A. J., Jr., and Syvertson, Clarence A.: Aircraft Configurations Developing High Lift-Drag Ratios at High Supersonic Speeds. NACA RM A55L05, 1956.
4. Carmel, Melvin M., Kelly, Thomas C., and Gregory, Donald T.: Aerodynamic Characteristics at Mach Numbers From 2.5 to 3.5 of a Canard Bomber Configuration Designed for Supersonic Cruise Flight. NACA RM L58G16, 1958.
5. Church, James D., Hayes, William C., Jr., and Sleeman, William C., Jr.: Investigation of Aerodynamic Characteristics of an Airplane Configuration Having Tail Surfaces Outboard of the Wing Tips at Mach Numbers of 2.30, 2.97, and 3.51. NACA RM L58C25, 1958.
6. Haack, W.: Projectile Shapes for Smallest Wave Drag. AII No. 27736, Translation No. A9-T-3, Contract W33-038-ac-15004(16351), Air Materiel Command, U. S. Air Force, Brown Univ., 1948.

CONFIDENTIAL

DECLASSIFIED
CONFIDENTIAL

21

TABLE I.- PRESSURE FORCES MEASURED ON WING ALONE AND ON WING-BODY CONFIGURATIONS

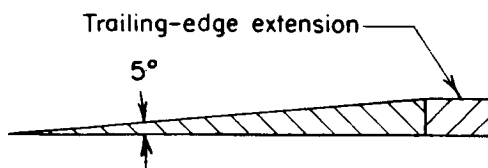
Configuration	α , deg	$C_{L,p}$	$C_{D,p}$	$C_{D,b}$
Wing alone	0	0	0	
	2	.0268	.000935	
	4	.0546	.00382	
	6	.0859	.00902	
Body 1	0	0.00772	0.000169	0.00095
	2	.0386	.00164	.00090
	4	.0636	.00495	.00083
	6	.0974	.0109	.00072
Body 2	0	0.0186	0.000866	0.00313
	2	.0507	.00302	.00304
	4	.0773	.00705	.00292
	6	.1100	.0137	.00287
Body 3	0	0.0144	0.00064	0.00221
	2	.0411	.00233	.00217
	4	.0721	.00636	.00209
	6	.1044	.0128	.00199
Body 4	0	0.0244	0.00175	0.00466
	2	.0523	.00426	.00470
	4	.0830	.00890	.00455
	6	.1141	.0159	.00447
Body 5	0	0.0360	0.00343	0.00671
	2	.0653	.00637	.00671
	4	.0962	.0119	.00648
	6	.1296	.0198	.00648
Body 6	0	0.0230	0.00158	0.00347
	2	.0509	.00385	.00335
	4	.0790	.00815	.00321
	6	.1110	.0150	.00310
Body 7	0	0.0532	0.00798	0.0102
	2	.0850	.0124	.00989
	4	.117	.0192	.0102
	6	.145	.0280	.0105
Body 8	0	0.0121	0.000564	
	2	.0407	.00238	
	4	.0705	.00622	
	6	.105	.0129	
Body 9	0	0.0243	0.00168	
	2	.0522	.00418	
	4	.0825	.00895	
	6	.113	.0160	
Body 10	0	0.0153	0.00519*	
	2	.0421	.00706*	
	4	.0725	.0111*	
	6	.104	.0171*	
Body 11	0	0.0162	0.00117	0.00212
	2	.0415	.00289	.00202
	4	.0713	.00672	.00197
	6	.104	.0130	.00181
Body 12	0	0.0214	0.00158	0.00355
	2	.0489	.00377	.00344
	4	.0782	.00801	.00335
	6	.110	.0146	.00324
Body 13	0	0.0299	0.00147	0.00439
	2	.0549	.00391	.00436
	4	.0850	.00856	.00433
	6	.120	.0159	.00419
Body 14	0	0.0277	0.00155	0.00400
	2	.0560	.00413	.00400
	4	.0871	.00902	.00394
	6	.120	.0164	.00394

* Includes pressures on rear surface of body.



L-254

CONFIDENTIAL



TYPICAL WING SECTION-AA

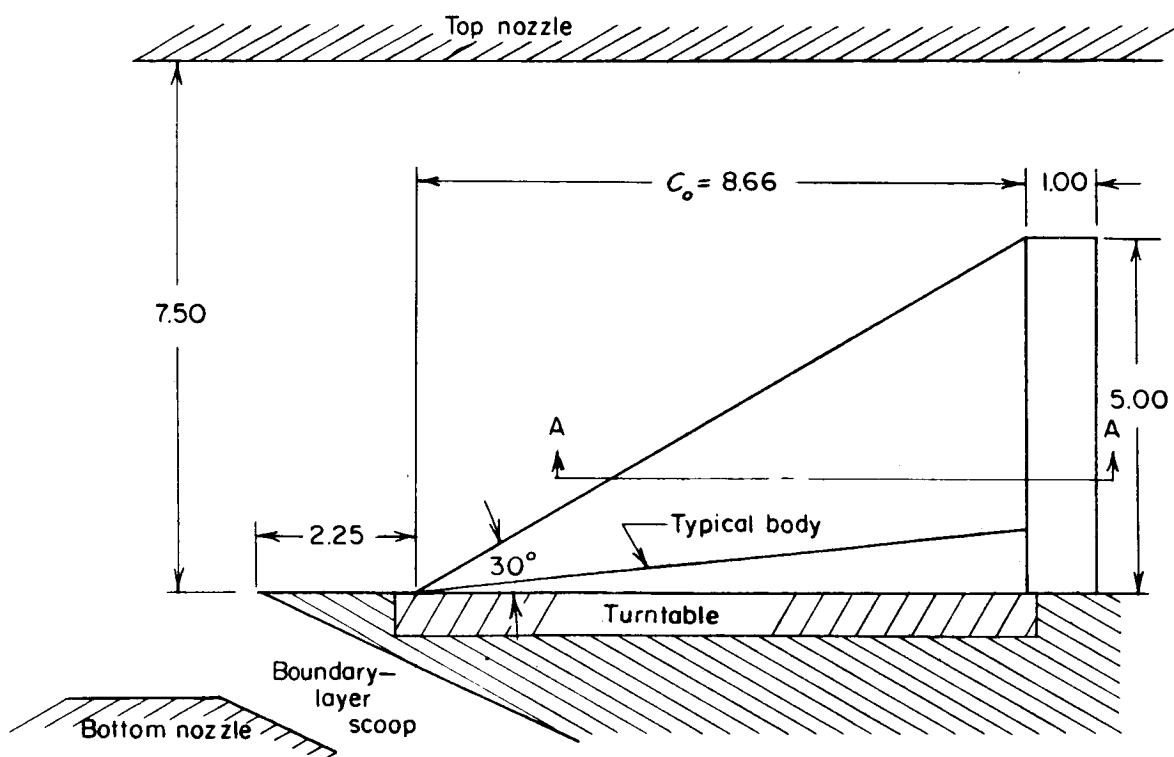
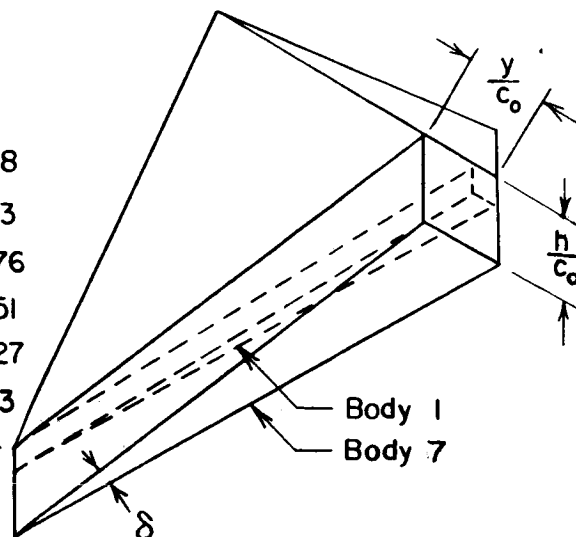


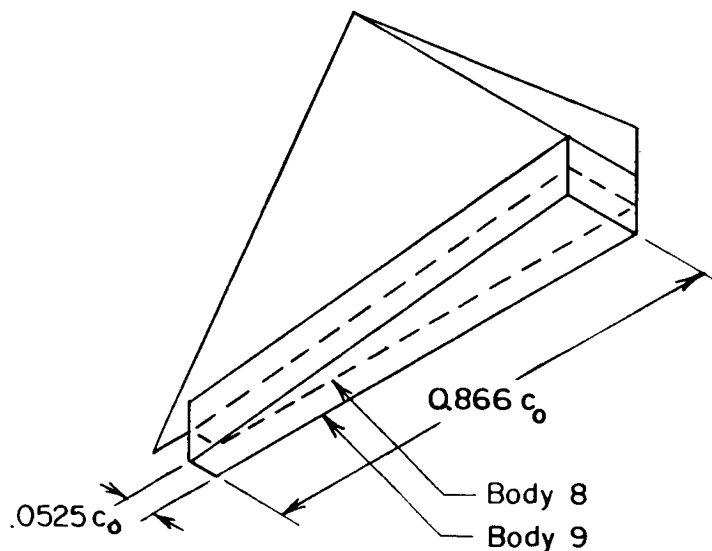
Figure 1.- Schematic drawing of experimental setup. All linear dimensions are in inches.

I-254

Body	δ, deg	$\frac{h}{c_0}$	$\frac{y}{c_0}$	$\frac{\text{Vol.}}{c_0^3}$
1	3	0.0525	0.0525	0.00138
2	3	.158	.0525	.00413
3	6	.0525	.105	.00276
4	6	.105	.105	.00551
5	6	.158	.105	.00827
6	9	.0525	.158	.00413
7	9	.158	.158	.0124



Body	δ, deg	$\frac{h}{c_0}$	$\frac{y}{c_0}$
8	6	0.0525	0.144
9	6	.105	.144

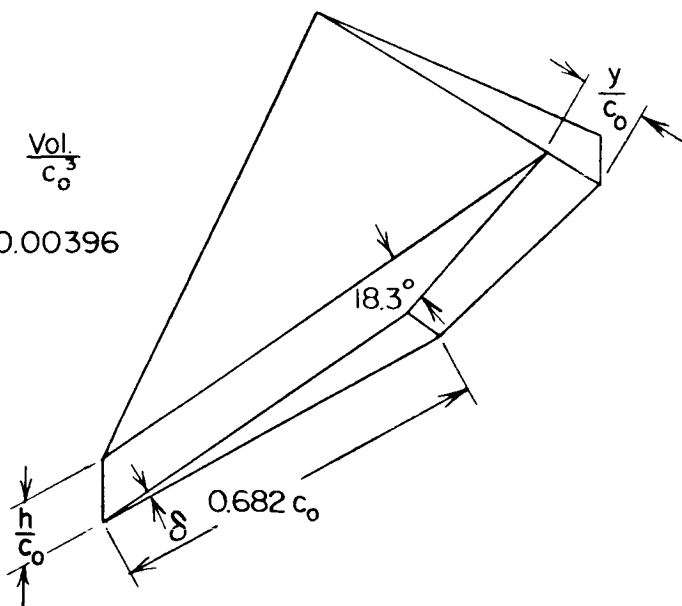


(a) Bodies 1 to 9.

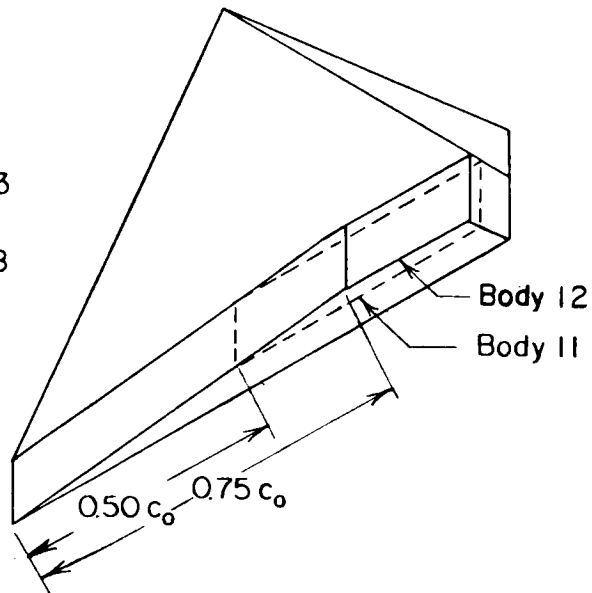
Figure 2.- Schematic drawing of body shapes investigated. Wing extension deleted for clarity. Wing root chord c_0 is 8.66 inches.

CONFIDENTIAL

Body	δ, deg	$\frac{h}{c_0}$	$\frac{y}{c_0}$	$\frac{\text{Vol.}}{c_0^3}$
10	6	0.105	0.105	0.00396



Body	δ, deg	$\frac{h}{c_0}$	$\frac{y}{c_0}$	$\frac{\text{Vol.}}{c_0^3}$
11	6	0.105	0.0525	0.00413
12	6	0.105	0.0788	0.00518



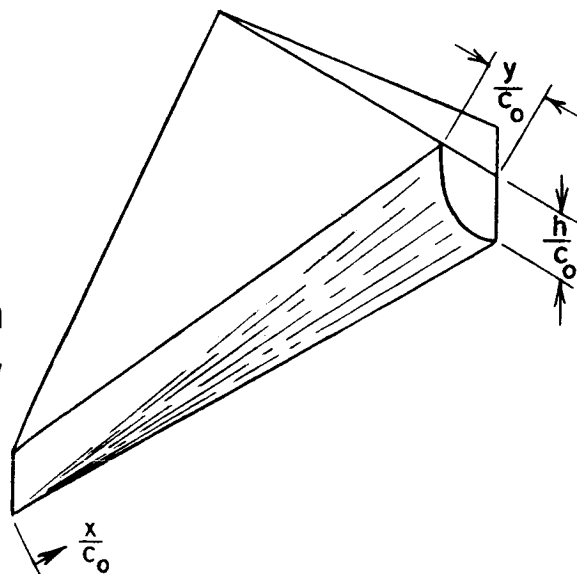
(b) Bodies 10 to 12.

Figure 2.- Continued.

CONFIDENTIAL

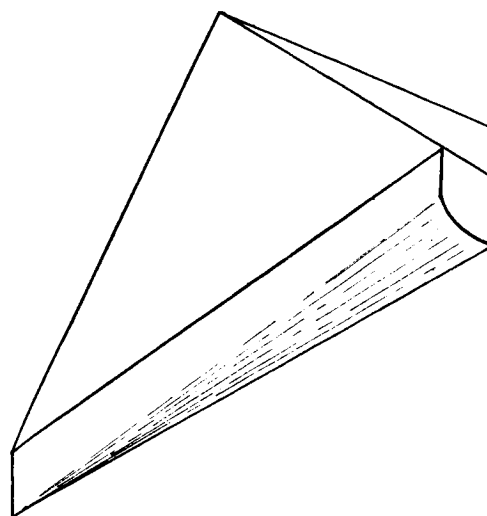
Body	δ, deg	$\frac{h}{c_0}$	$\frac{y}{c_0}$	$\frac{\text{Vol}}{c_0^3}$
13	6	0.120	0.105	0.00551

Shaded portion of body has a conical shape. Local radius is equal to local body width.



Body	δ, deg	$\frac{h}{c_0}$	$\frac{y}{c_0}$	$\frac{\text{Vol}}{c_0^3}$
14	6	0.112	0.105	0.00551

Shaded portion of body has a 2 to 1 elliptical shape. Local major axis is equal to local body width.



(c) Bodies 13 and 14.

Figure 2.- Concluded.

CONFIDENTIAL

CONFIDENTIAL

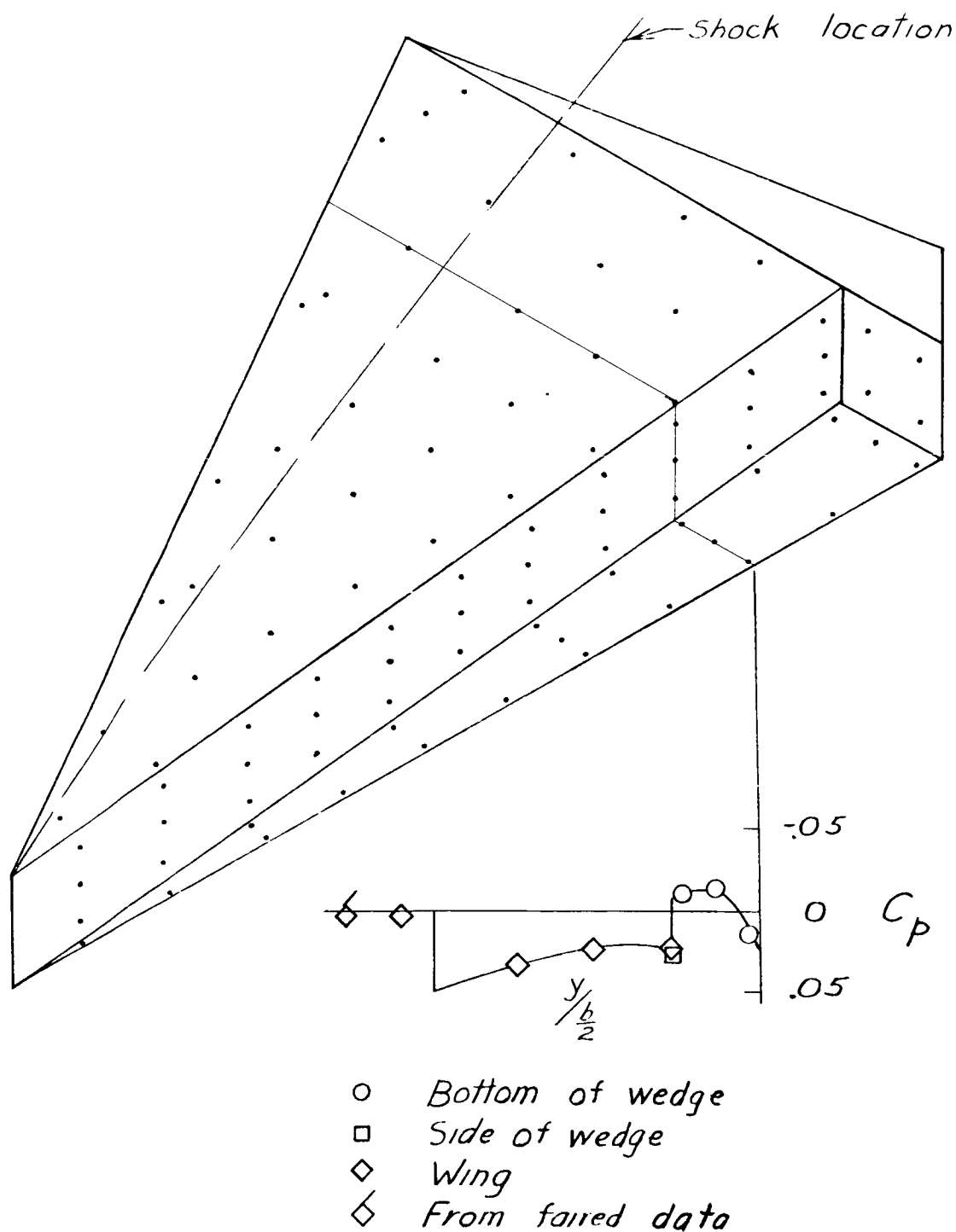


Figure 3.- Schematic drawing of wing-body configuration 4, showing location of orifices, typical pressure distribution at $\alpha = 0^\circ$, and location of body shock at $\alpha = 0^\circ$.

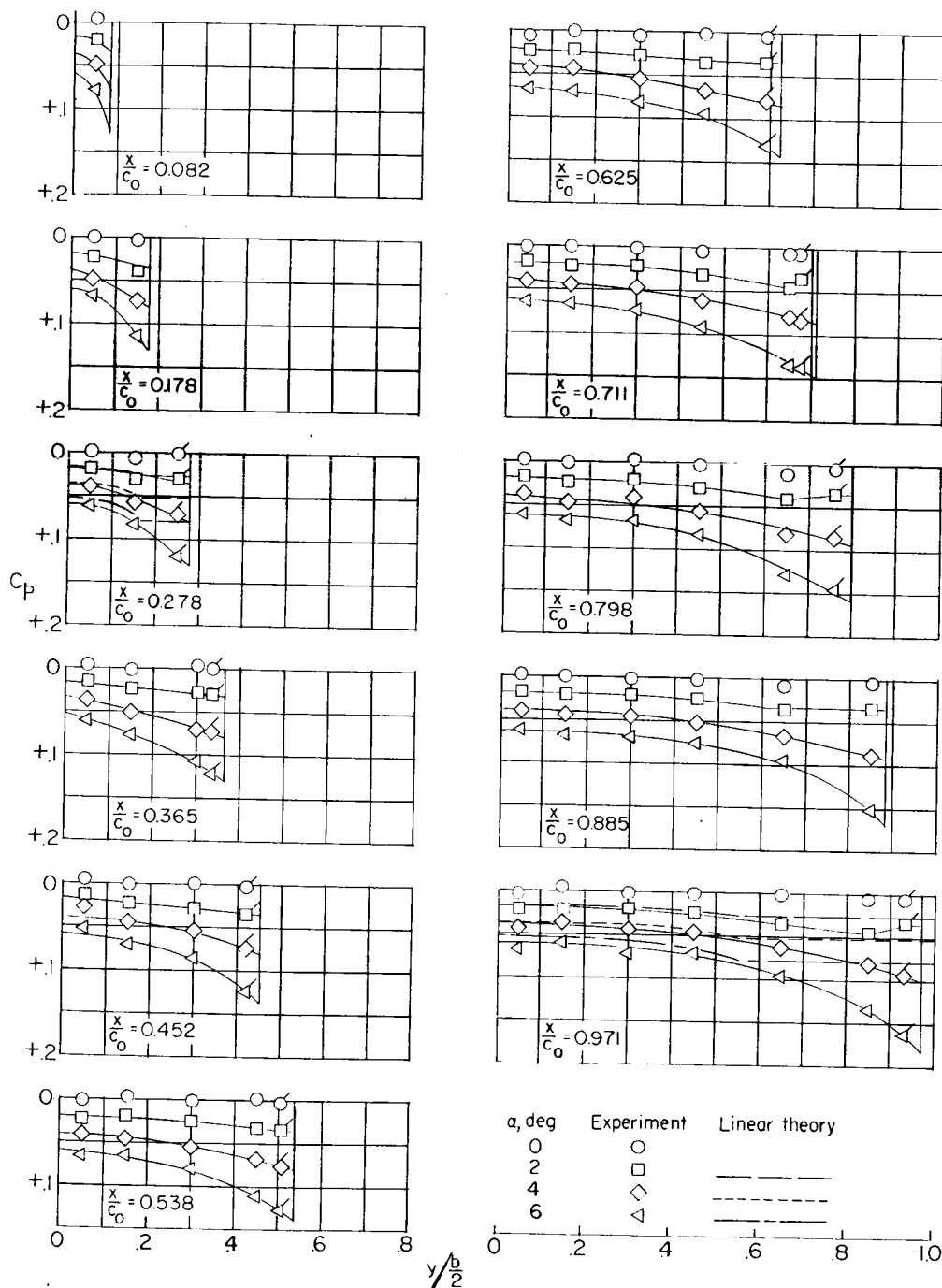
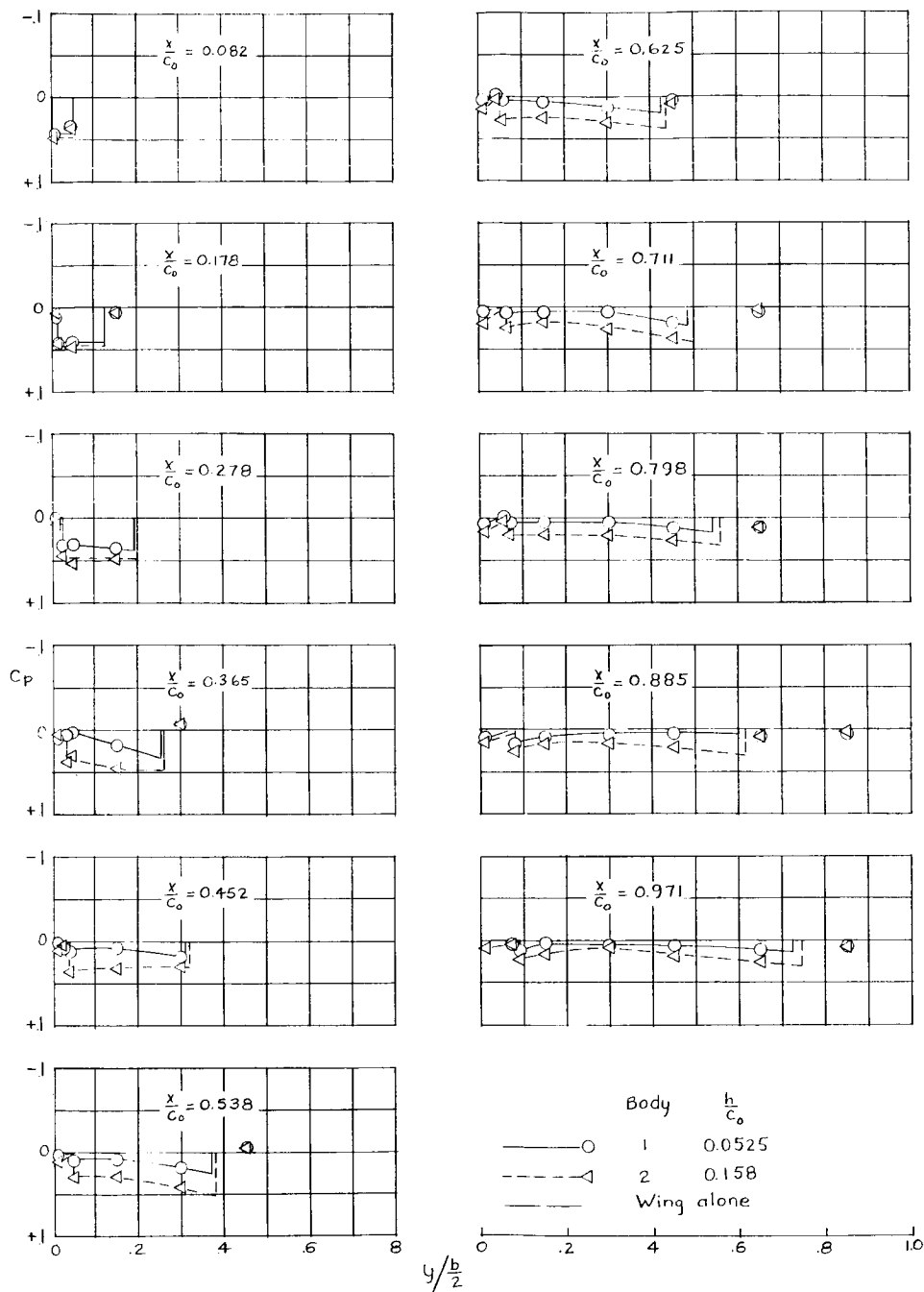


Figure 4.- Pressure distributions on bottom surface of wing alone and comparison with linear-theory predictions. Flagged symbols are from faired data.

CONFIDENTIAL

(a) $\alpha = 0^\circ$.Figure 5.- Pressure distributions on lifting surfaces of wing-body configurations for bodies 1 and 2. $\delta = 3^\circ$.

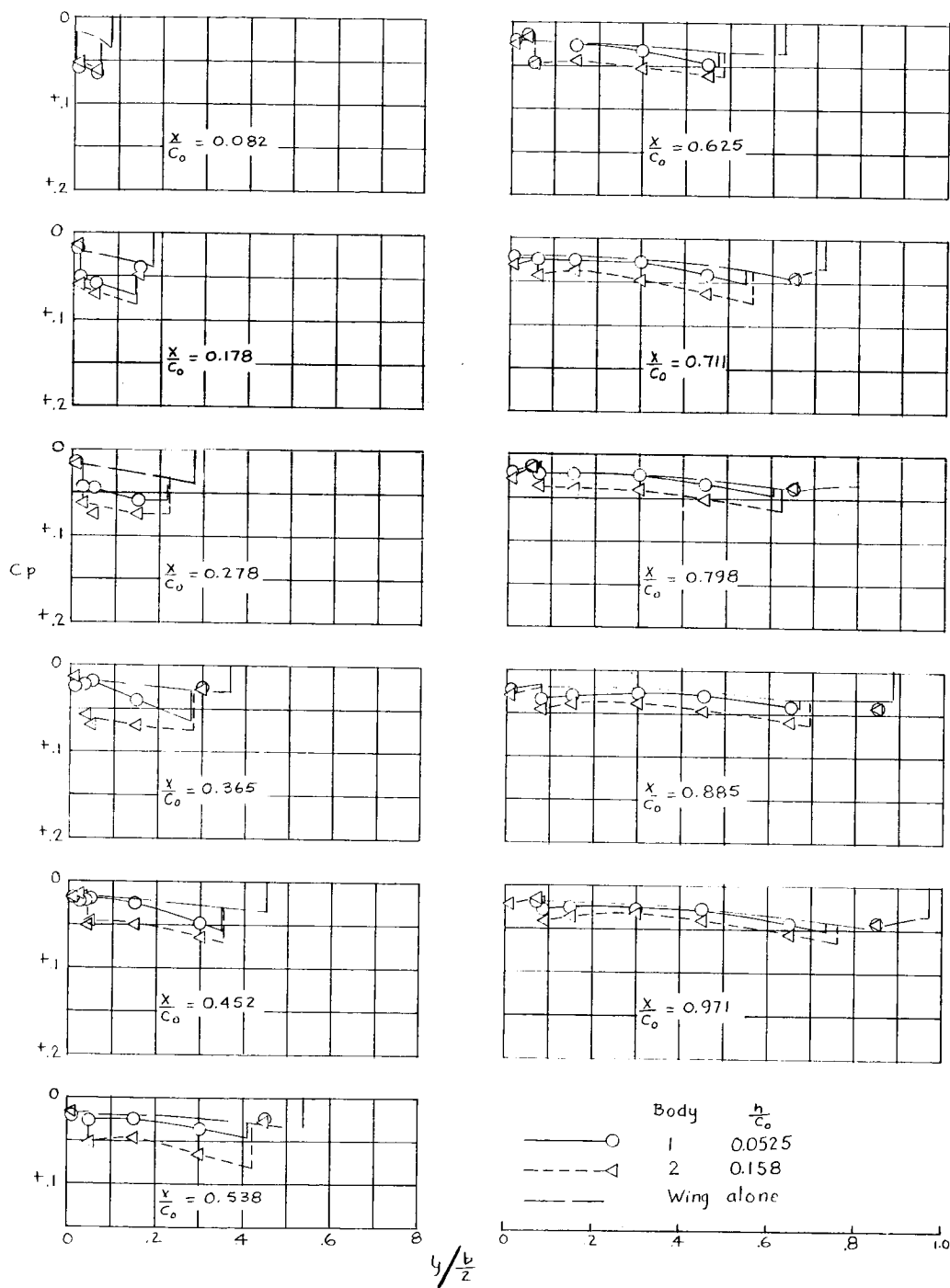


Figure 5.- Continued.

CONFIDENTIAL

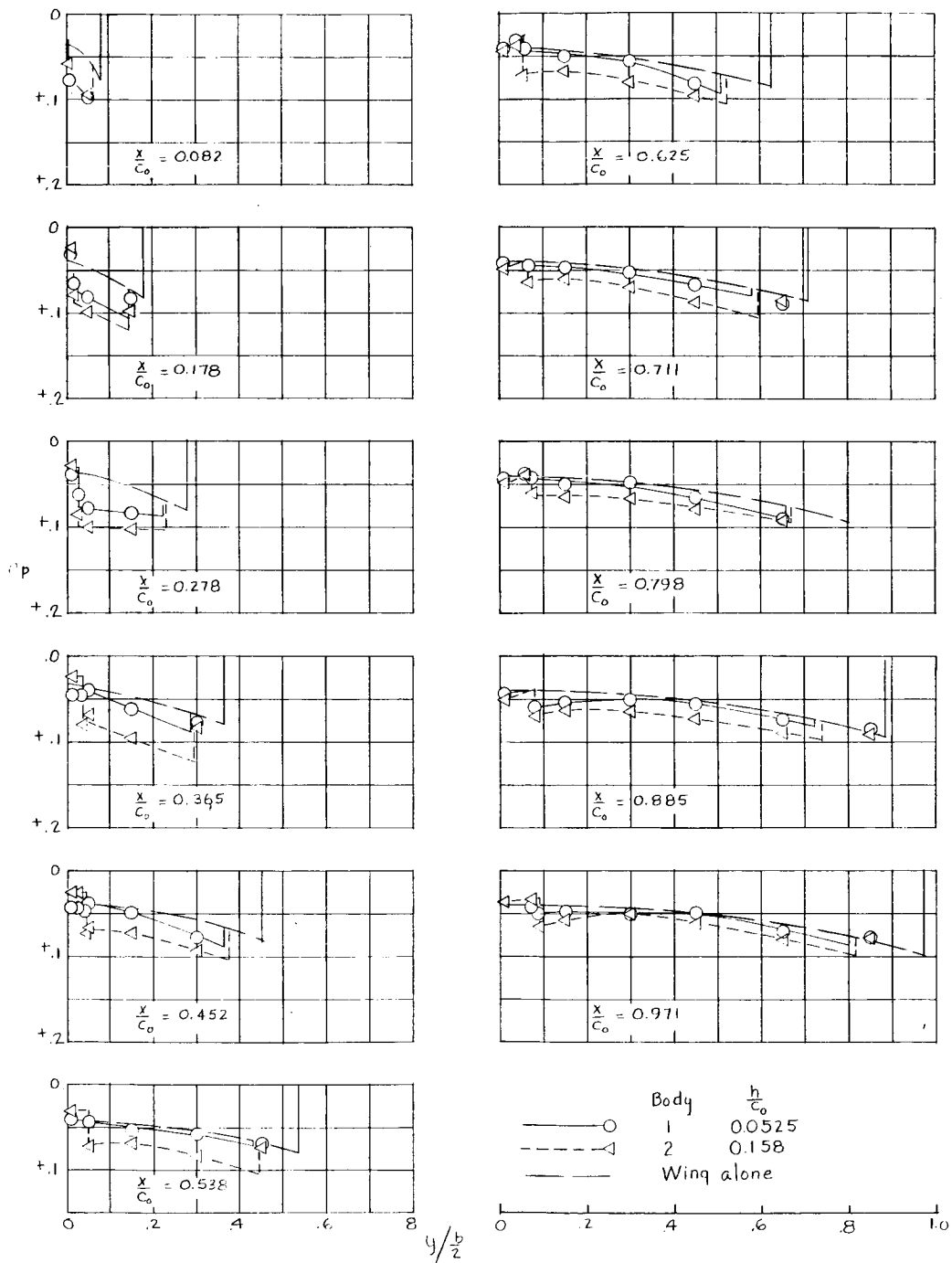
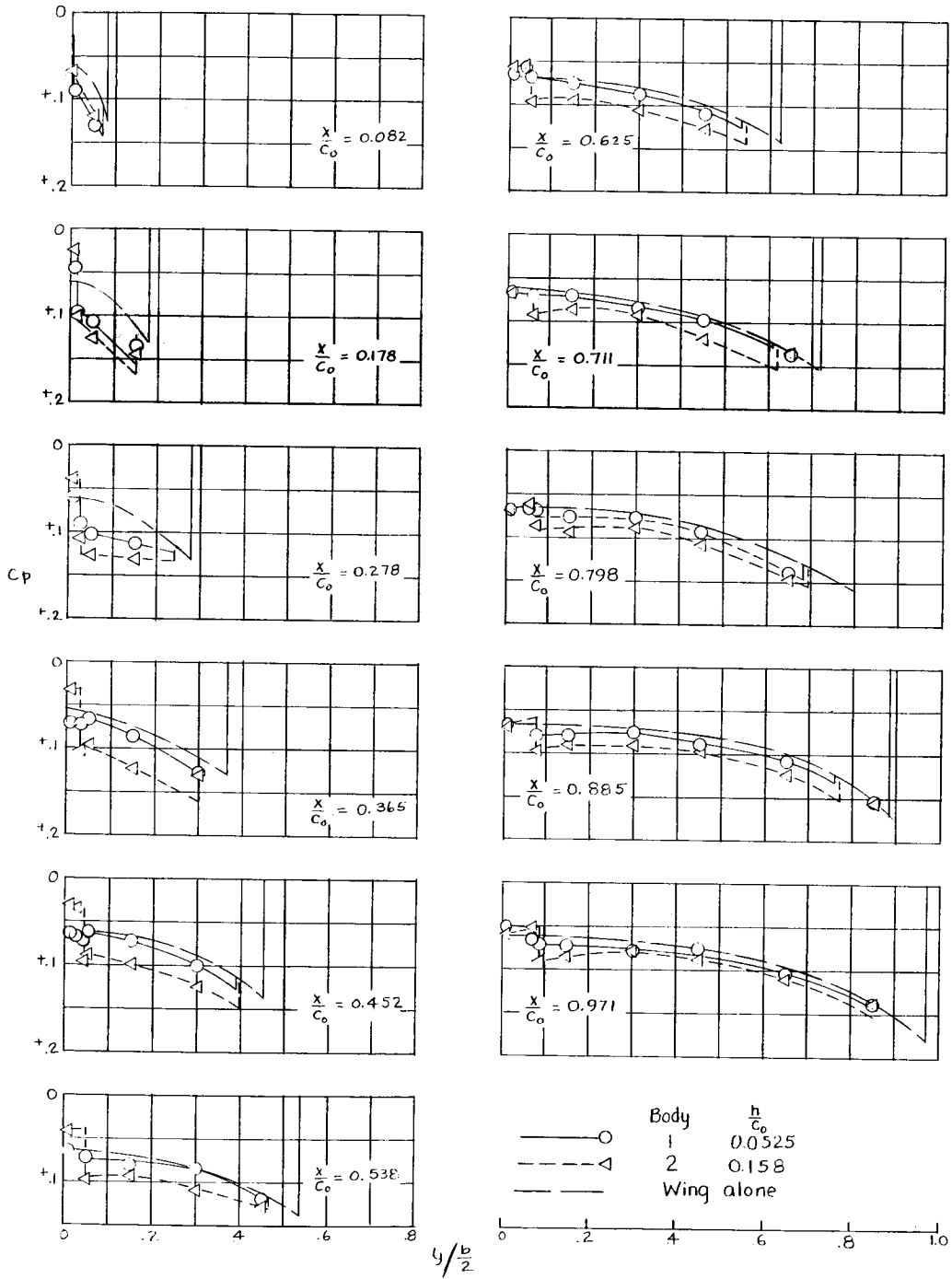
(c) $\alpha = 4^\circ$.

Figure 5.- Continued.



(d) $\alpha = 6^\circ$.

Figure 5.- Concluded.

CONFIDENTIAL

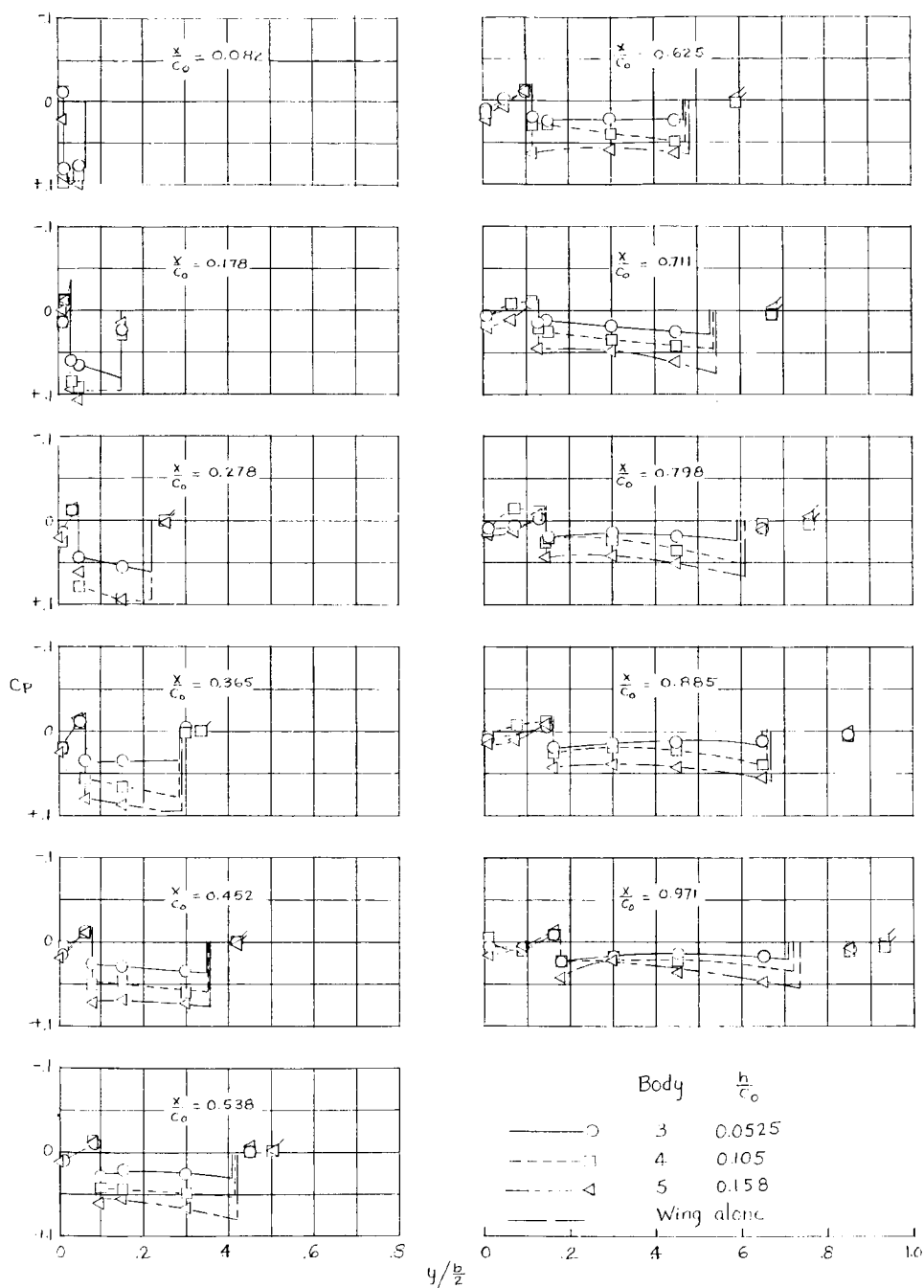
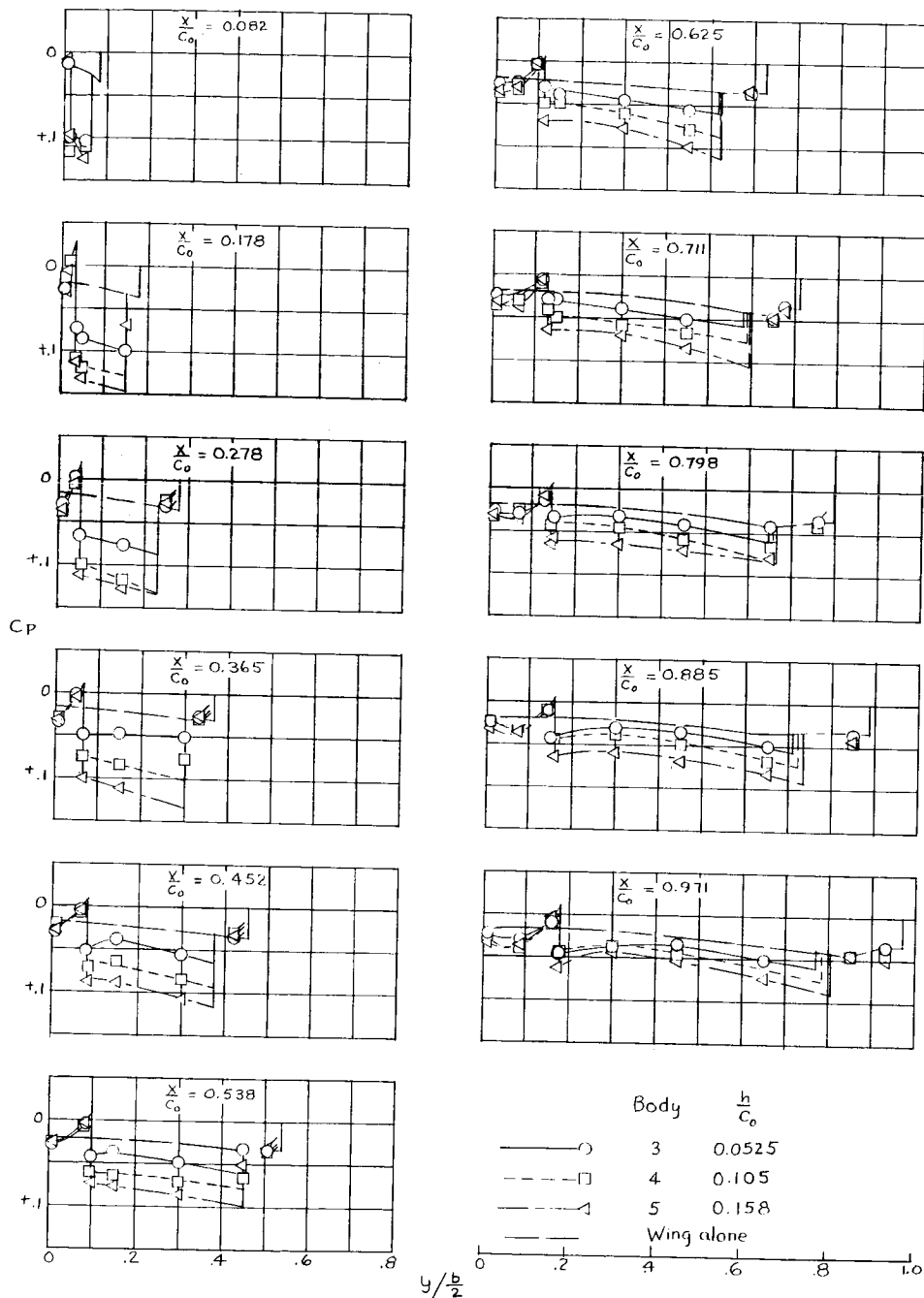
(a) $\alpha = 0^\circ$.

Figure 6.- Pressure distributions on lifting surfaces of wing-body configurations for bodies 3, 4, and 5. $\delta = 6^\circ$. Flagged symbols are from faired data.

CONFIDENTIAL

L-254



(b) $\alpha = 2^\circ$.

Figure 6.- Continued.

CONFIDENTIAL

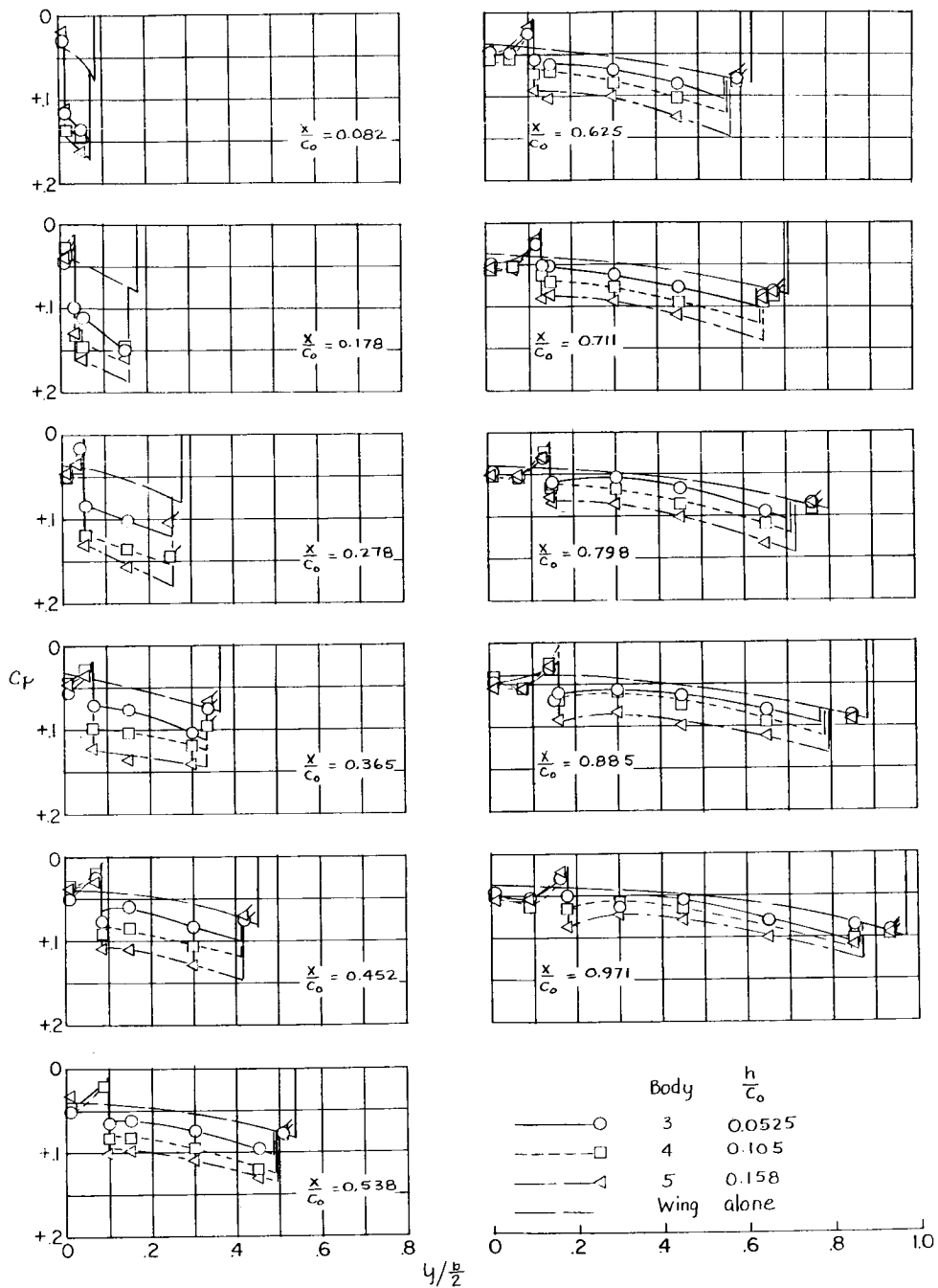
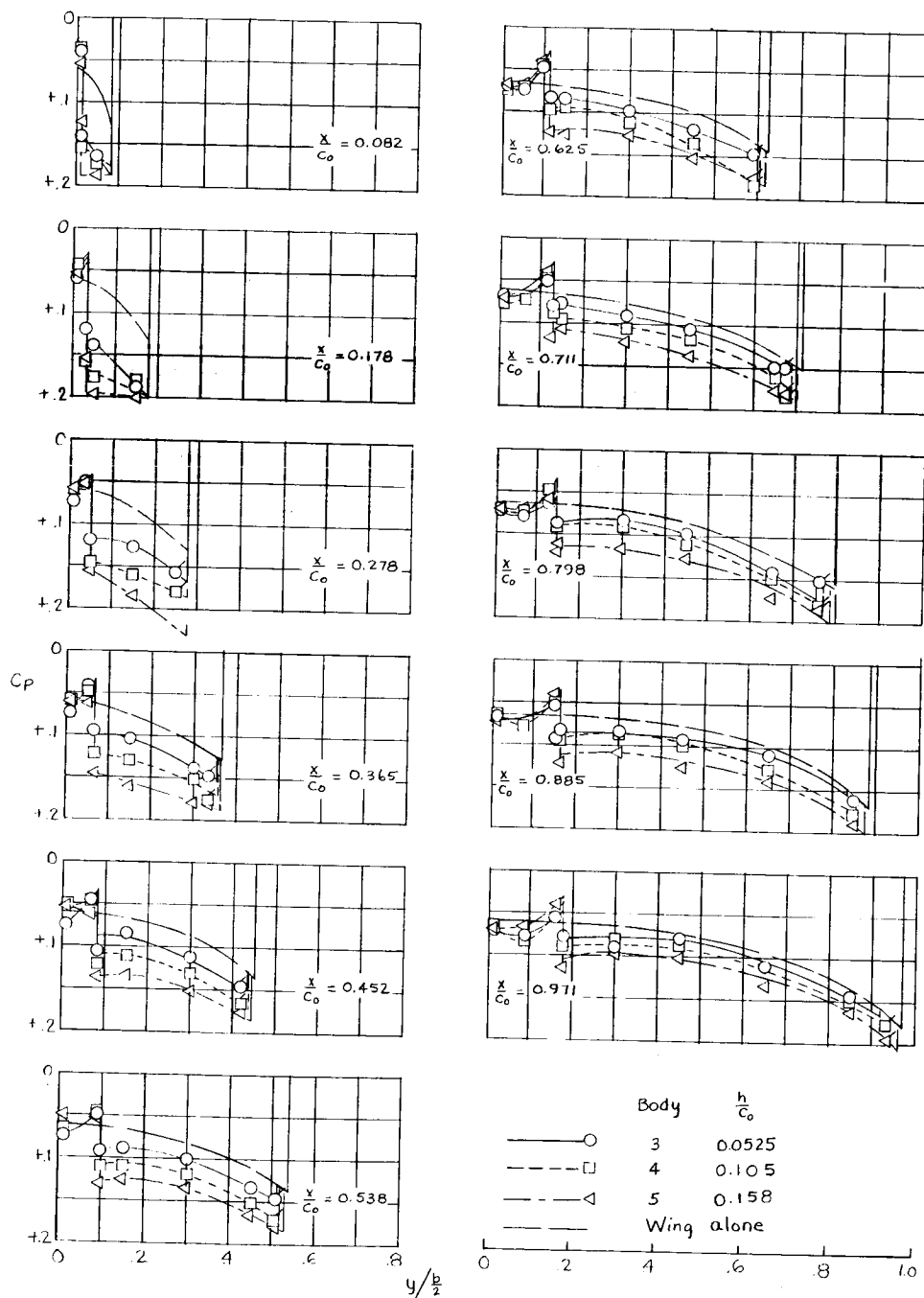
(c) $\alpha = 4^\circ$.

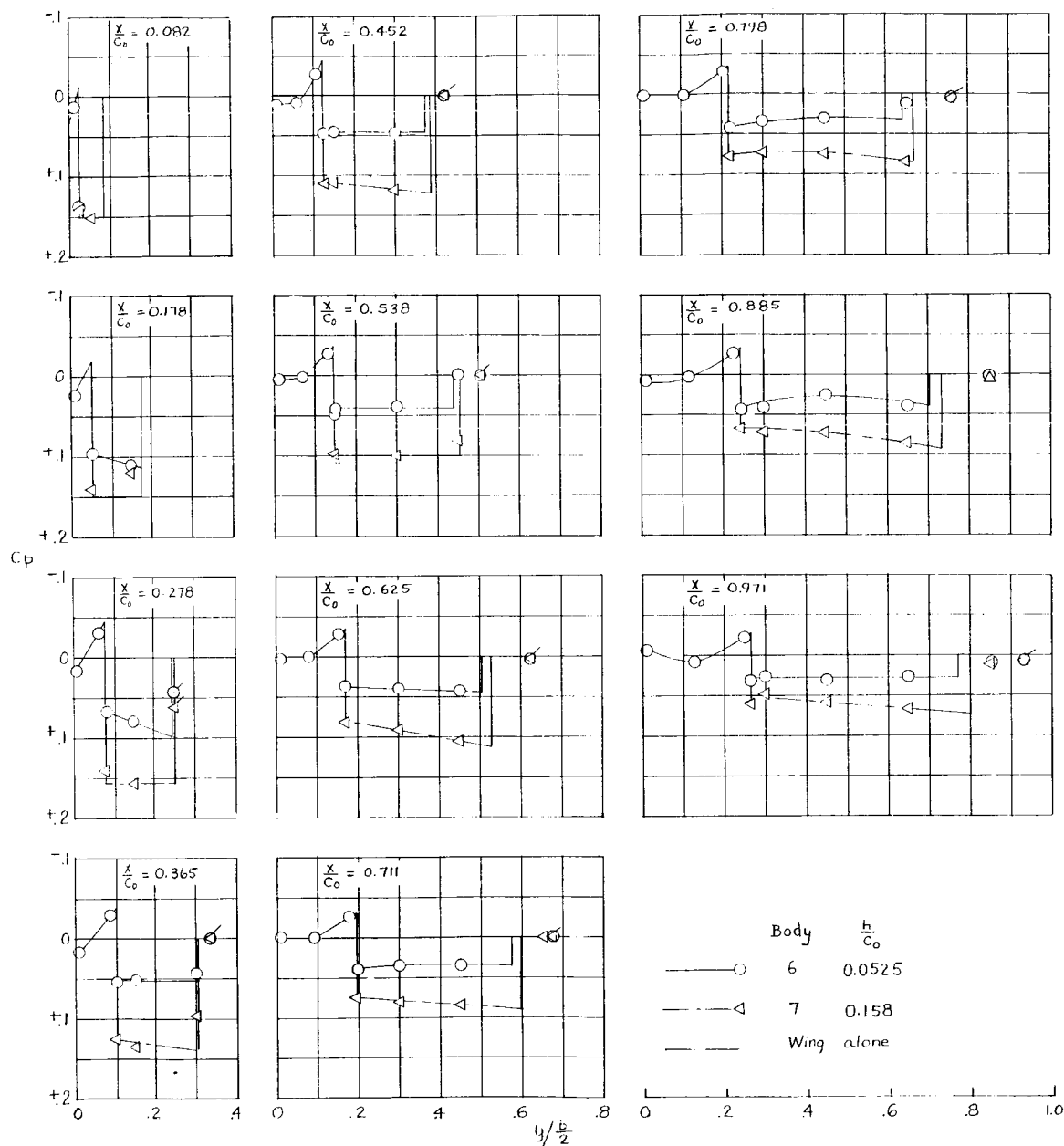
Figure 6.- Continued.



(d) $\alpha = 6^\circ$.

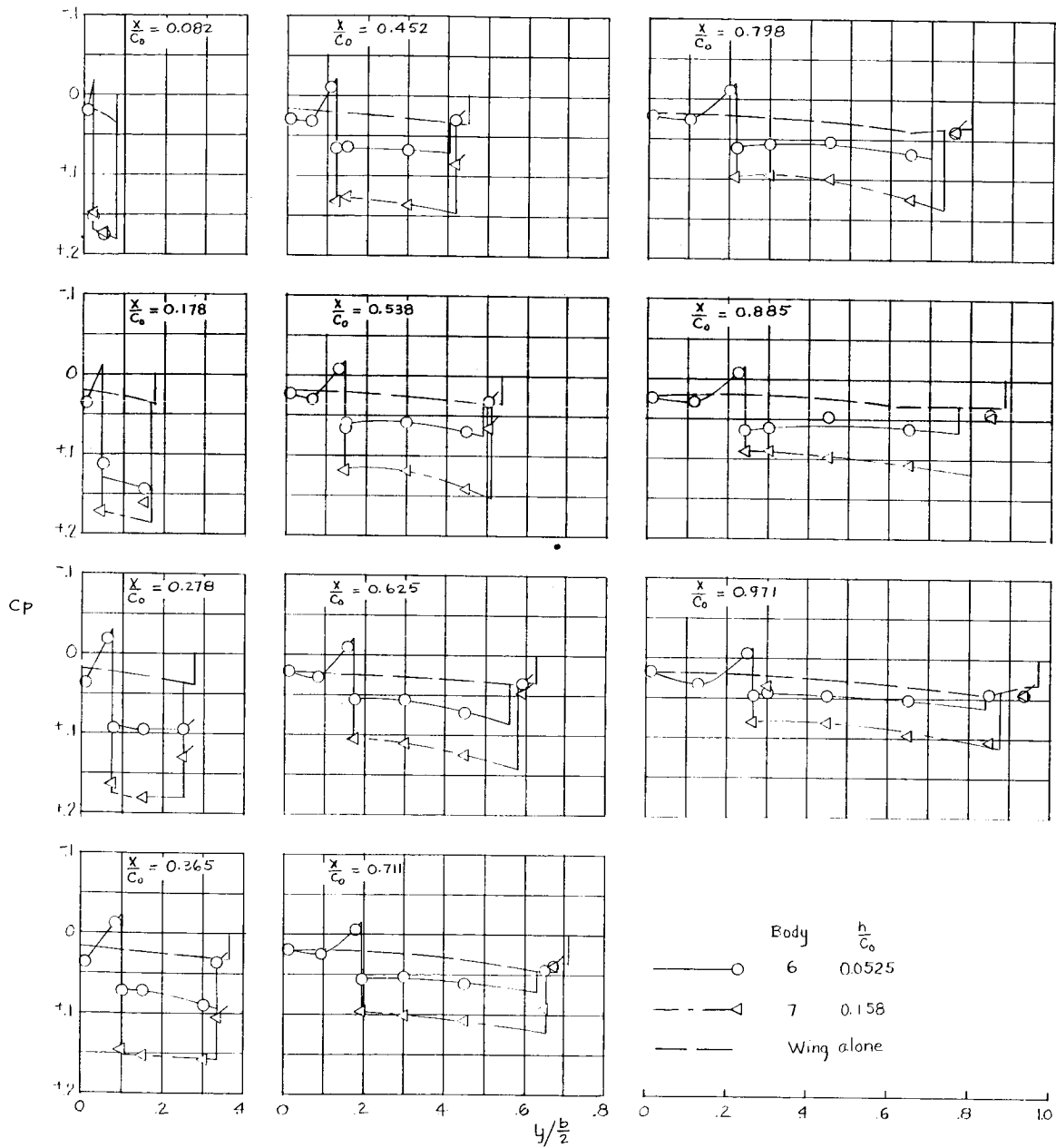
Figure 6.- Concluded.

CONFIDENTIAL



(a) $\alpha = 0^\circ$.

Figure 7.- Pressure distributions on lifting surfaces of wing-body configurations for bodies 6 and 7. $\delta = 9^\circ$. Flagged symbols are from faired data.



(b) $\alpha = 2^\circ$.

Figure 7.- Continued.

CONFIDENTIAL

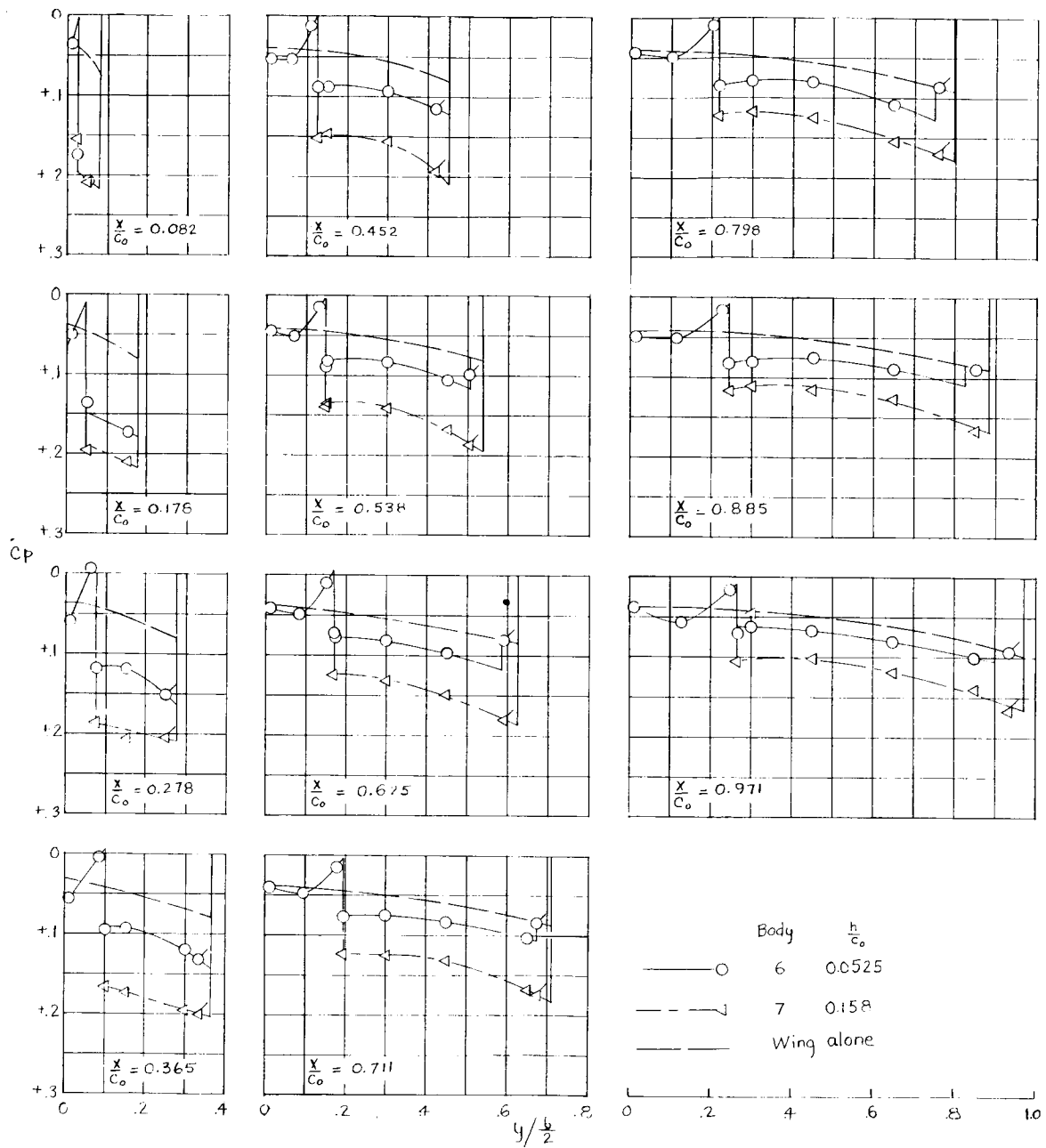
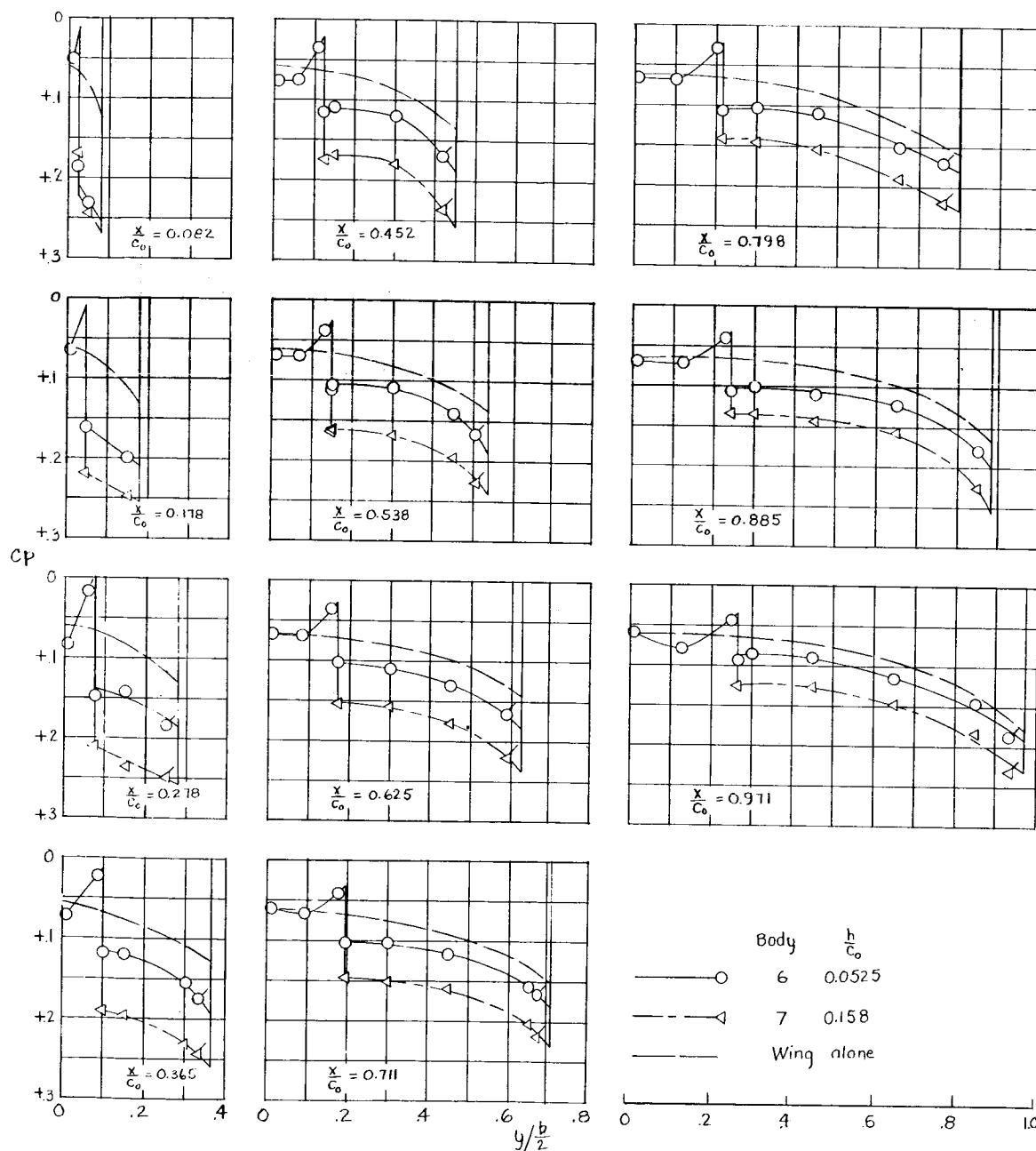
(c) $\alpha = 4^\circ$.

Figure 7.- Continued.

CONFIDENTIAL



(d) $\alpha = 6^\circ$.

Figure 7.- Concluded.

CONFIDENTIAL

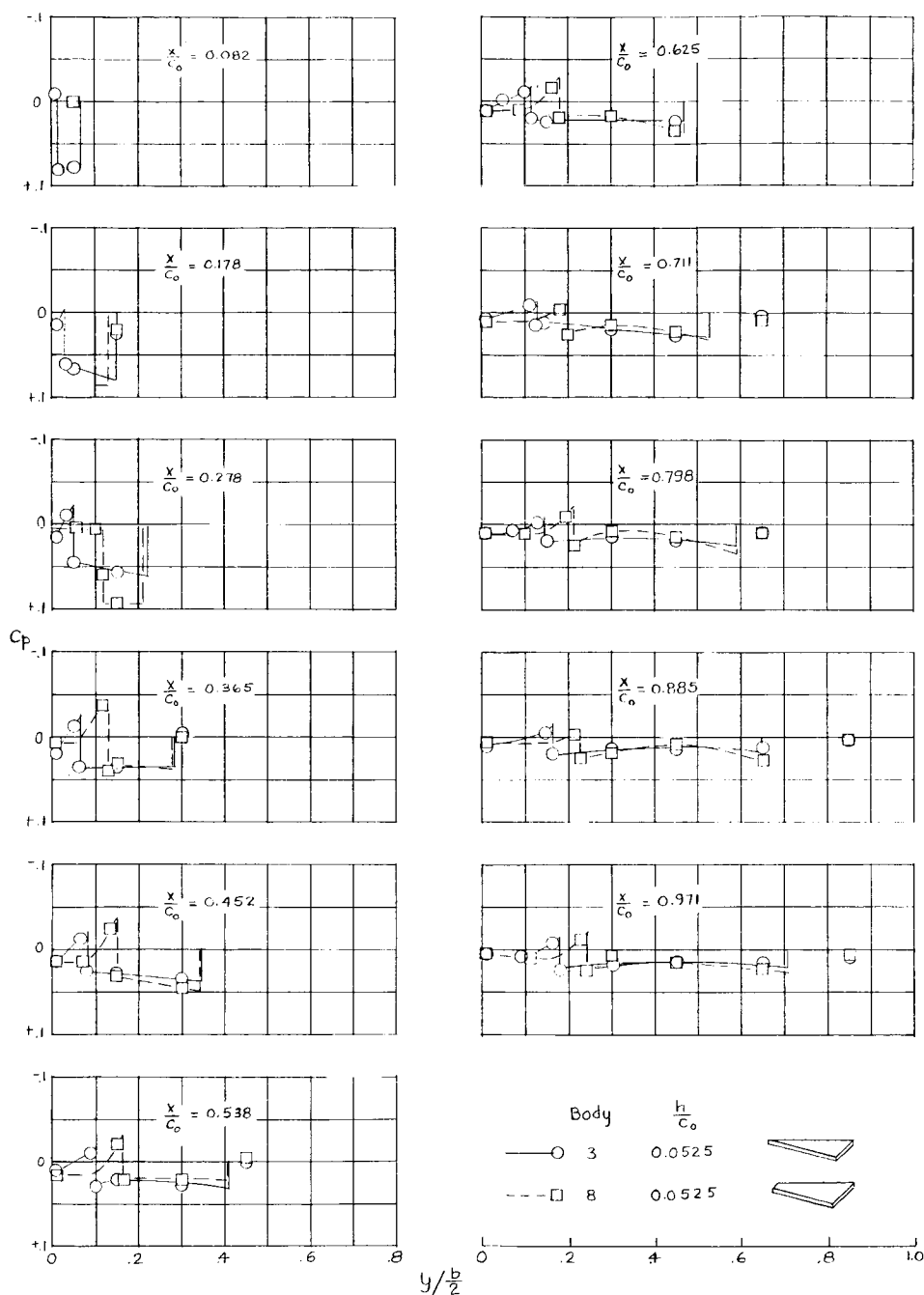


Figure 8.- Pressure distributions on lifting surfaces of wing-body configurations for bodies 3 and 8. Flagged symbols are from faired data.

CONFIDENTIAL

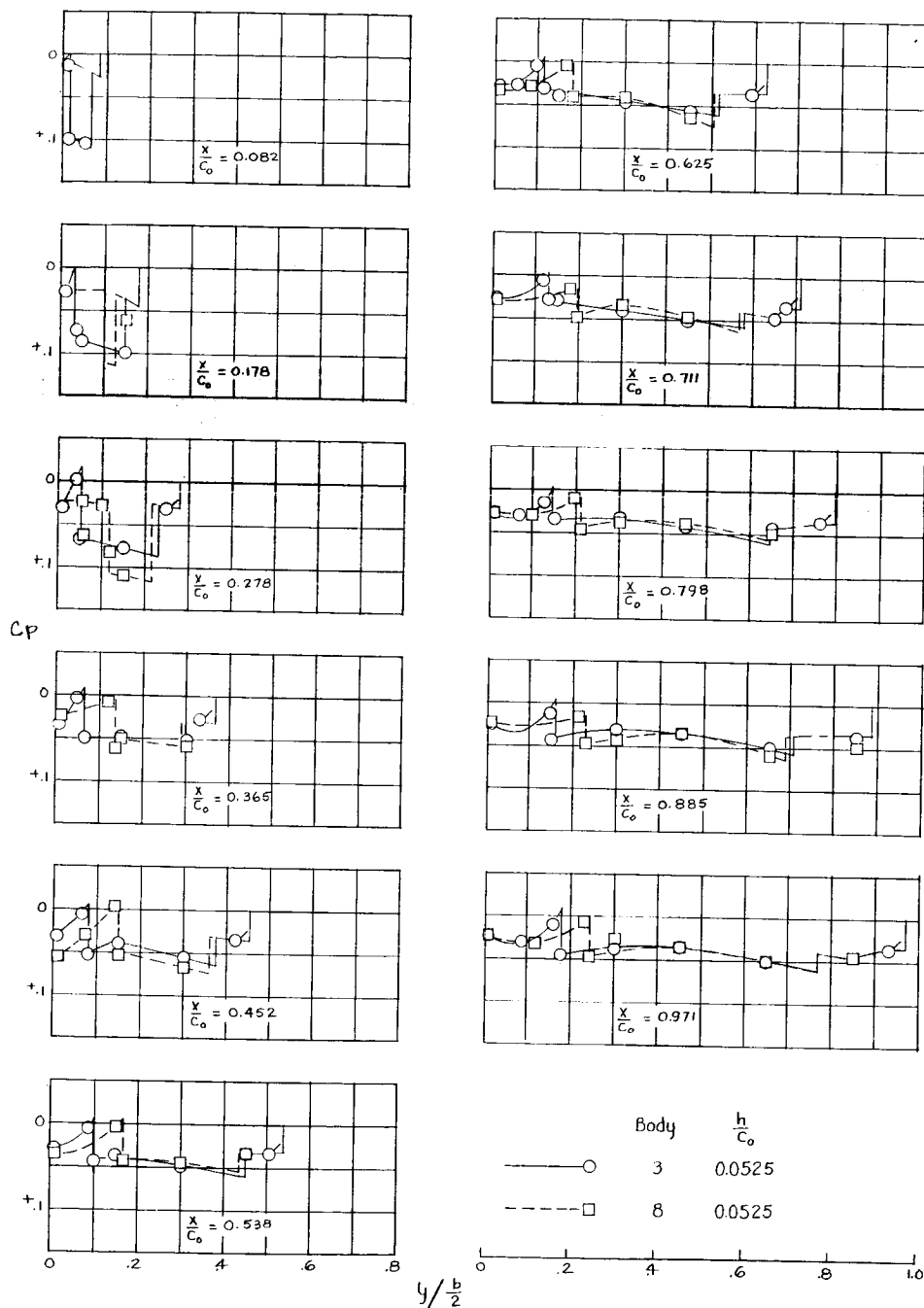
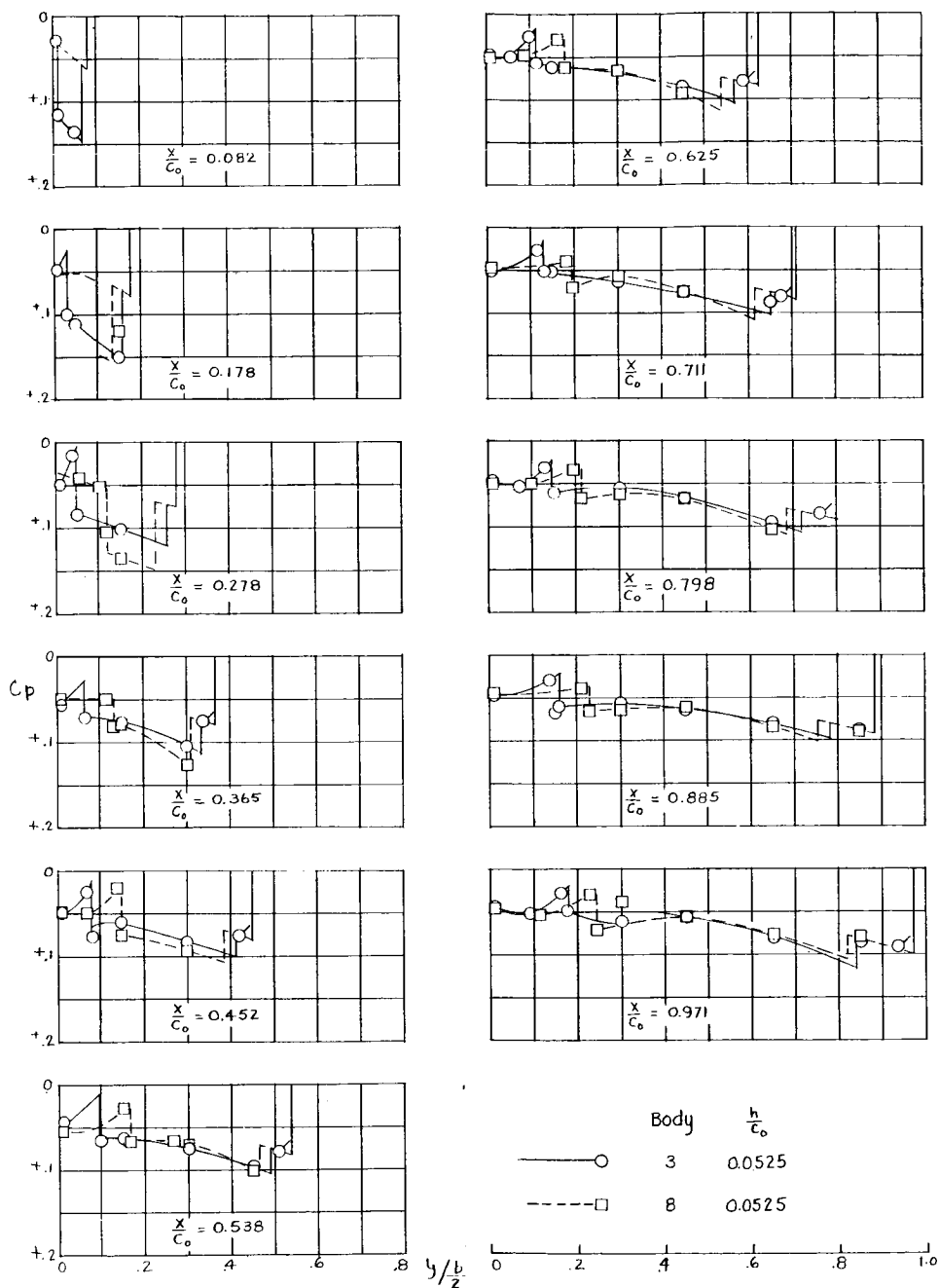
(b) $\alpha = 2^\circ$.

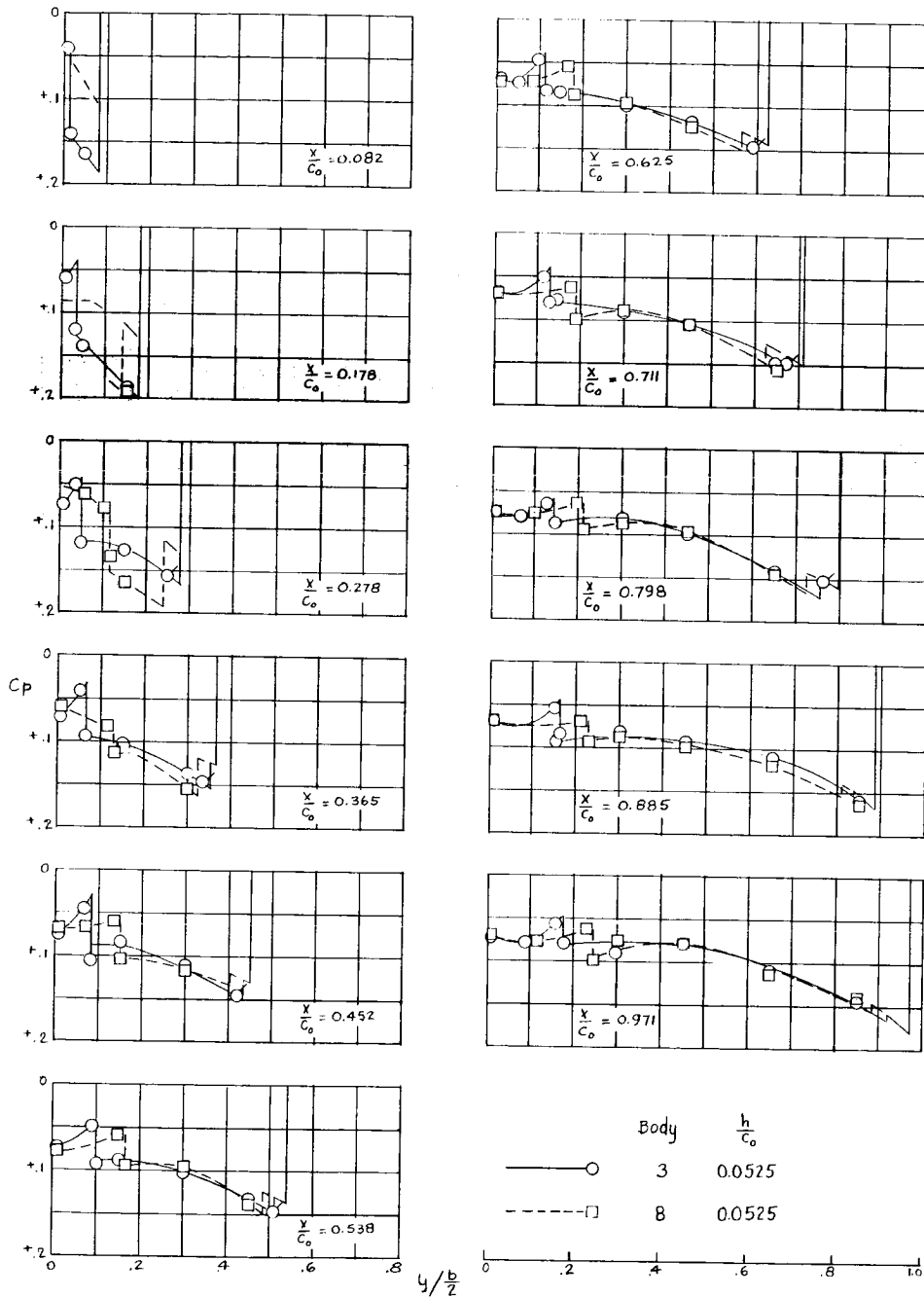
Figure 8.- Continued.

CONFIDENTIAL



(c) $\alpha = 4^\circ$.

Figure 8.- Continued.



(d) $\alpha = 6^\circ$

Figure 8.- Concluded.

CONFIDENTIAL

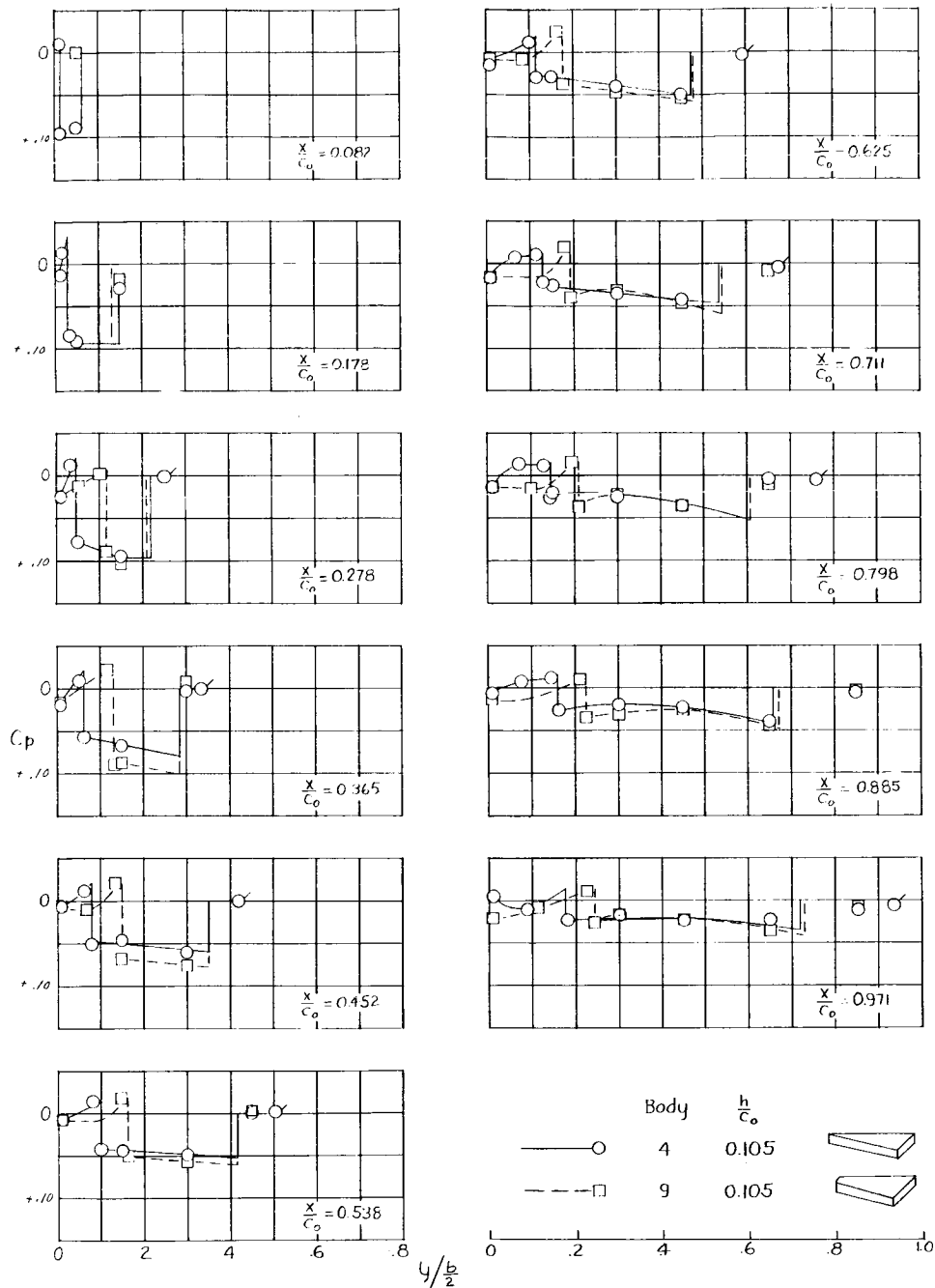
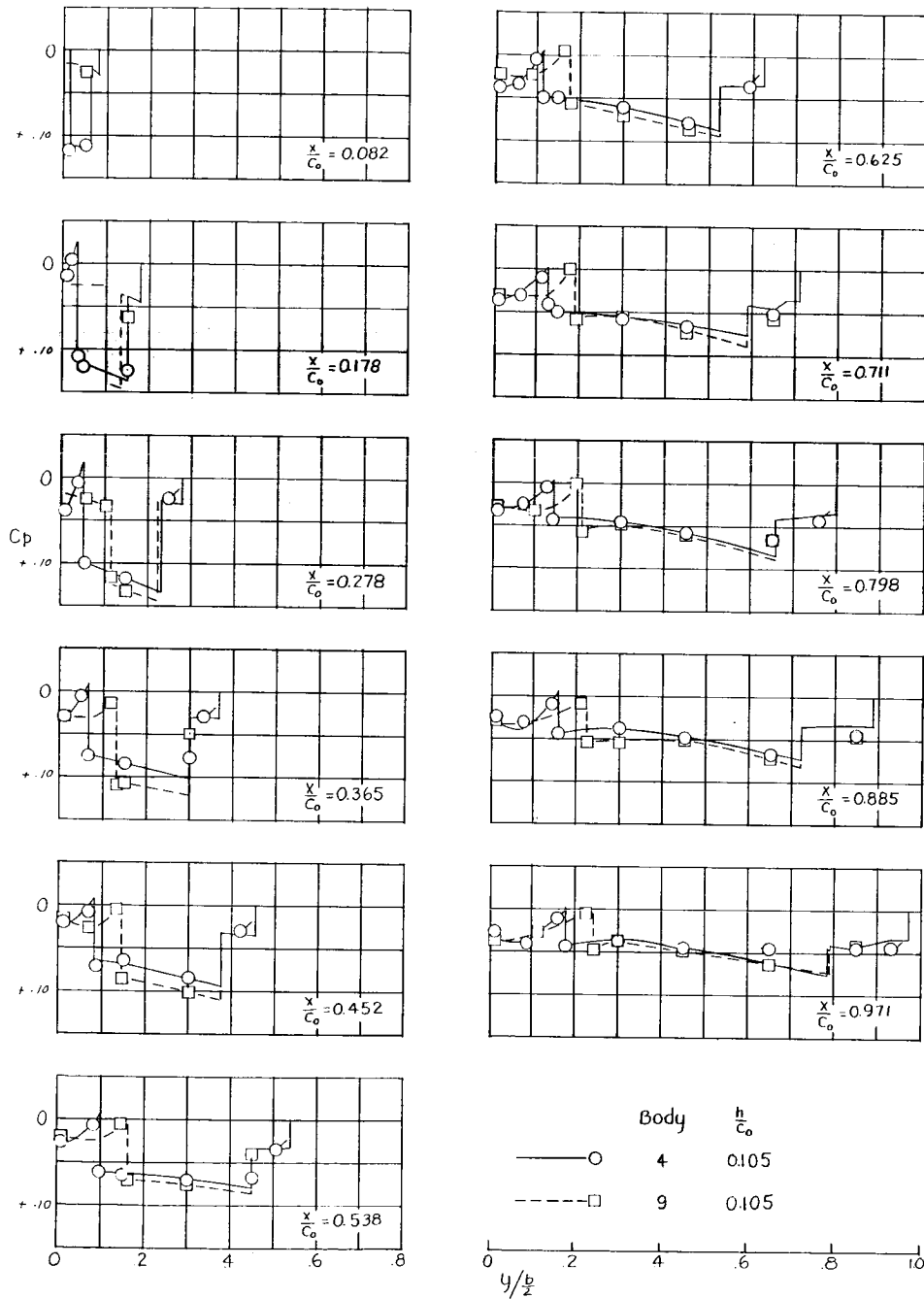


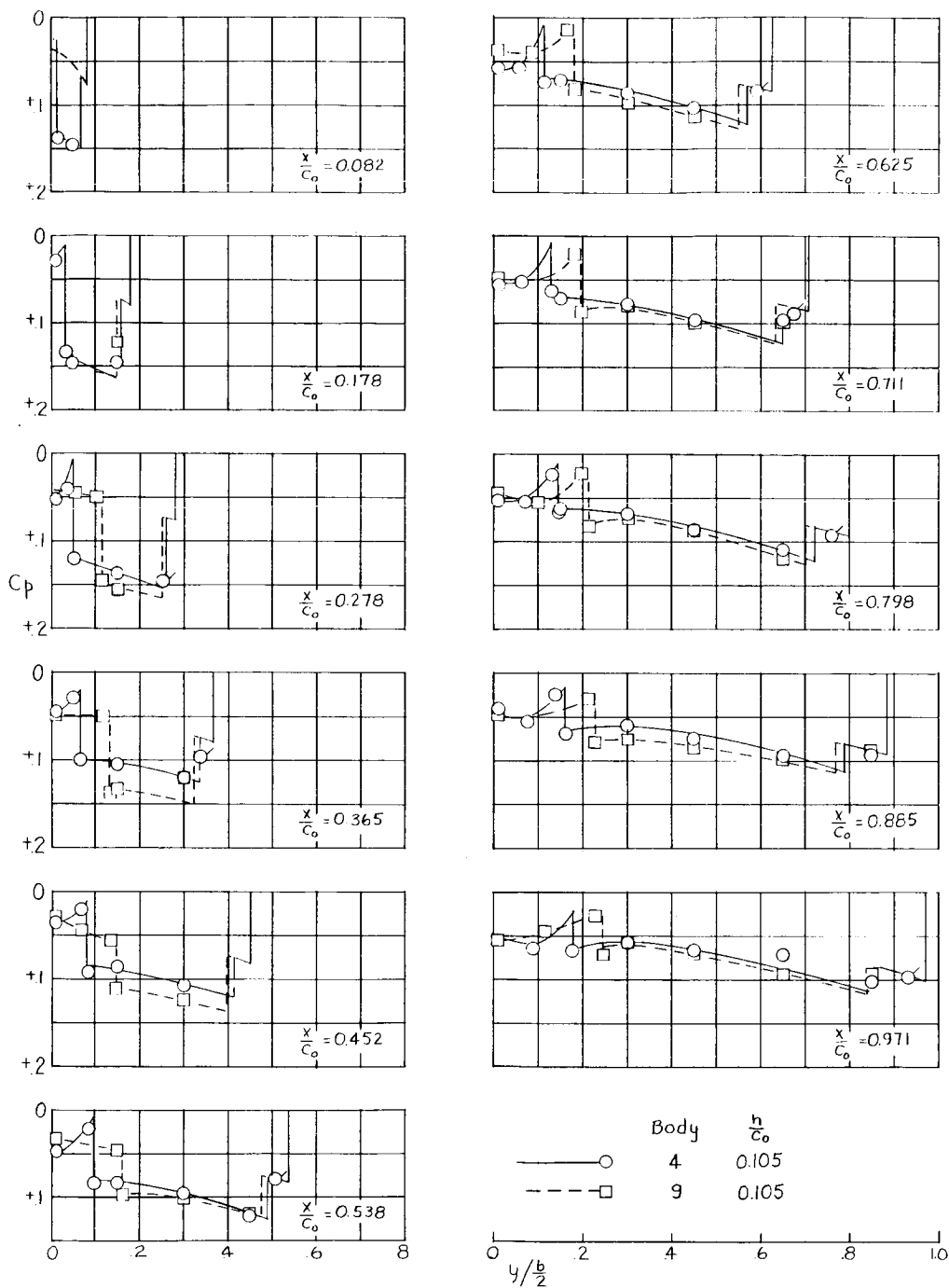
Figure 9.- Pressure distributions on lifting surfaces of wing-body configurations for bodies 4 and 9. Flagged symbols are from faired data.



(b) $\alpha = 2^\circ$.

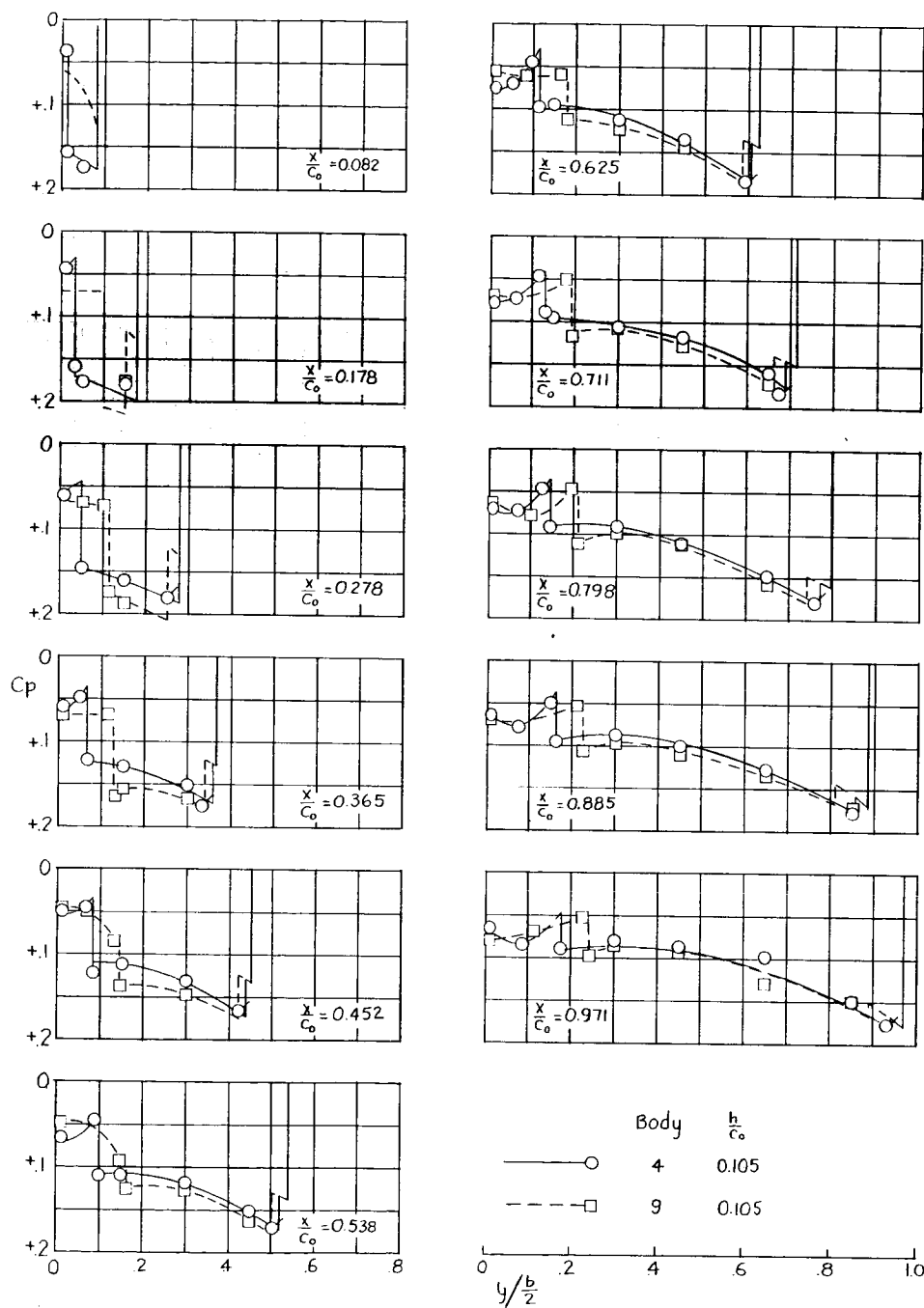
Figure 9.- Continued.

CONFIDENTIAL



(c) $\alpha = 4^\circ$.

Figure 9.- Continued.



(d) $\alpha = 6^\circ$.

Figure 9.- Concluded.

CONFIDENTIAL

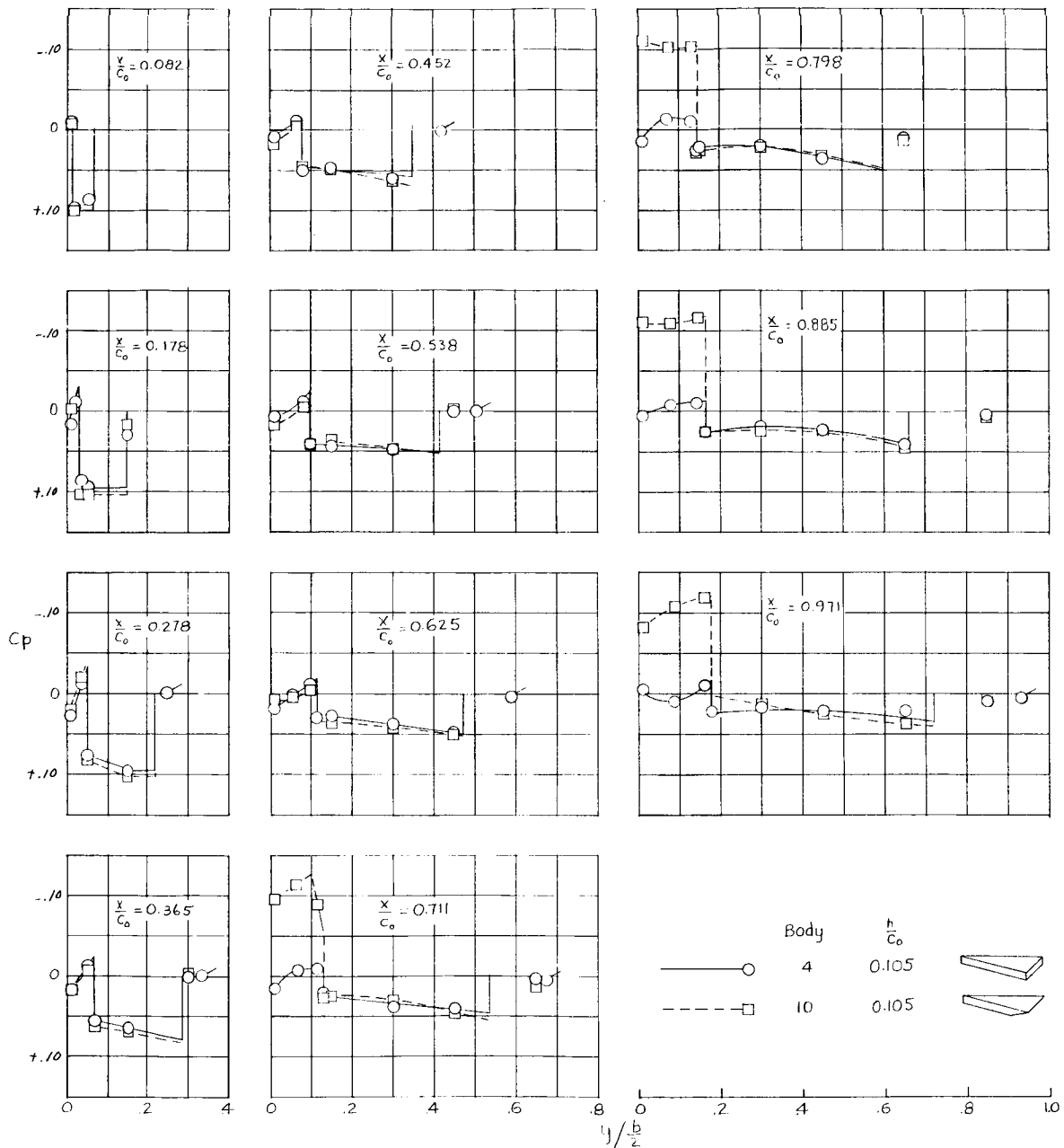


Figure 10.- Pressure distributions on lifting surfaces of wing-body configurations for bodies 4 and 10. Flagged symbols are from faired data.

CONFIDENTIAL

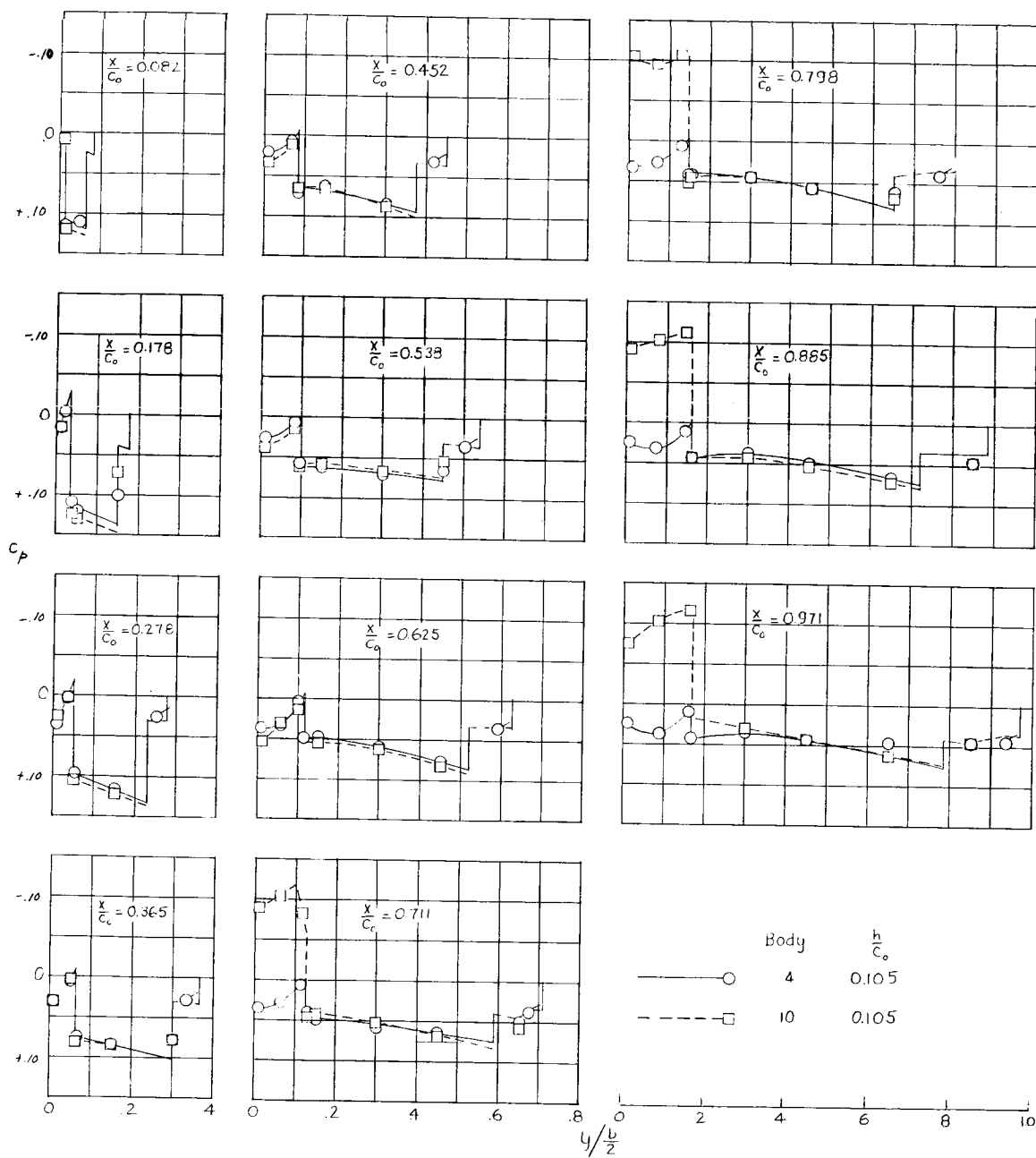


Figure 10.- Continued.

CONFIDENTIAL

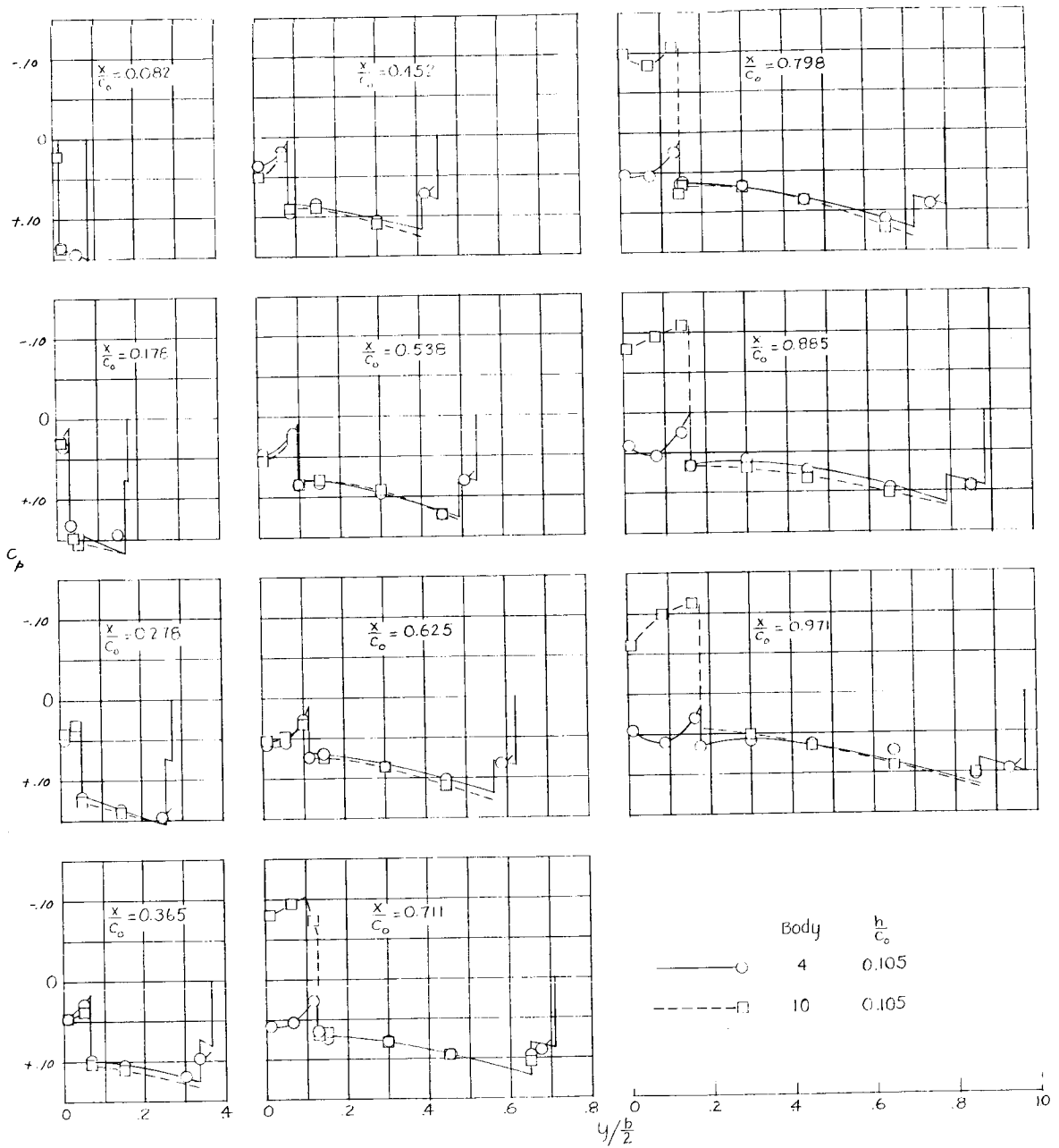
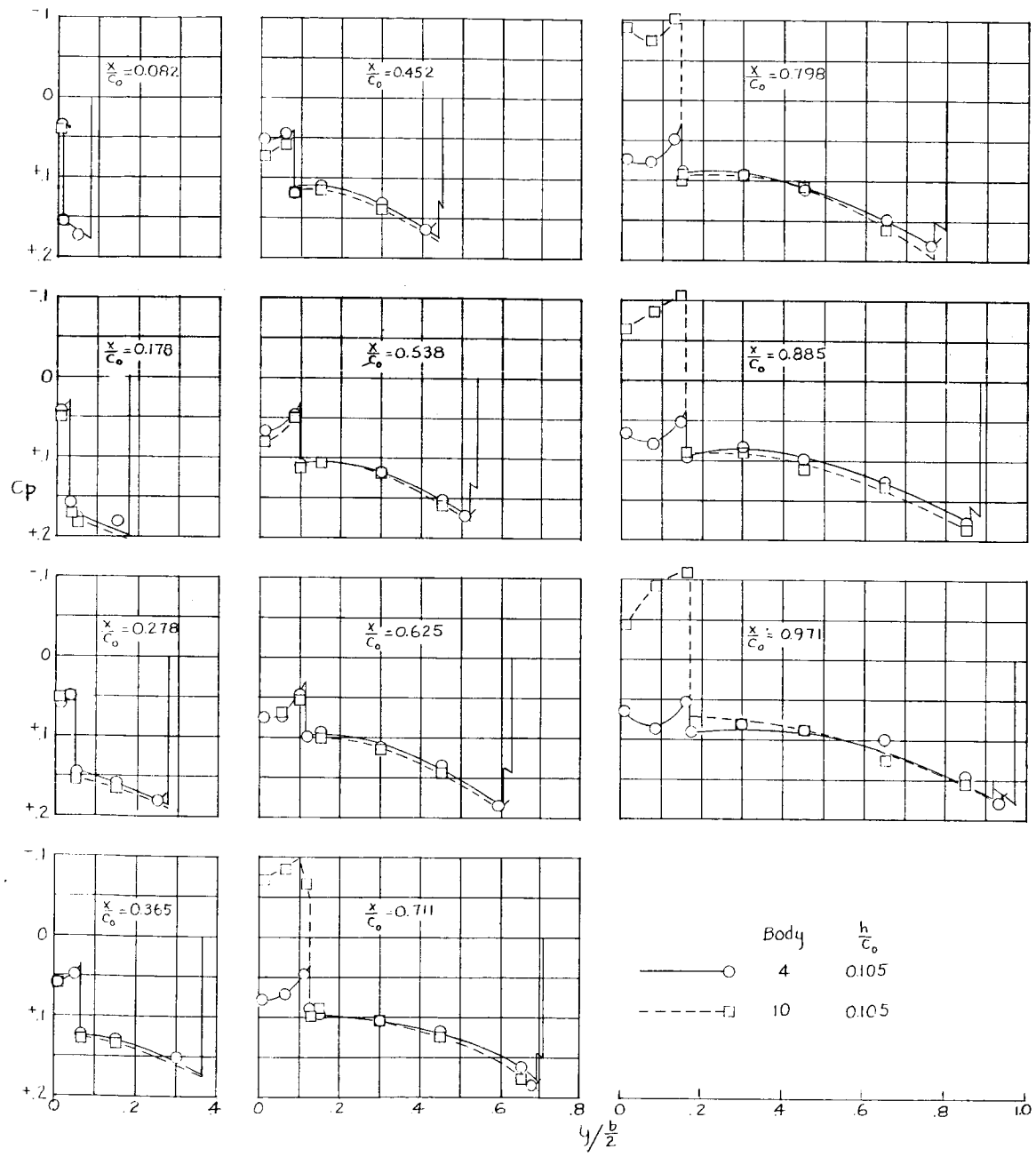
(c) $\alpha = 4^\circ$.

Figure 10.- Continued.



(d) $\alpha = 6^\circ$.

Figure 10.- Concluded.

CONFIDENTIAL

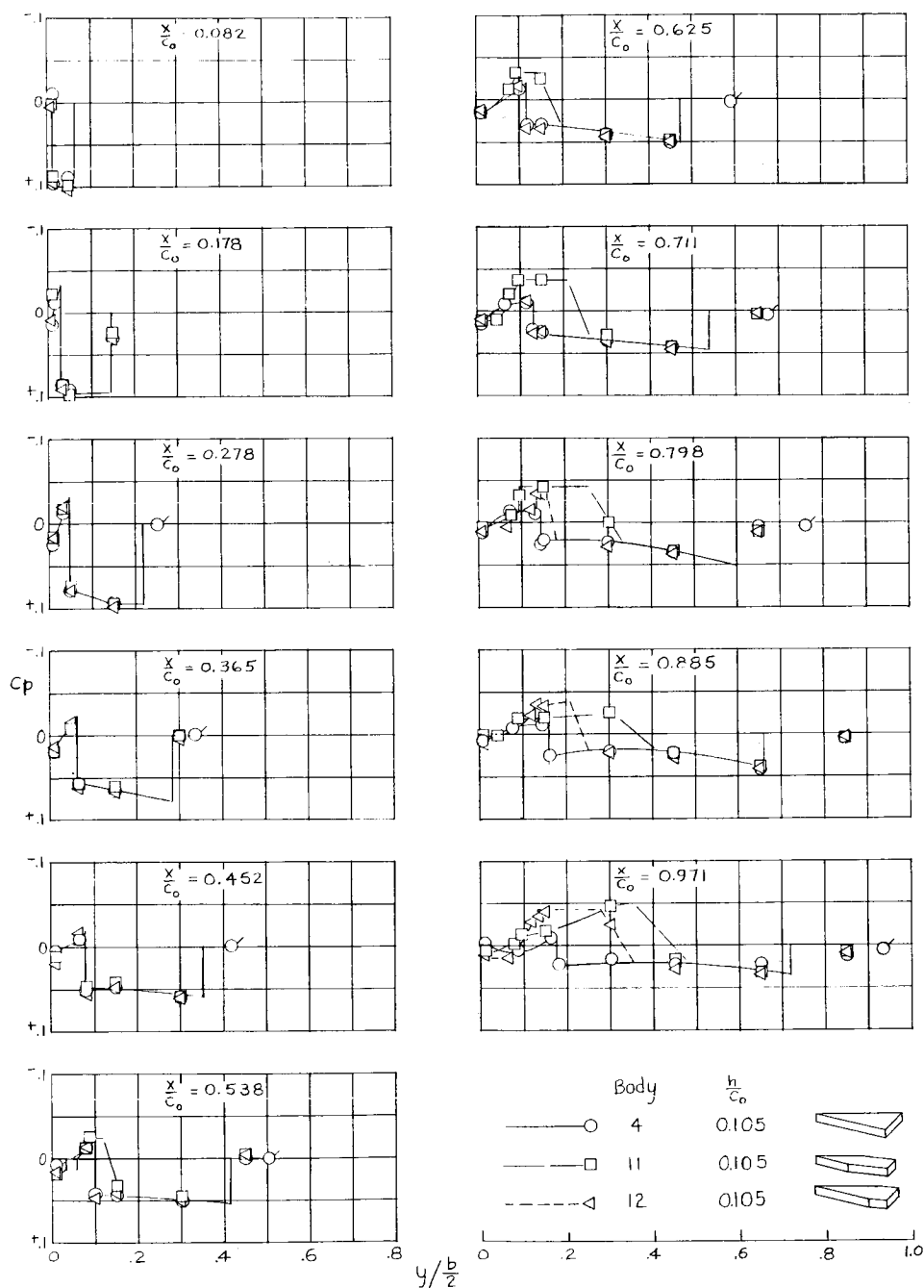


Figure 11.- Pressure distributions on lifting surfaces of wing-body configurations for bodies 4, 11, and 12. Flagged symbols are from faired data.

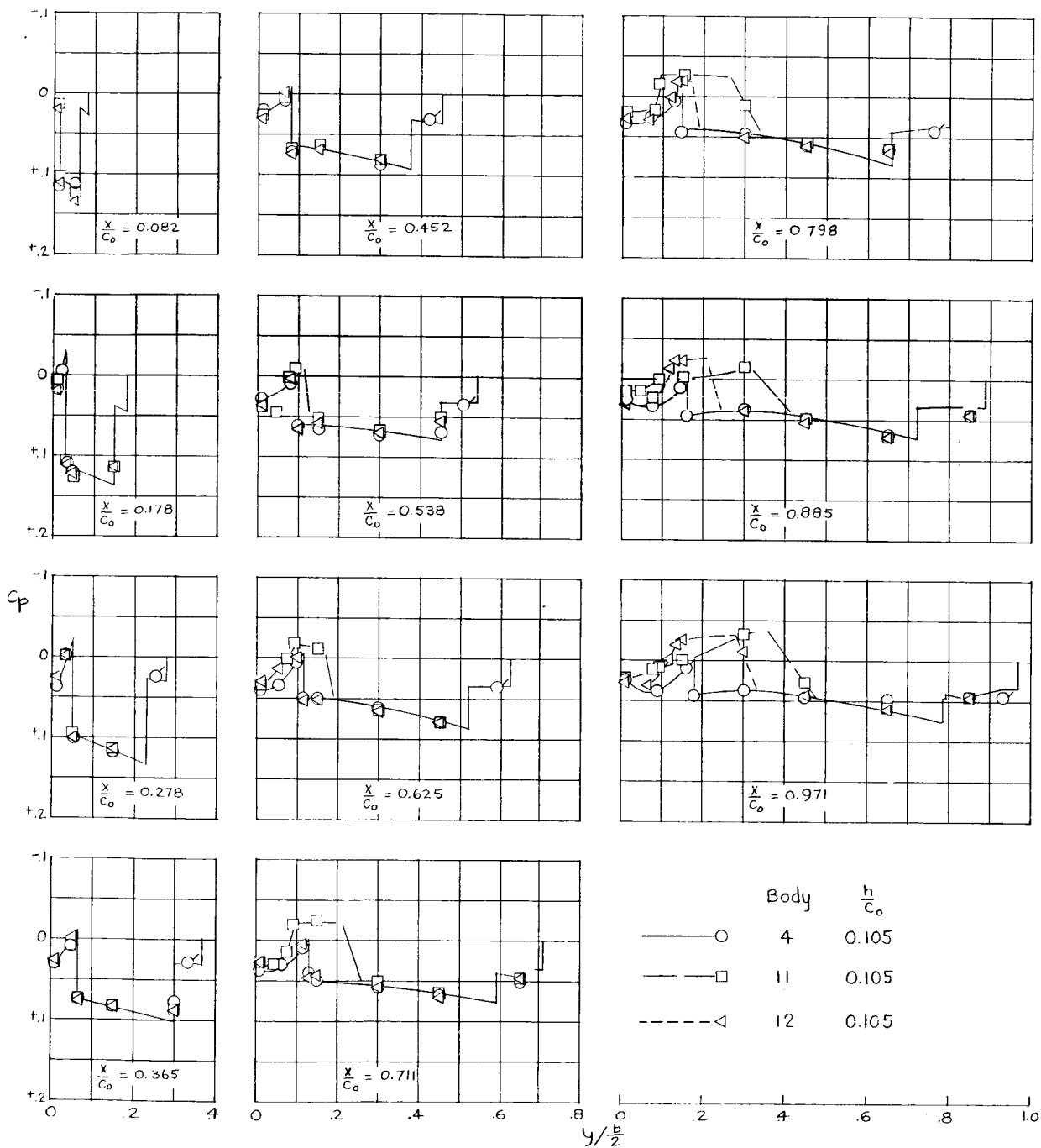
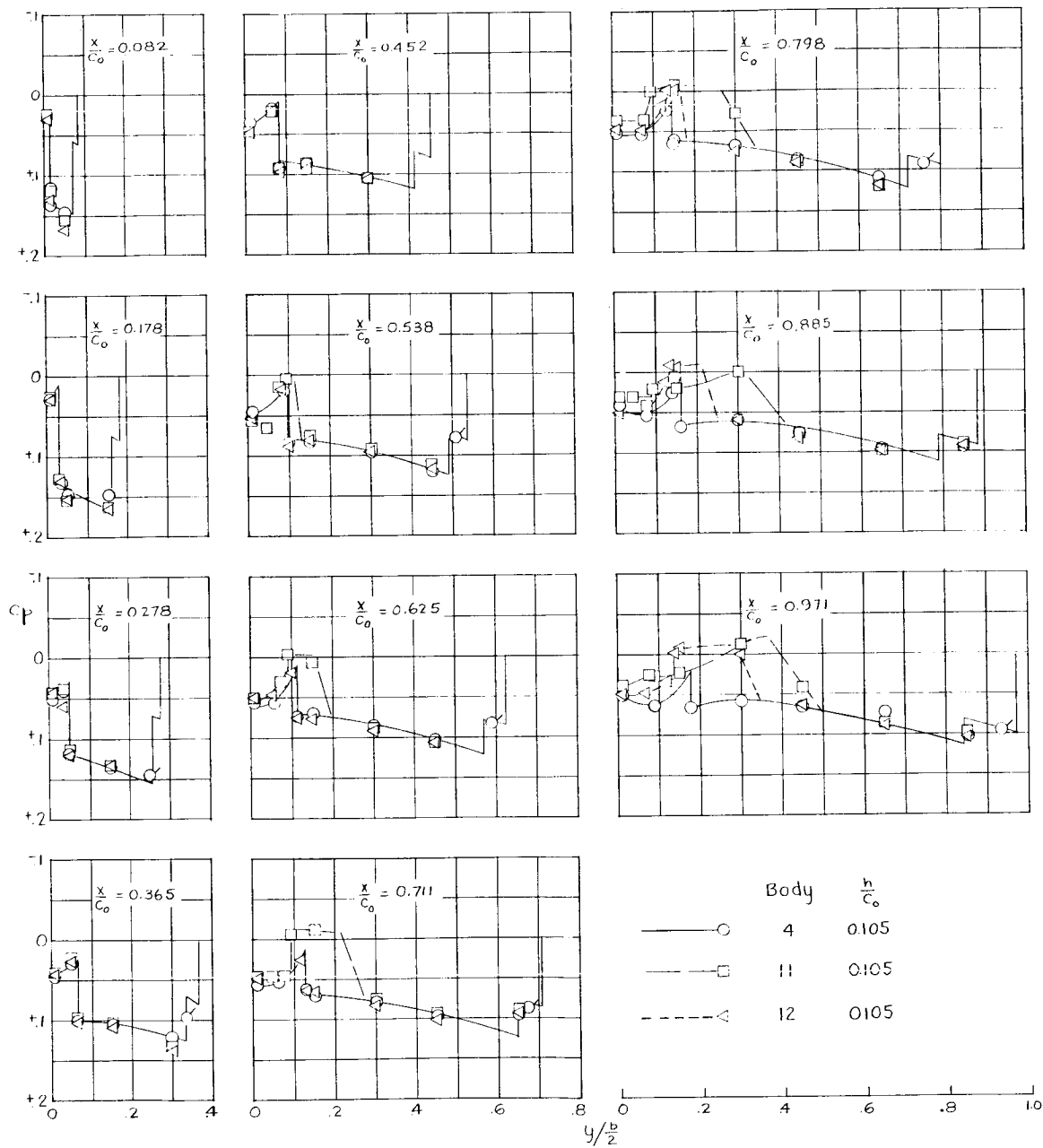


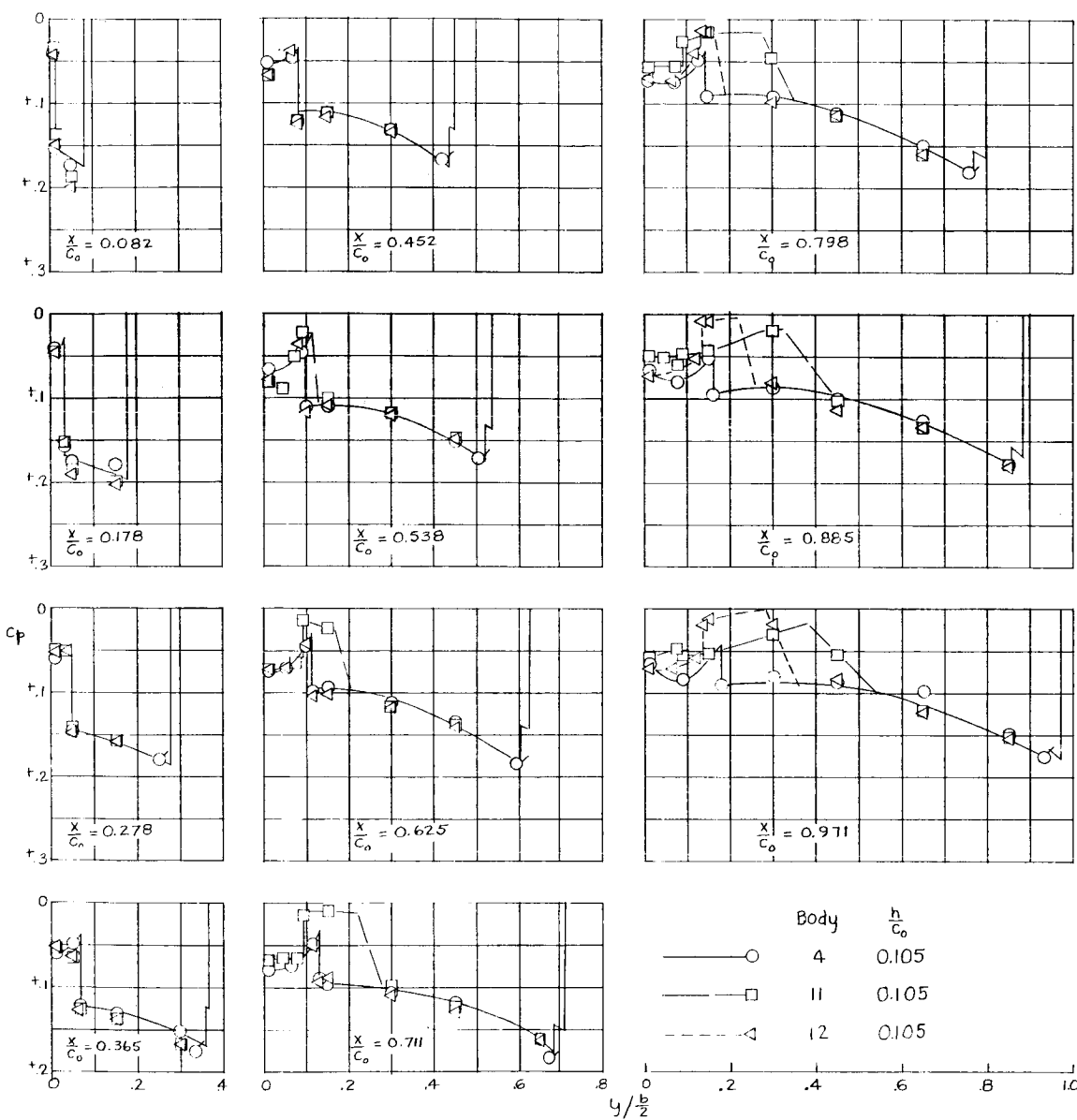
Figure 11.- Continued.

CONFIDENTIAL



(c) $\alpha = 4^\circ$.

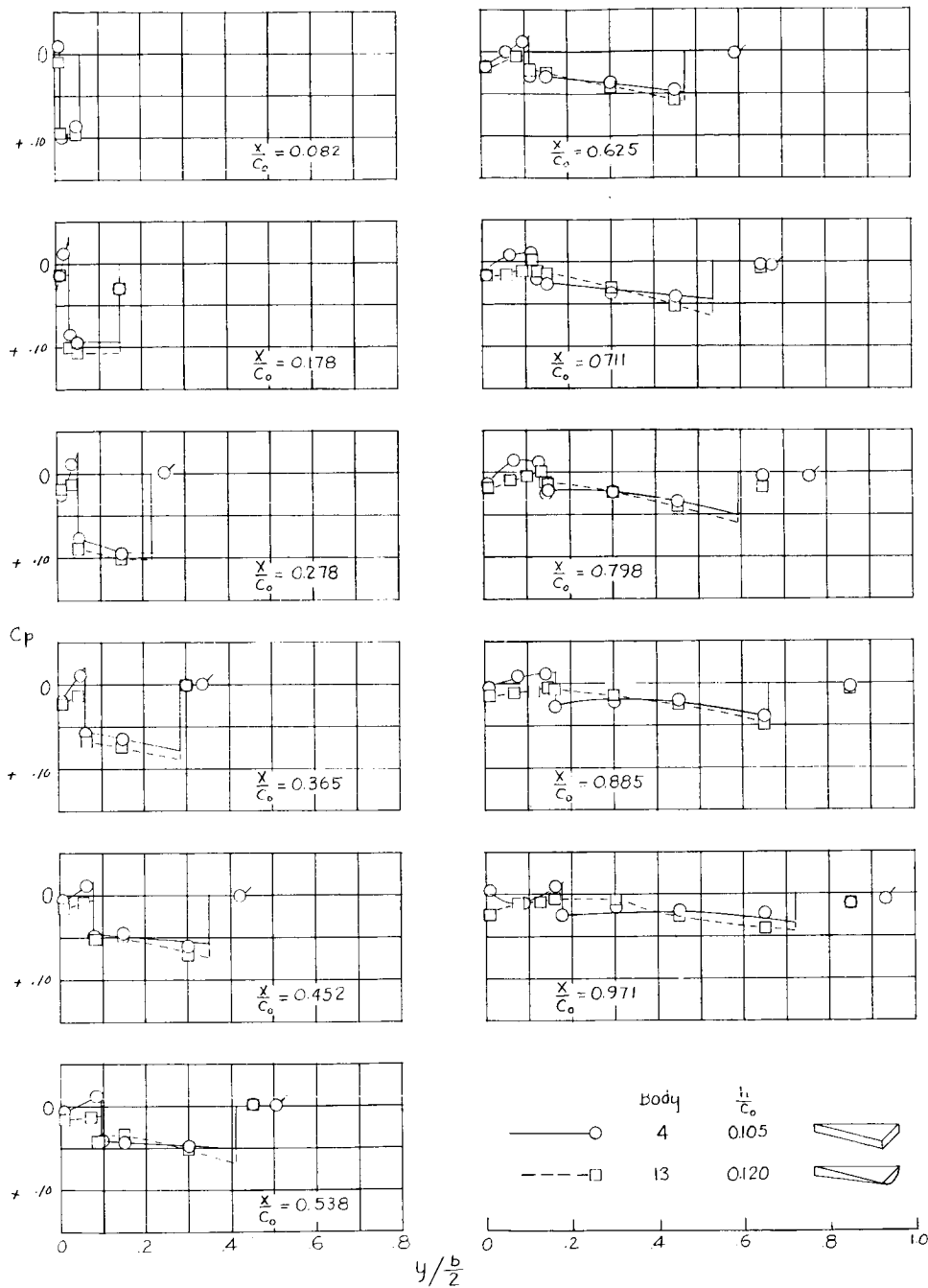
Figure 11.- Continued.



(d) $\alpha = 6^\circ$.

Figure 11.- Concluded.

CONFIDENTIAL



(a) $\alpha = 0^\circ$.

Figure 12.- Pressure distributions on lifting surfaces of wing-body configurations for bodies 4 and 13. Flagged symbols from faired data.

DECLASSIFIED

CONFIDENTIAL

57

L-254

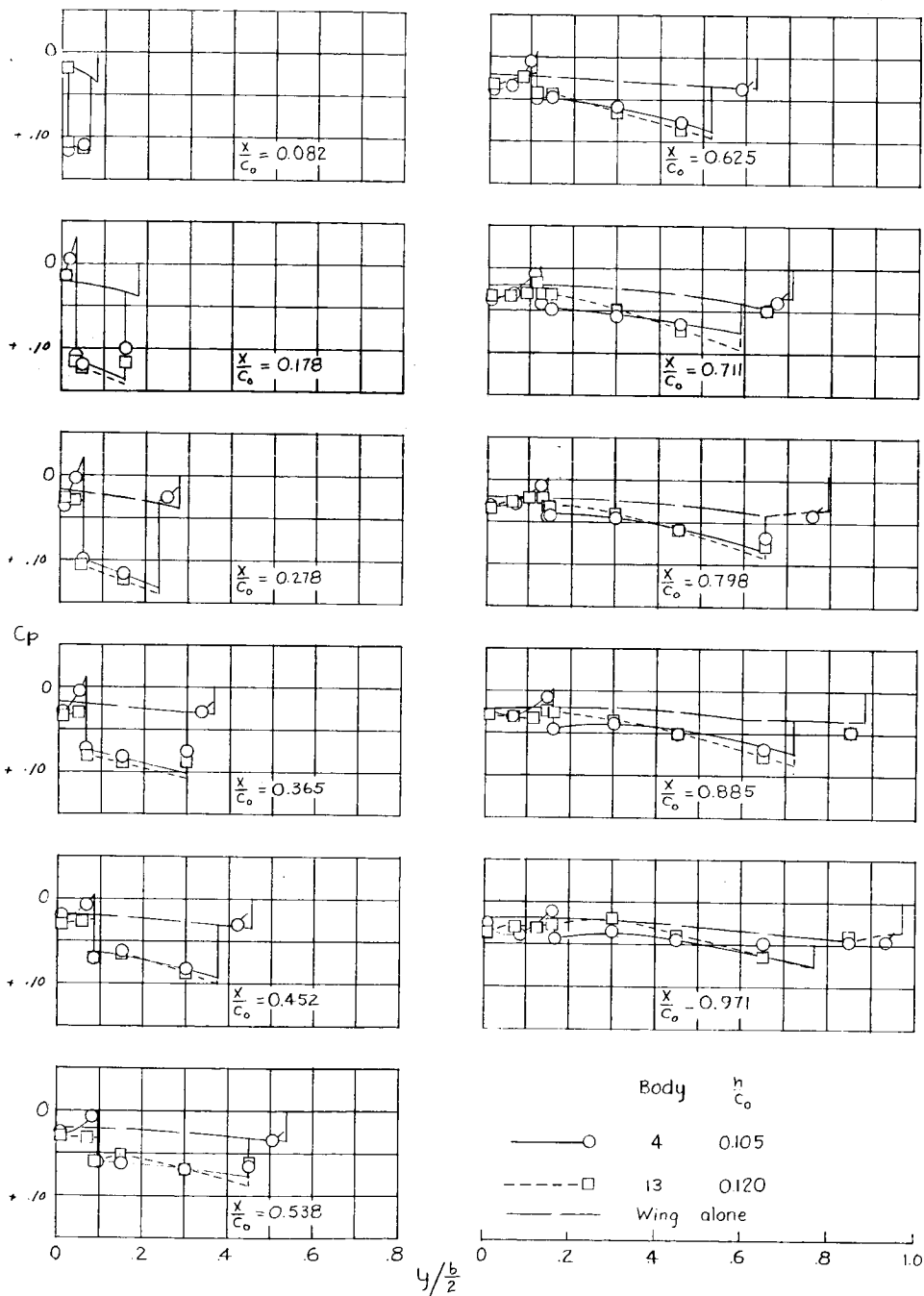
(b) $\alpha = 2^\circ$.

Figure 12.- Continued.

031712 20 1030

CONFIDENTIAL

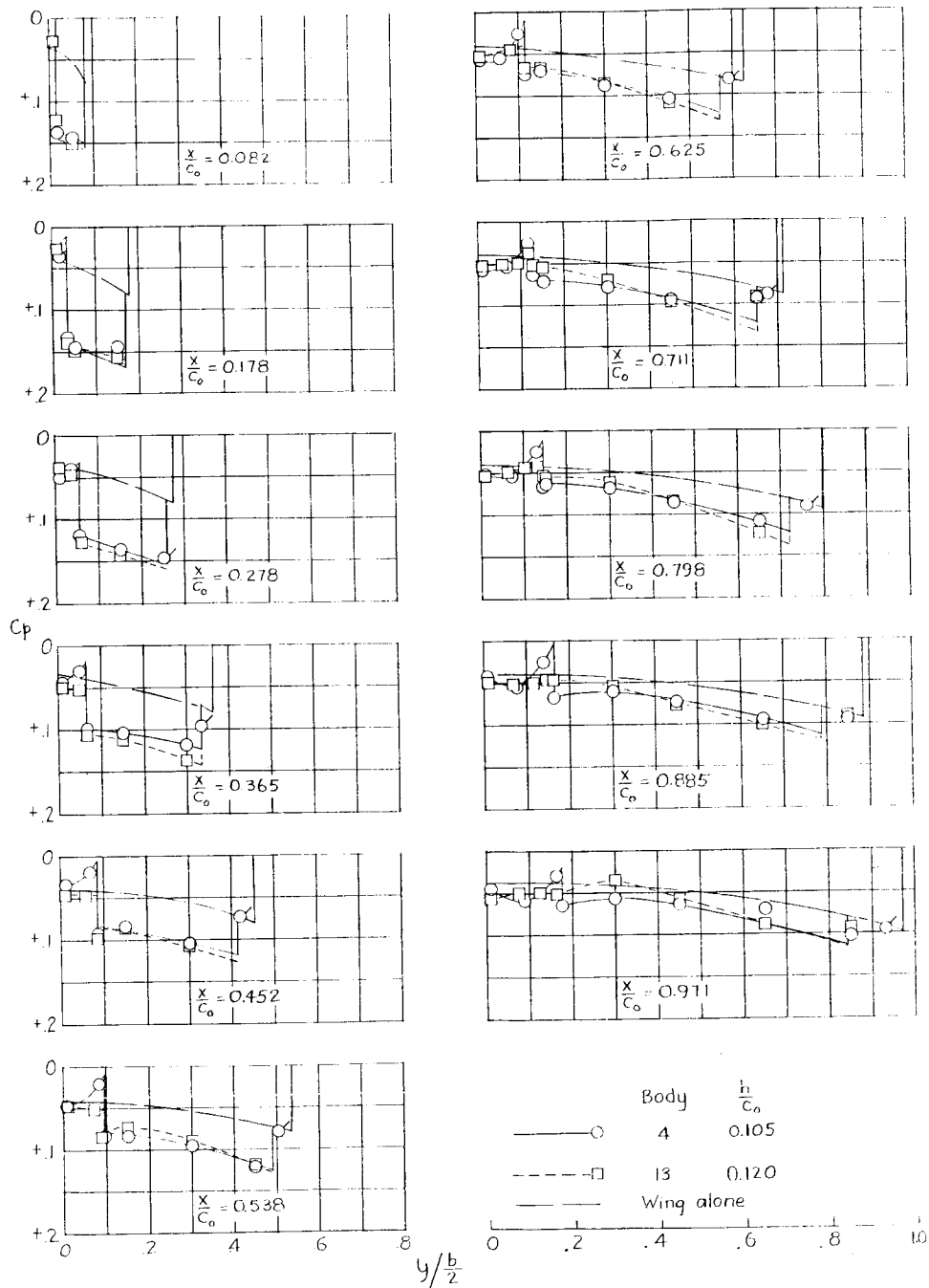
(c) $\alpha = 4^\circ$.

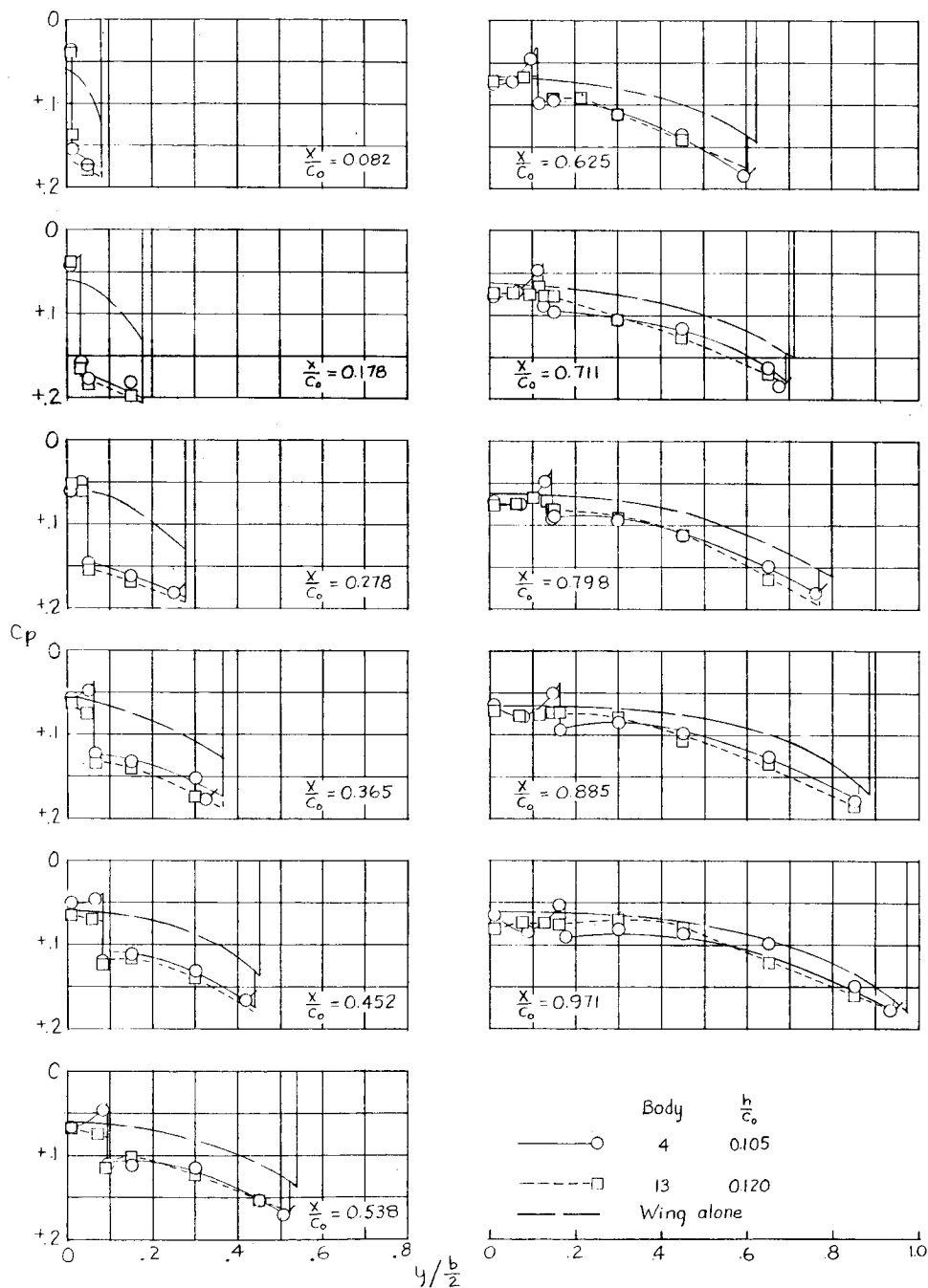
Figure 12.- Continued.

CONFIDENTIAL

DECLASSIFIED

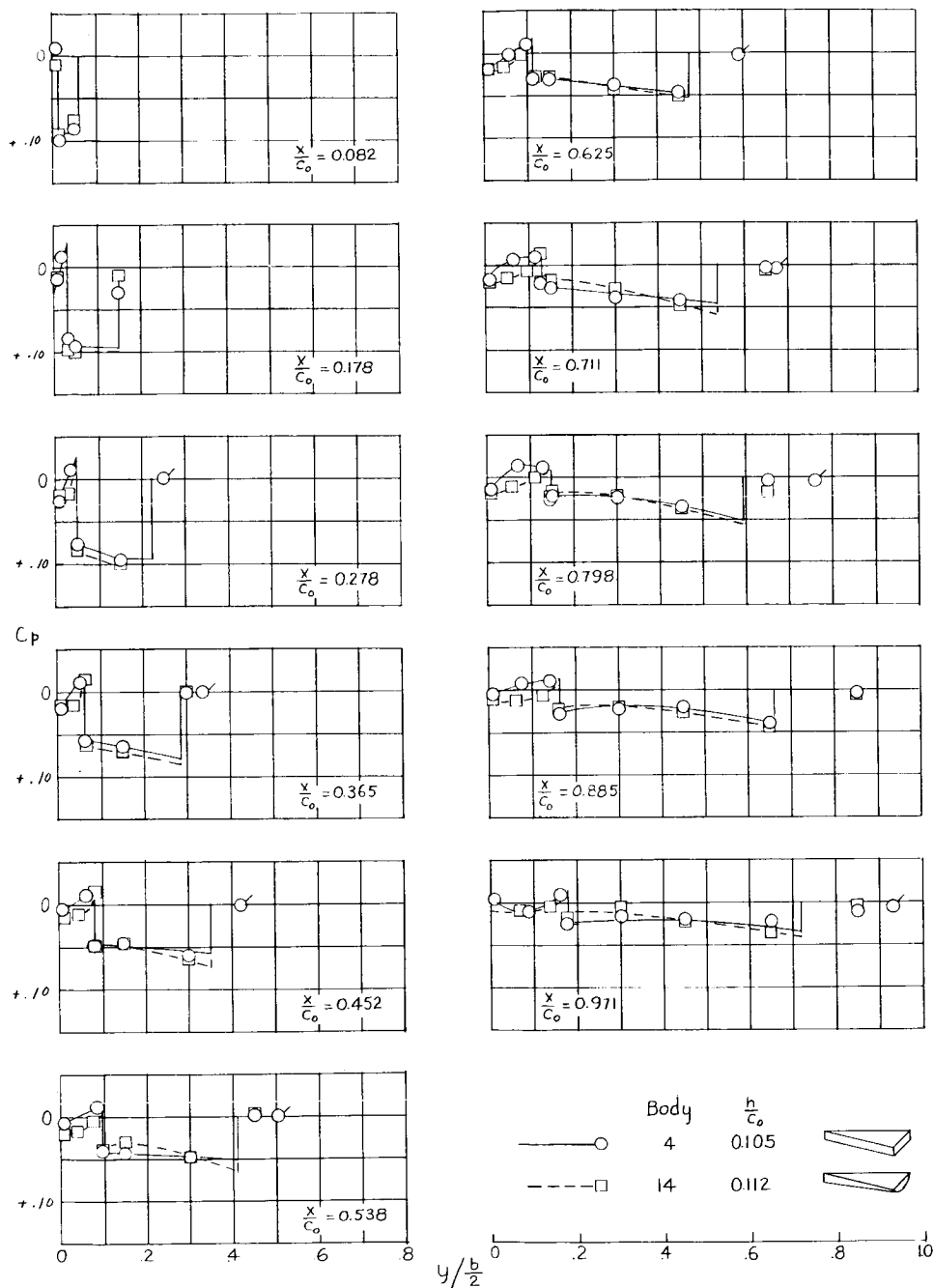
CONFIDENTIAL

59



(d) $\alpha = 6^\circ$.

Figure 12.- Concluded.



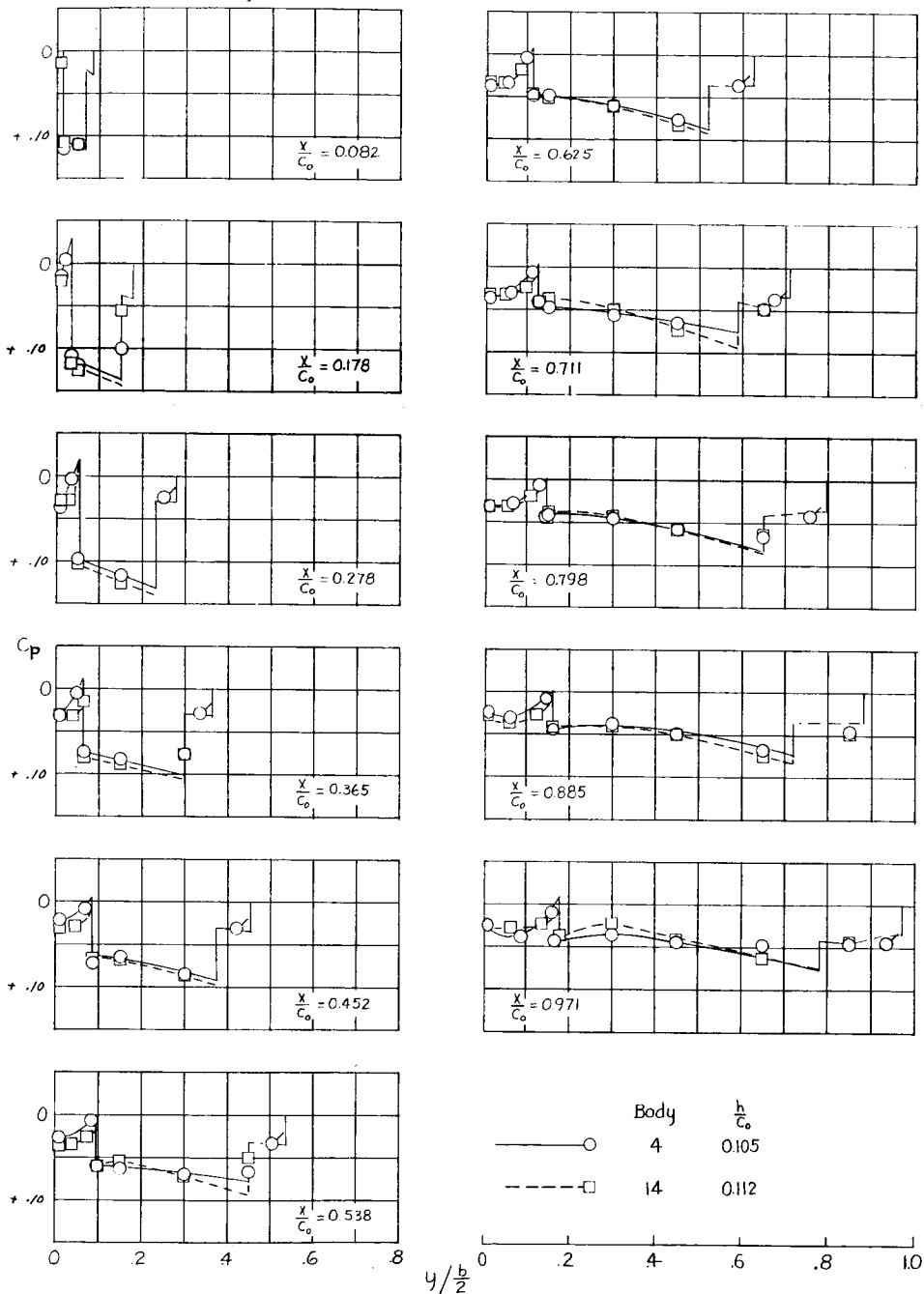
(a) $\alpha = 0^\circ$.

Figure 13.- Pressure distributions on lifting surfaces of wing-body configurations for bodies 4 and 14. Flagged symbols are from faired data.

DECLASSIFIED

CONFIDENTIAL

61



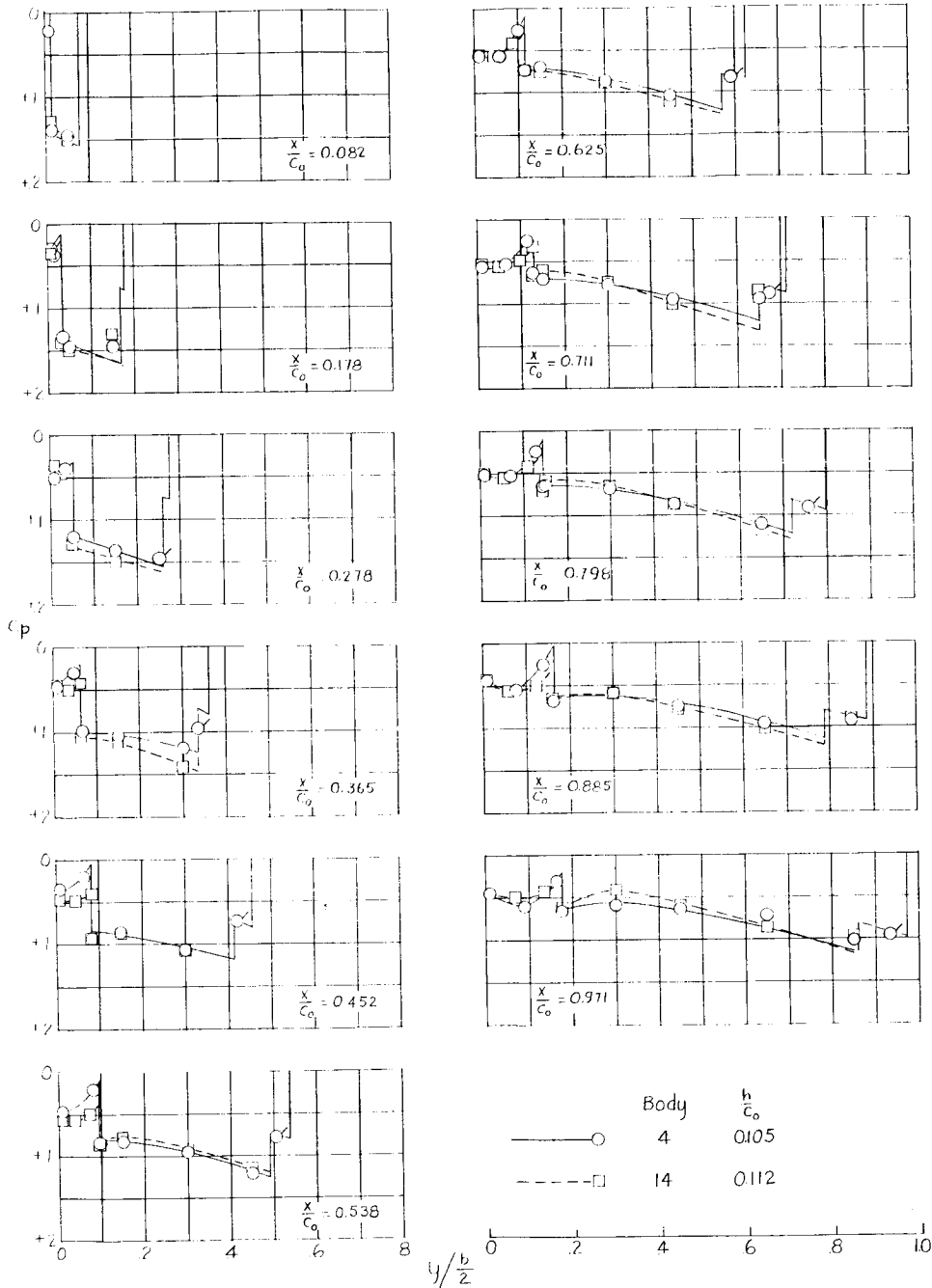
(b) $\alpha = 2^\circ$.

Figure 13.- Continued.

031712201030

62

CONFIDENTIAL



(c) $\alpha = 4^\circ$.

Figure 13.- Continued.

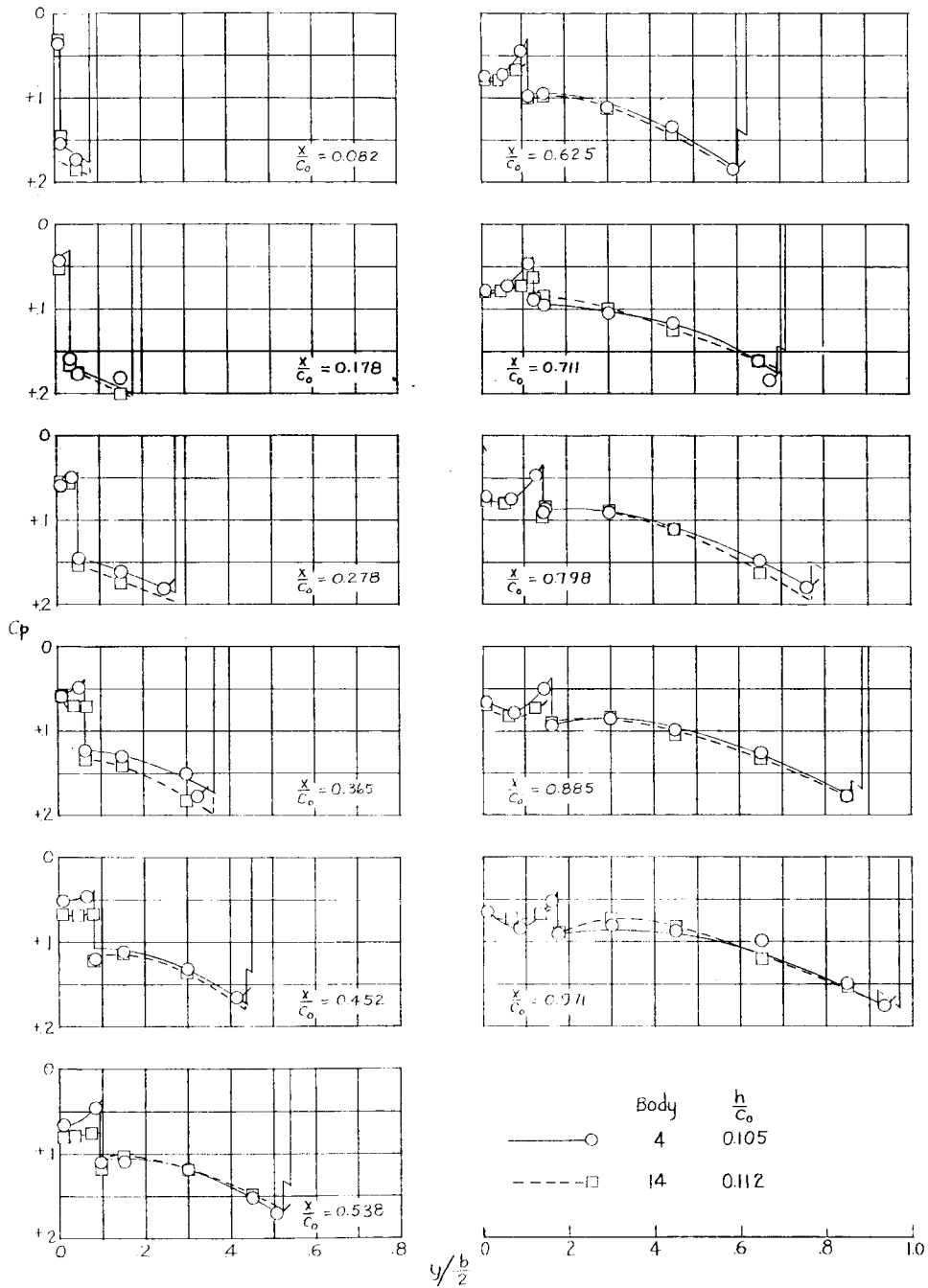
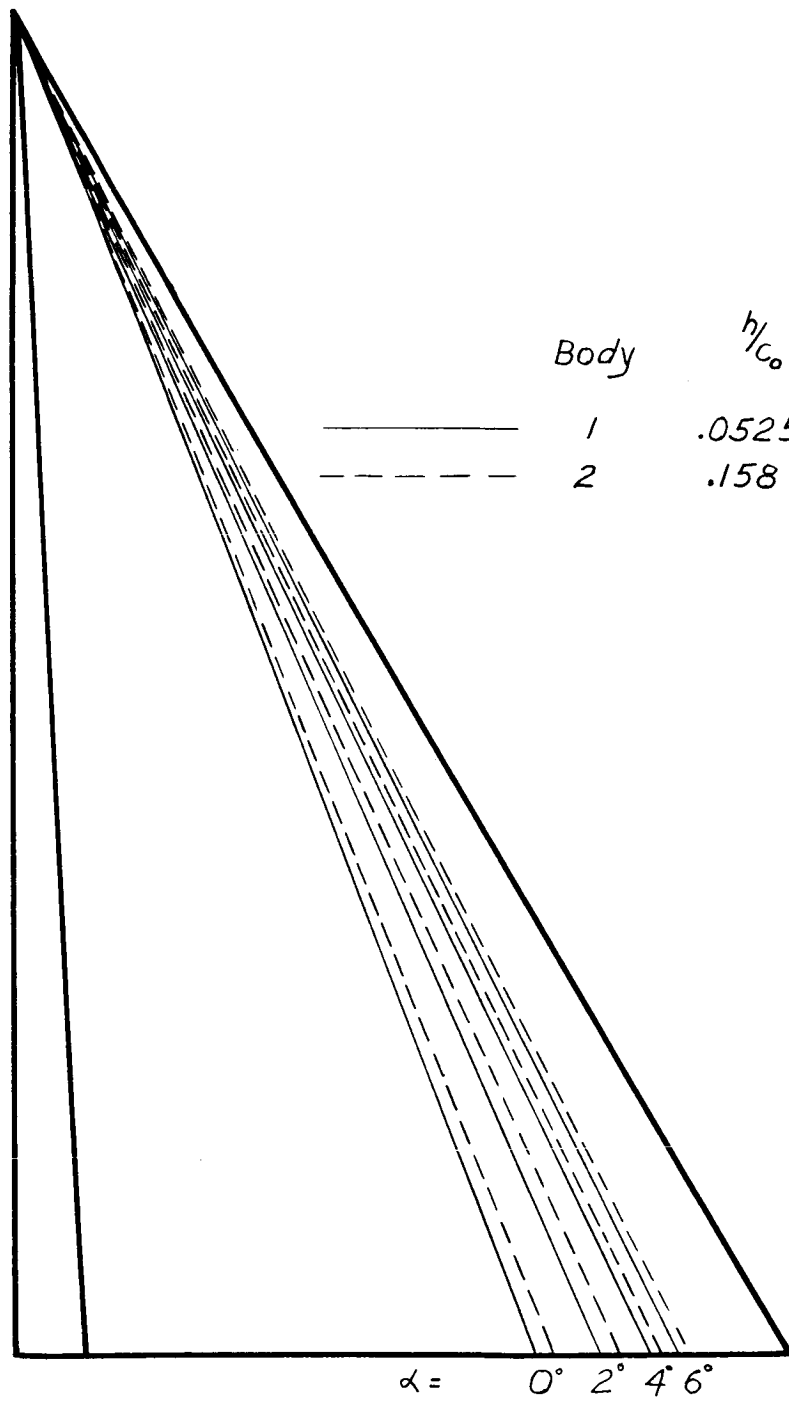


Figure 13.- Concluded.



(a) Bodies 1 and 2; $\delta = 3^\circ$.

Figure 14.- Shock locations for configurations with basic bodies.

DECLASSIFIED

CONFIDENTIAL

65

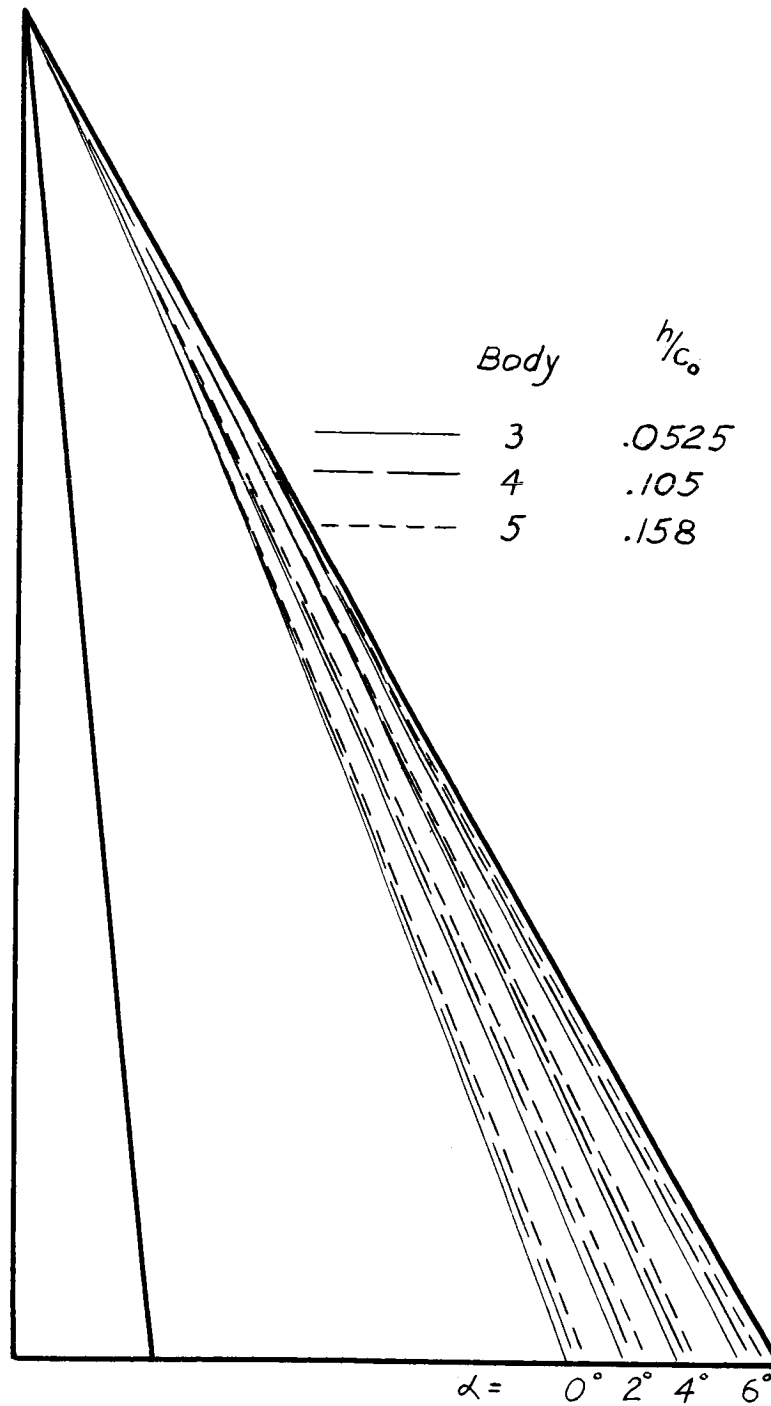
(b) Bodies 3, 4, 5; $\delta = 6^\circ$.

Figure 14.- Continued.

CONFIDENTIAL

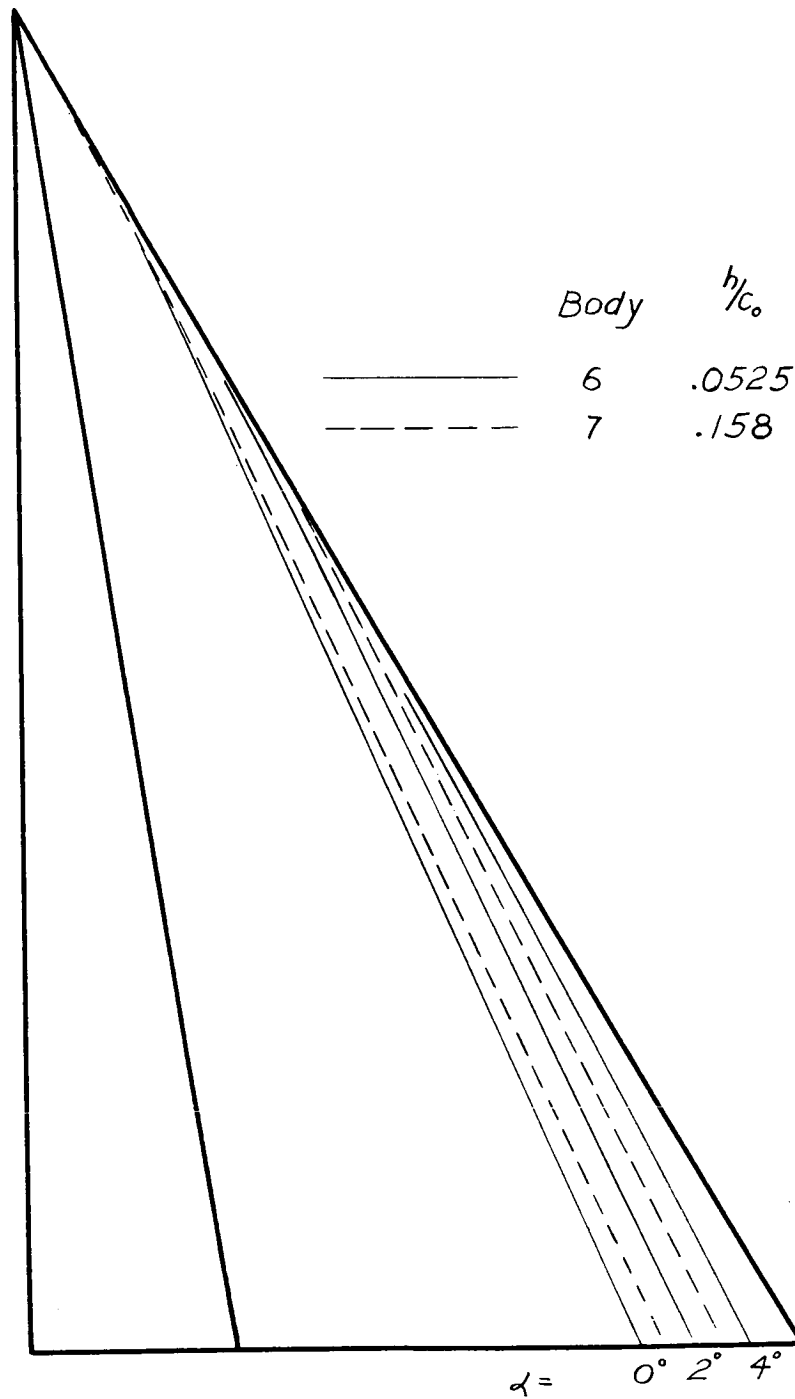
(c) Bodies 6 and 7; $\delta = 90^\circ$.

Figure 14.- Concluded.

[REDACTED]

BODY	$\Delta C_{L,p,\alpha=0^\circ}$			$\Delta C_{L,p, \text{average}}$		
	h/c_o			h/c_o		
	.0525	.105	.158	.0525	.105	.158
1	.0077			.0100		
2			.0186			.0223
3	.0144			.0162		
4		.0244			.0266	
5			.0360			.0400
6	.0230			.0242		
7			.0532			.0582

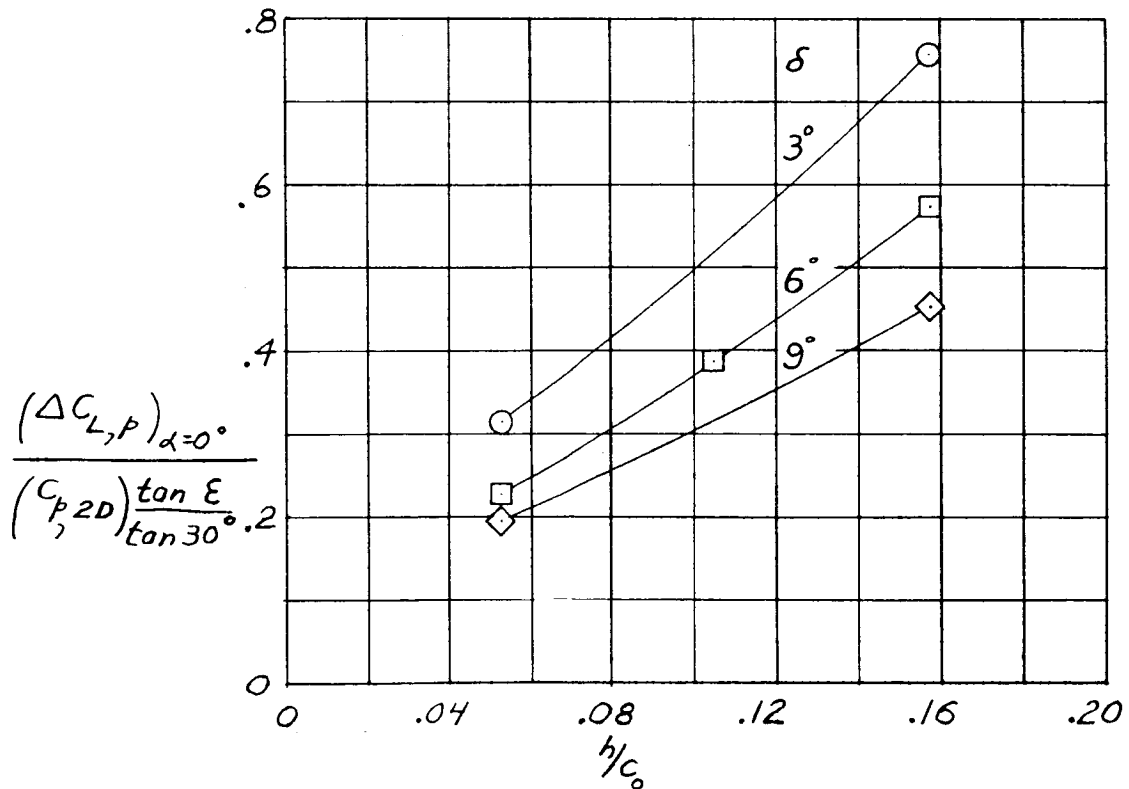
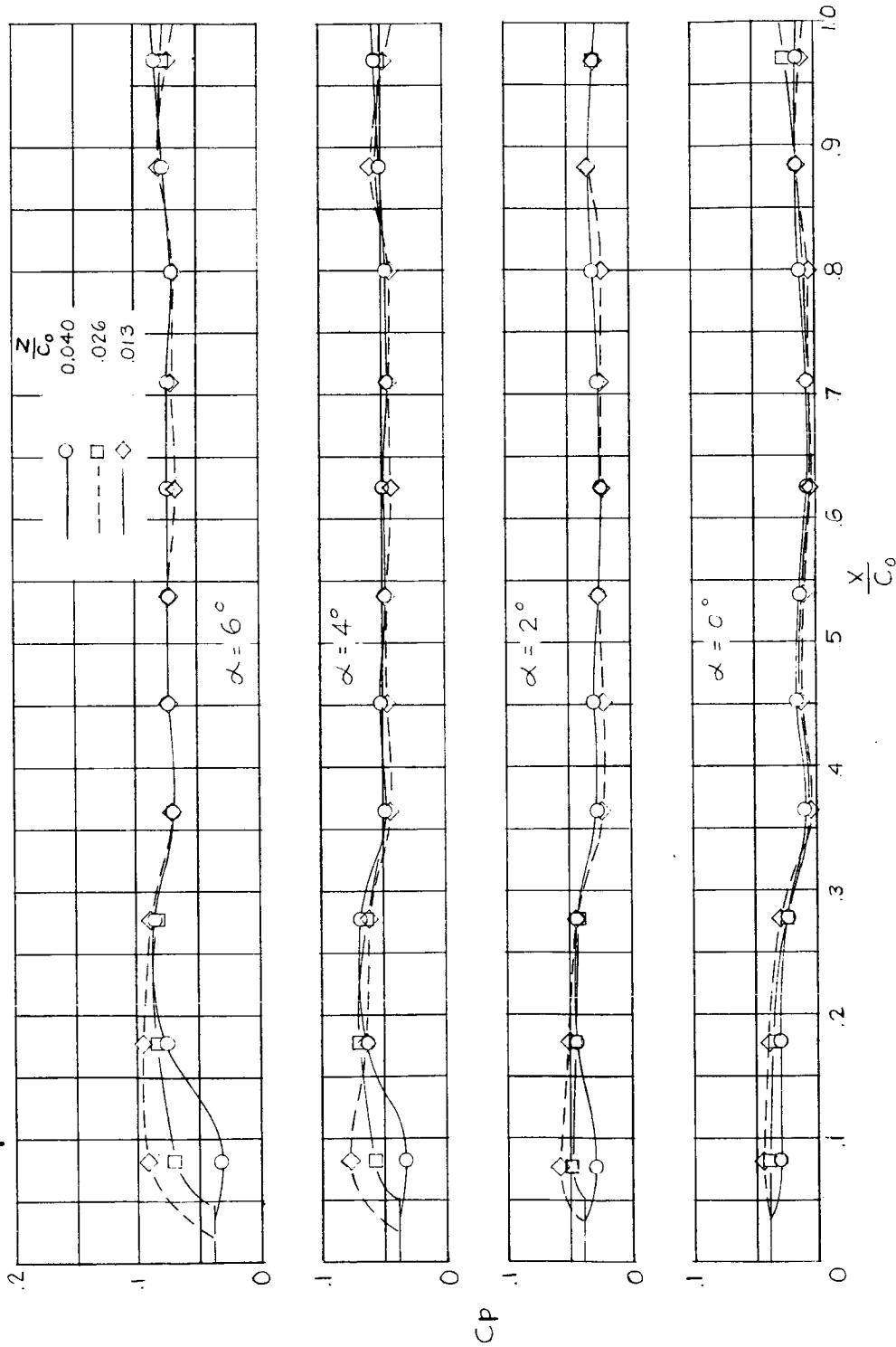


Figure 15.- Variation of interference-lift coefficients with body height and body half-angle.



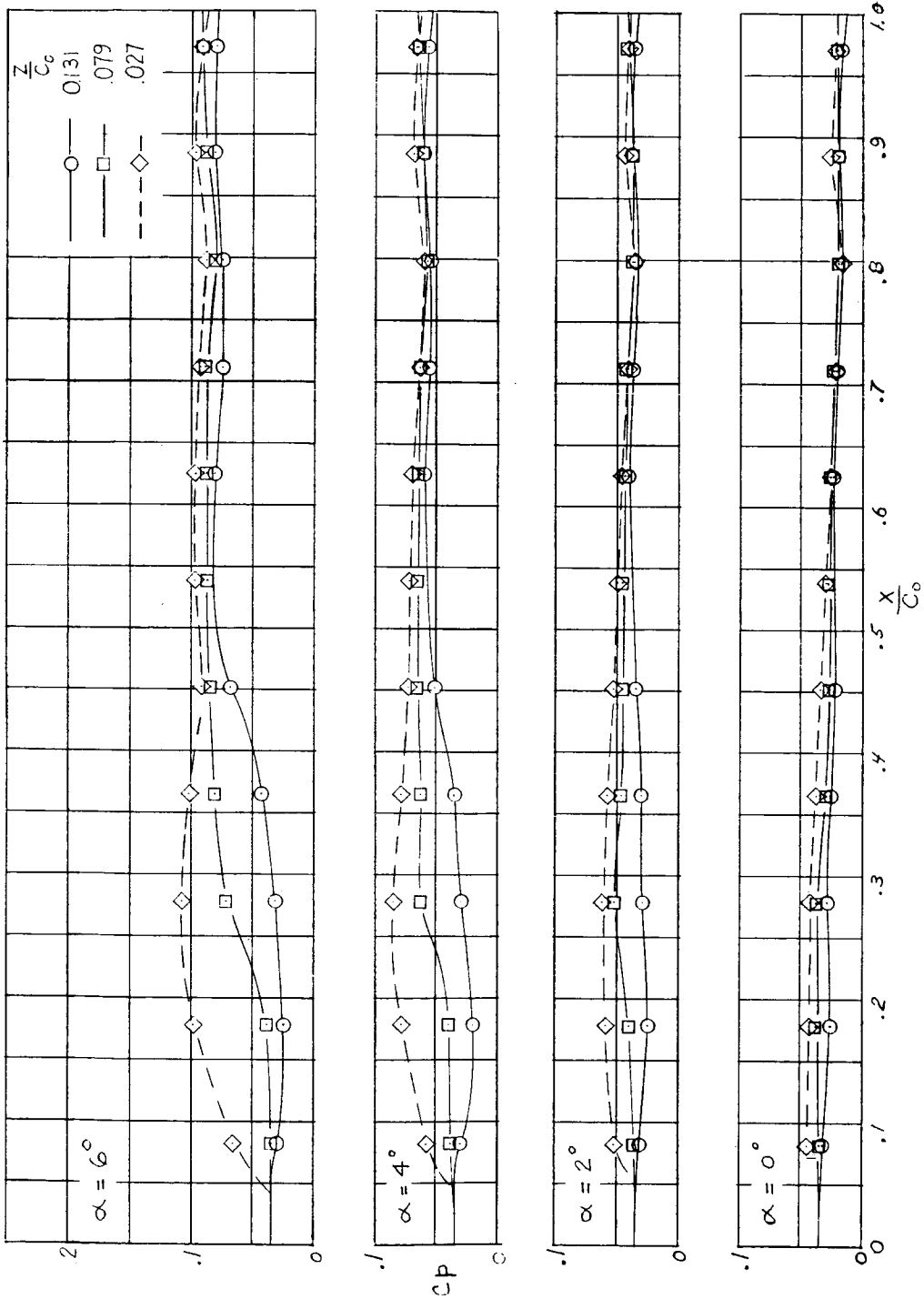
(a) Body 1.

Figure 16.- Pressure distributions on chord-force surfaces of bodies.

DECLASSIFIED

CONFIDENTIAL

69

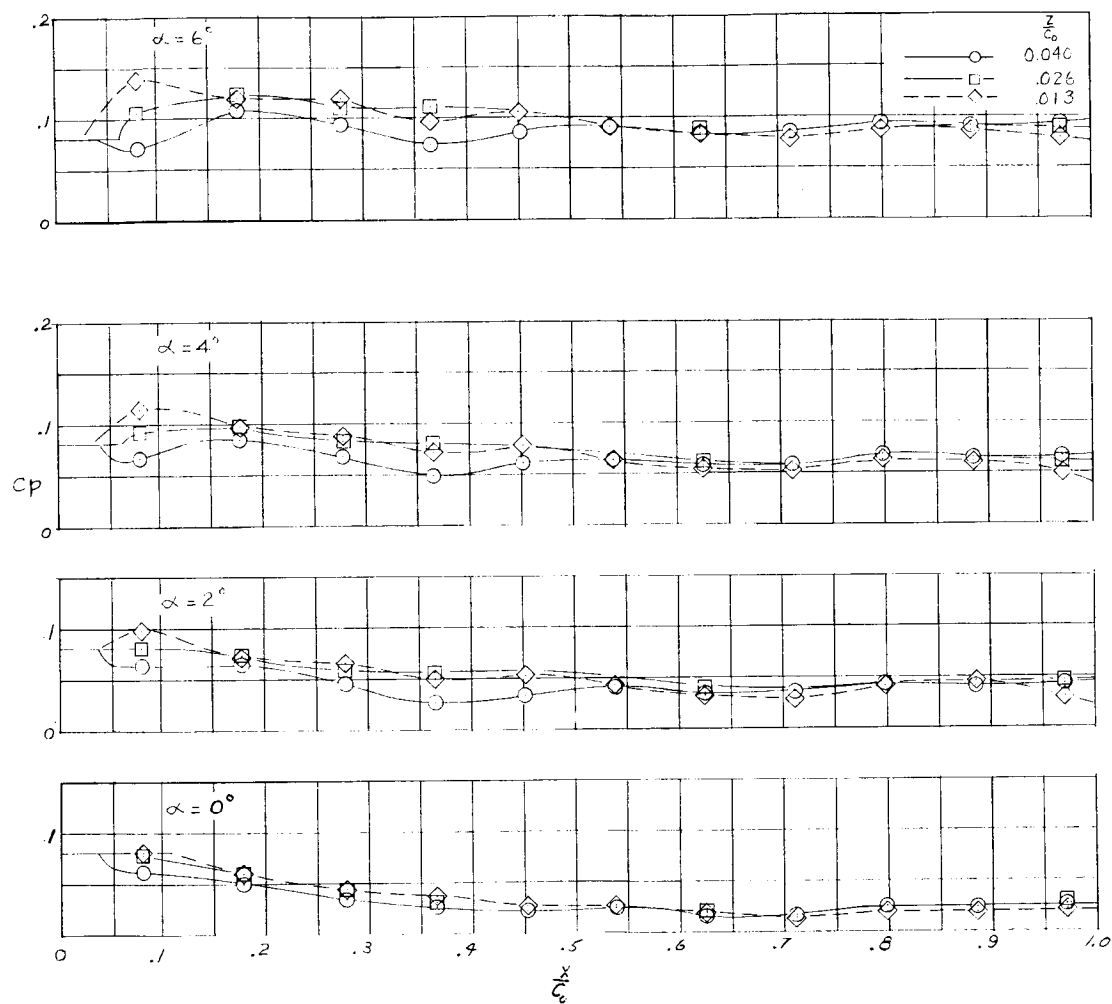


(b) Body 2.

Figure 16.- Continued.

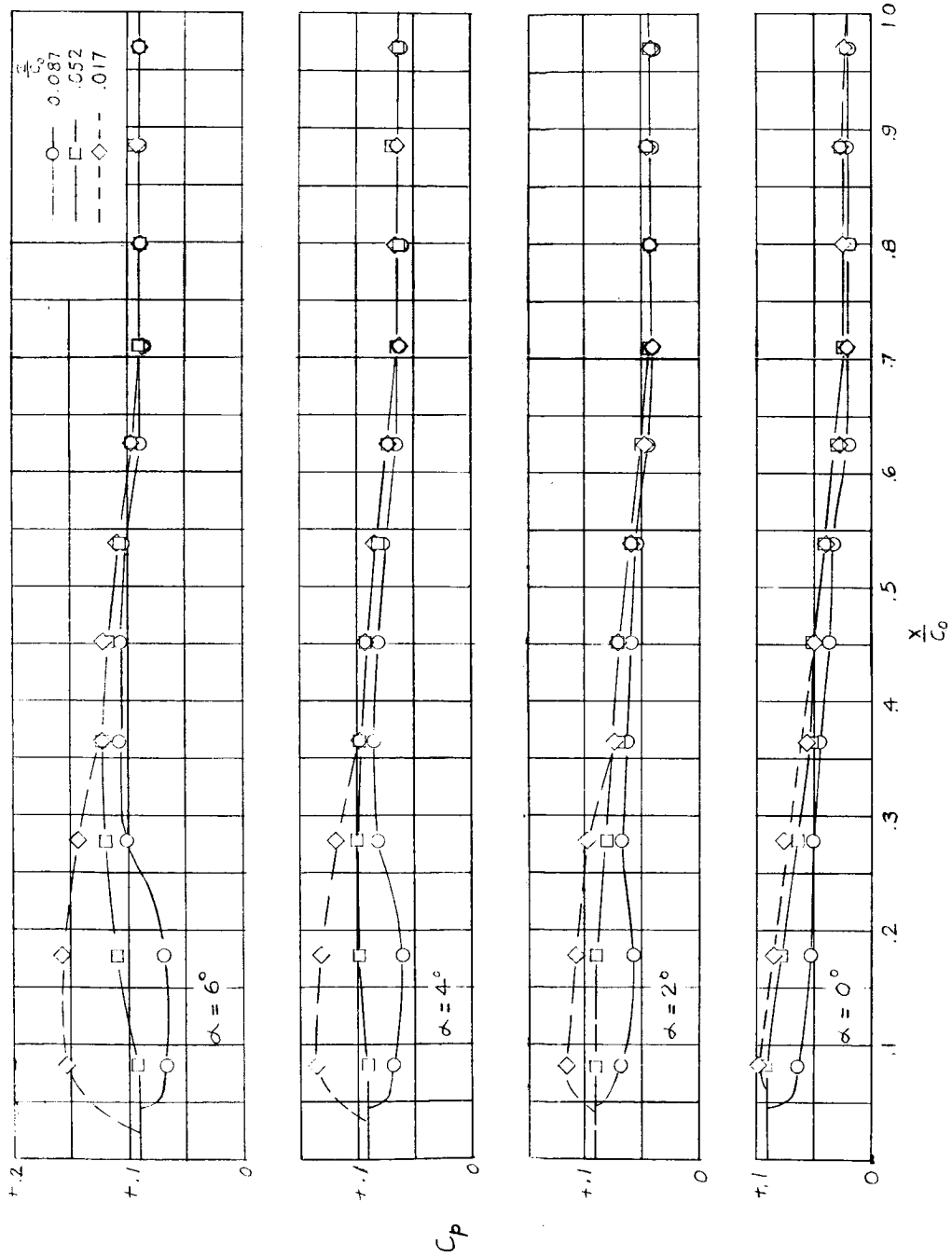
0371220 1030

CONFIDENTIAL



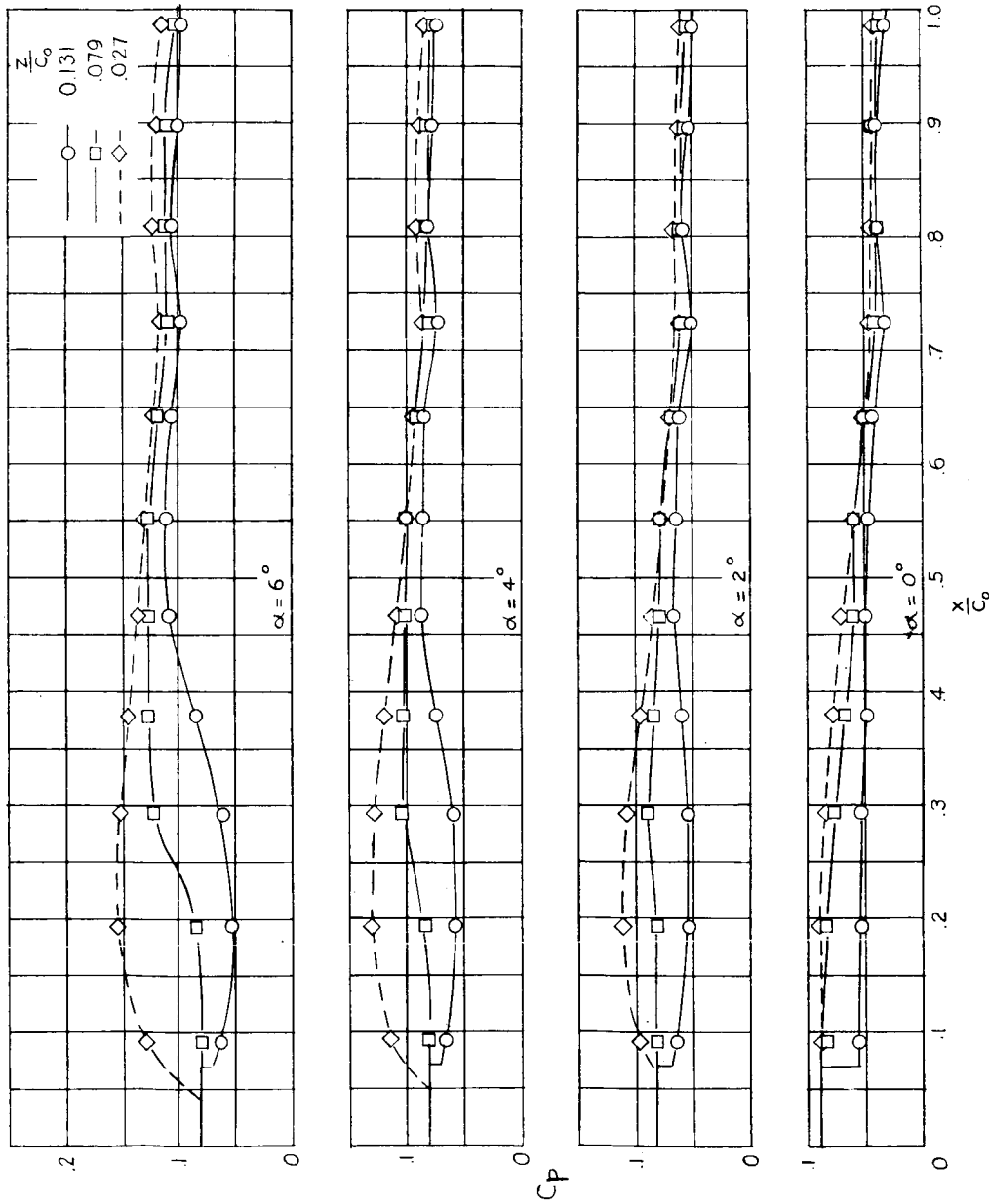
(c) Body 3.

Figure 16.- Continued.



(d) Body 4.

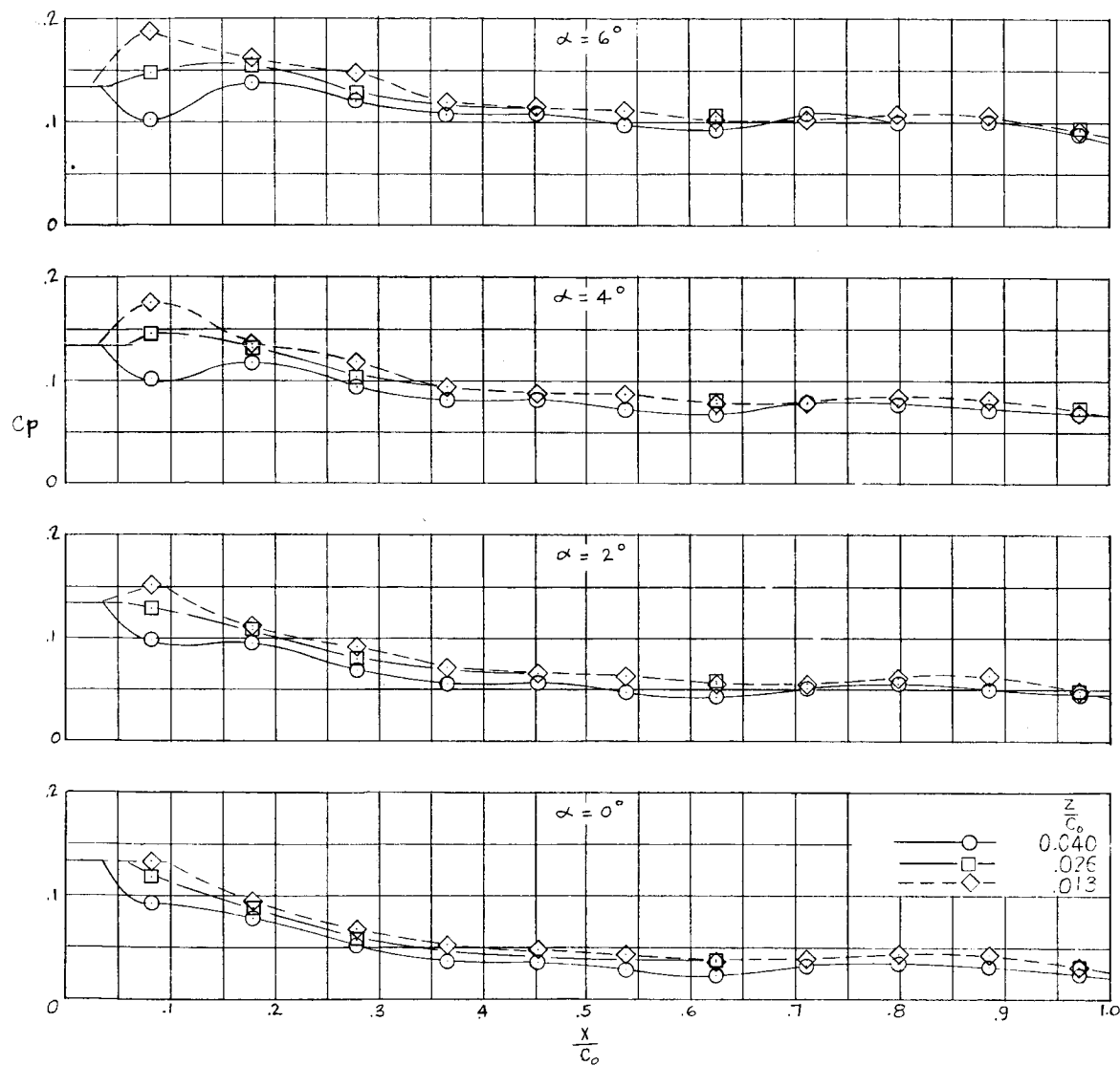
Figure 16.- Continued.



(e) Body 5.

Figure 16.- Continued.

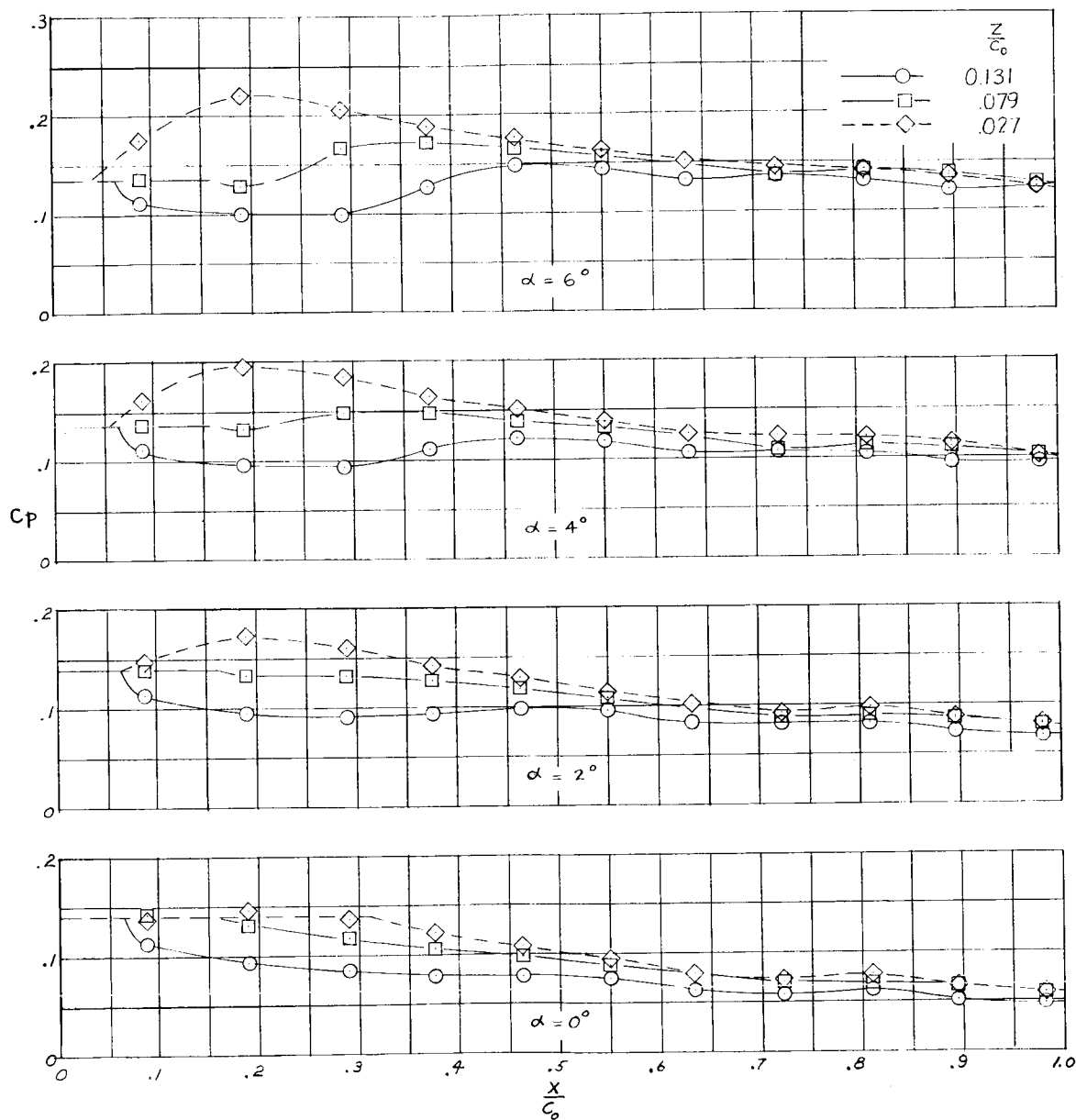
IL-254



(f) Body 6.

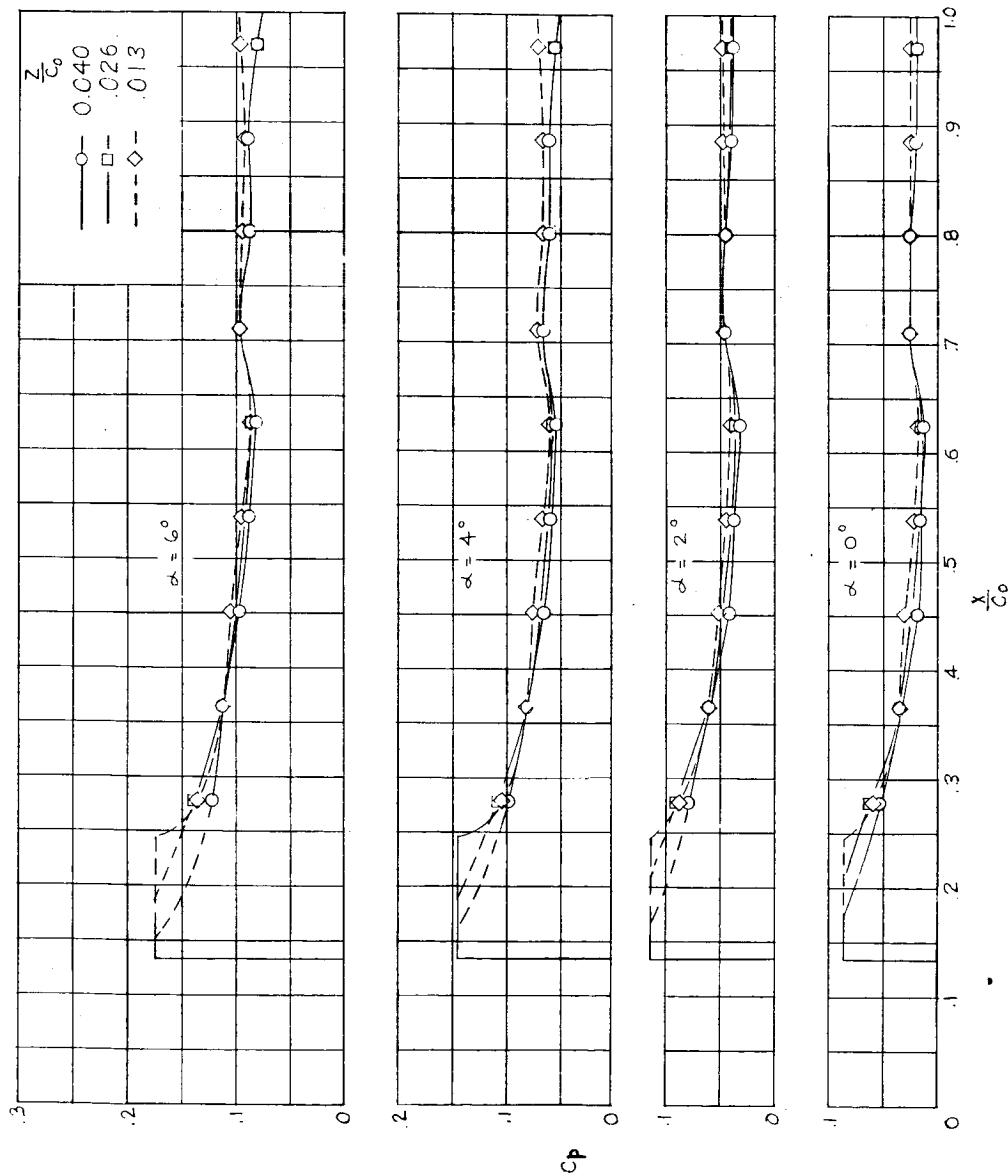
Figure 16.- Continued.

CONFIDENTIAL



(g) Body 7.

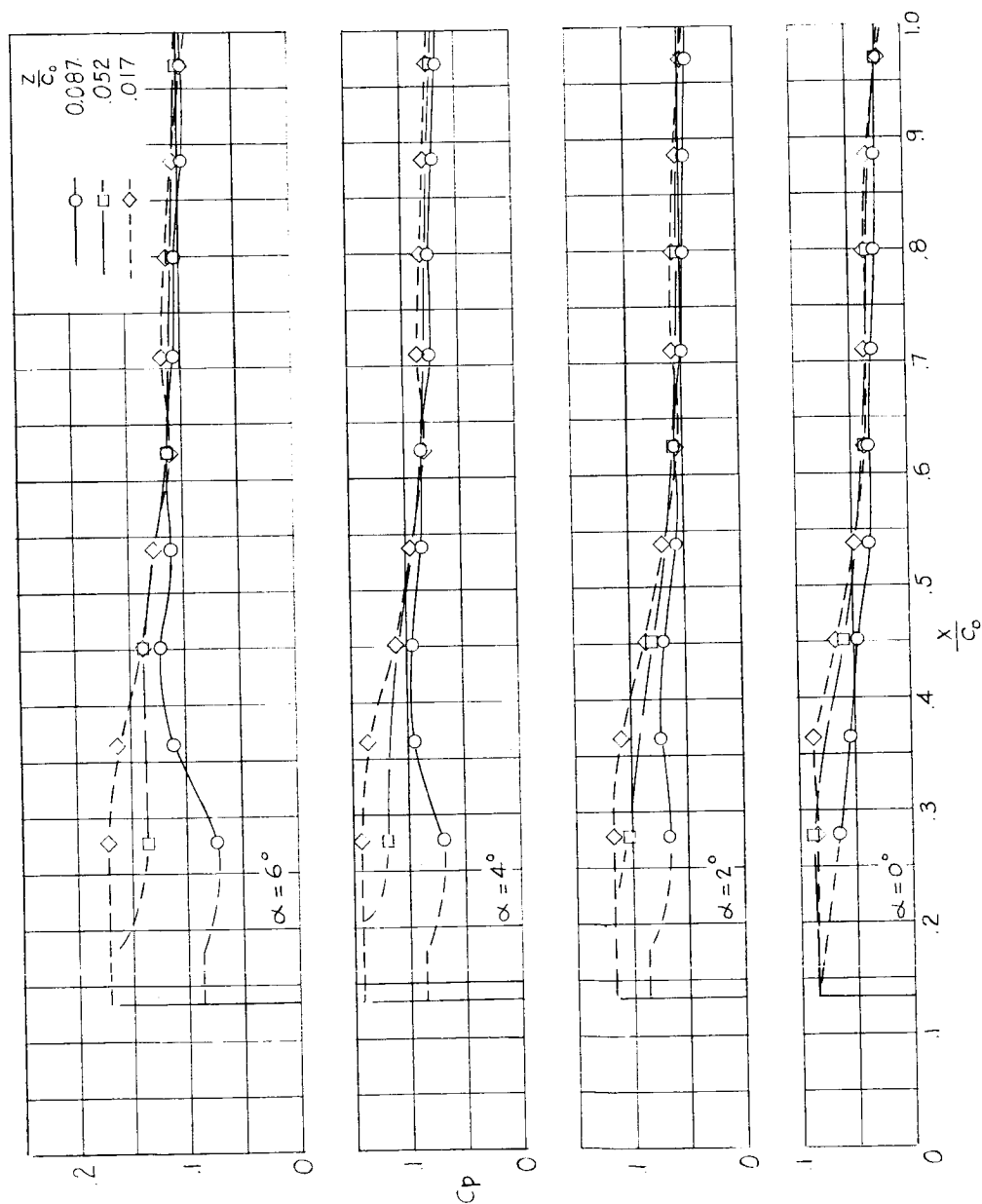
Figure 16.- Continued.



(h) Body 8.

Figure 16.- Continued.

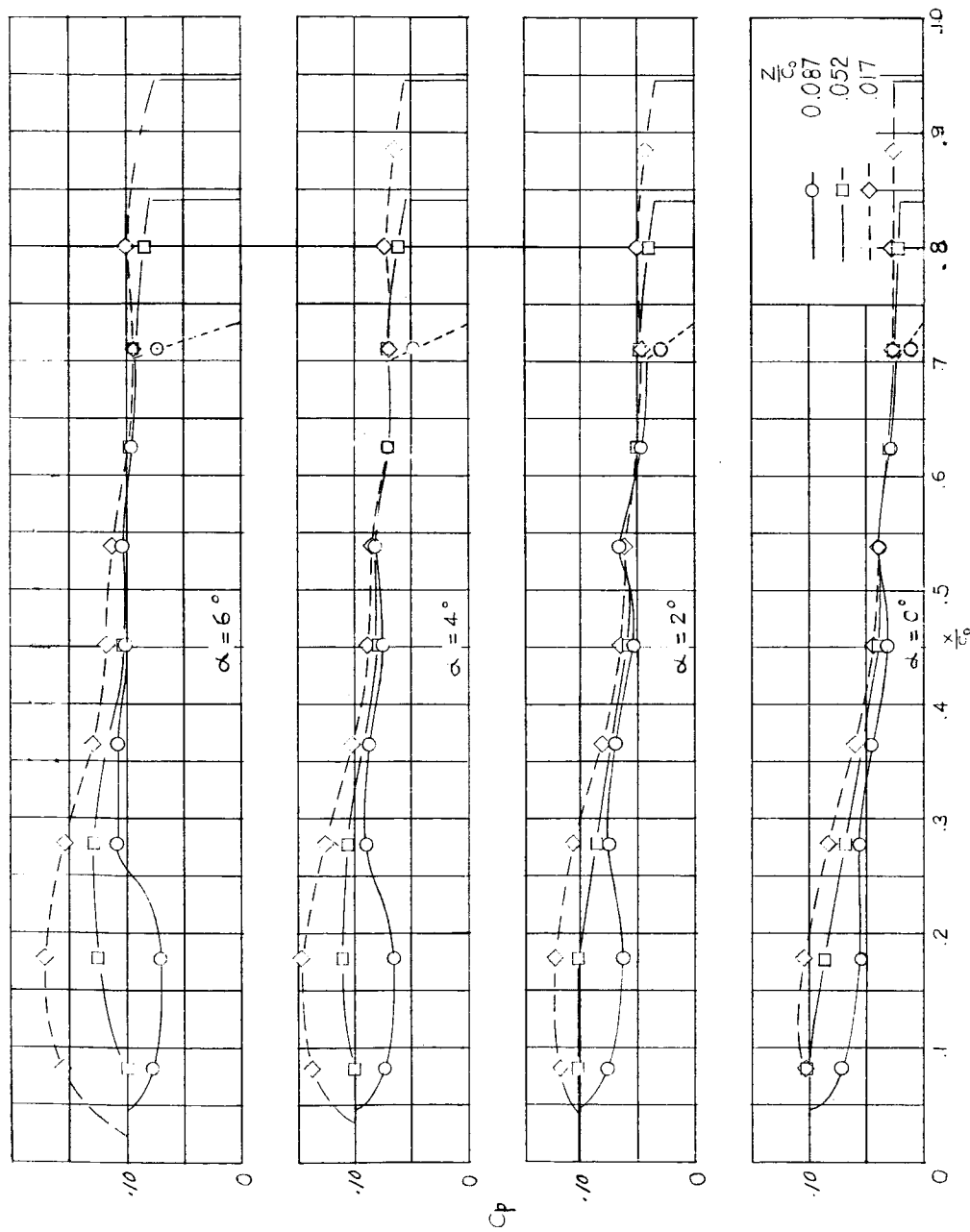
CONFIDENTIAL



(i) Body 9.

Figure 16.- Continued.

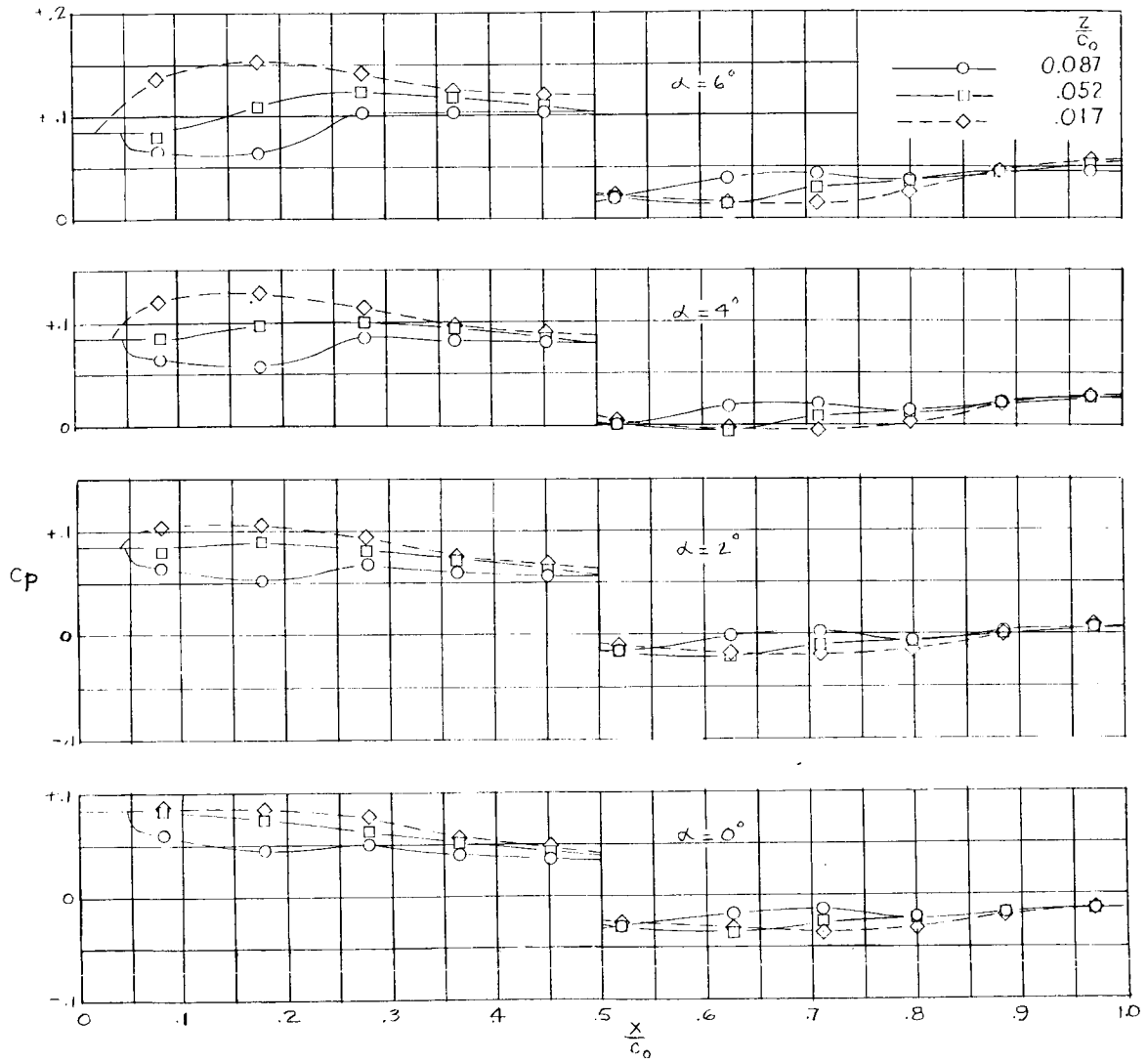
CONFIDENTIAL



(j) Body 10.

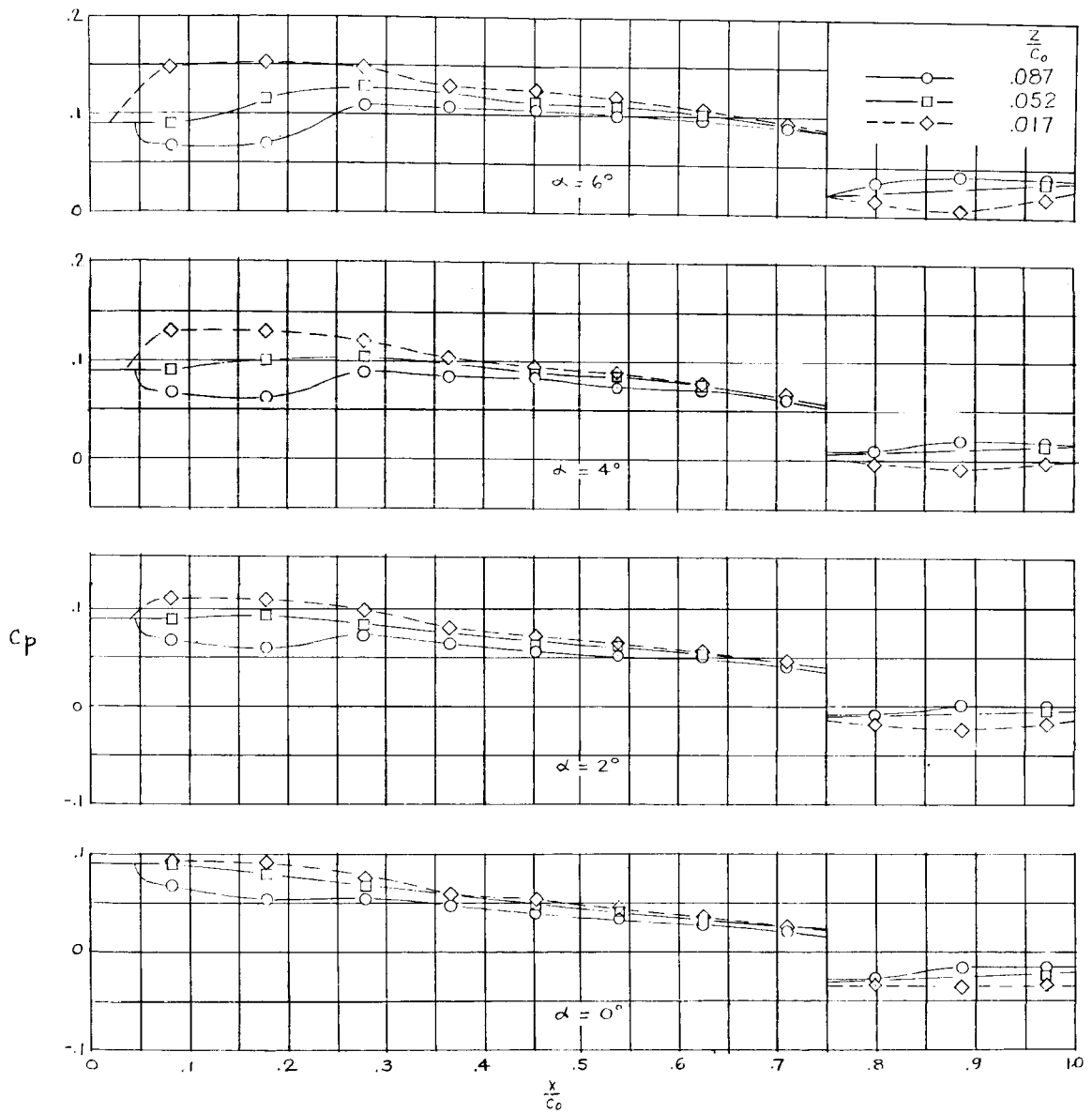
Figure 16.- Continued.

CONFIDENTIAL



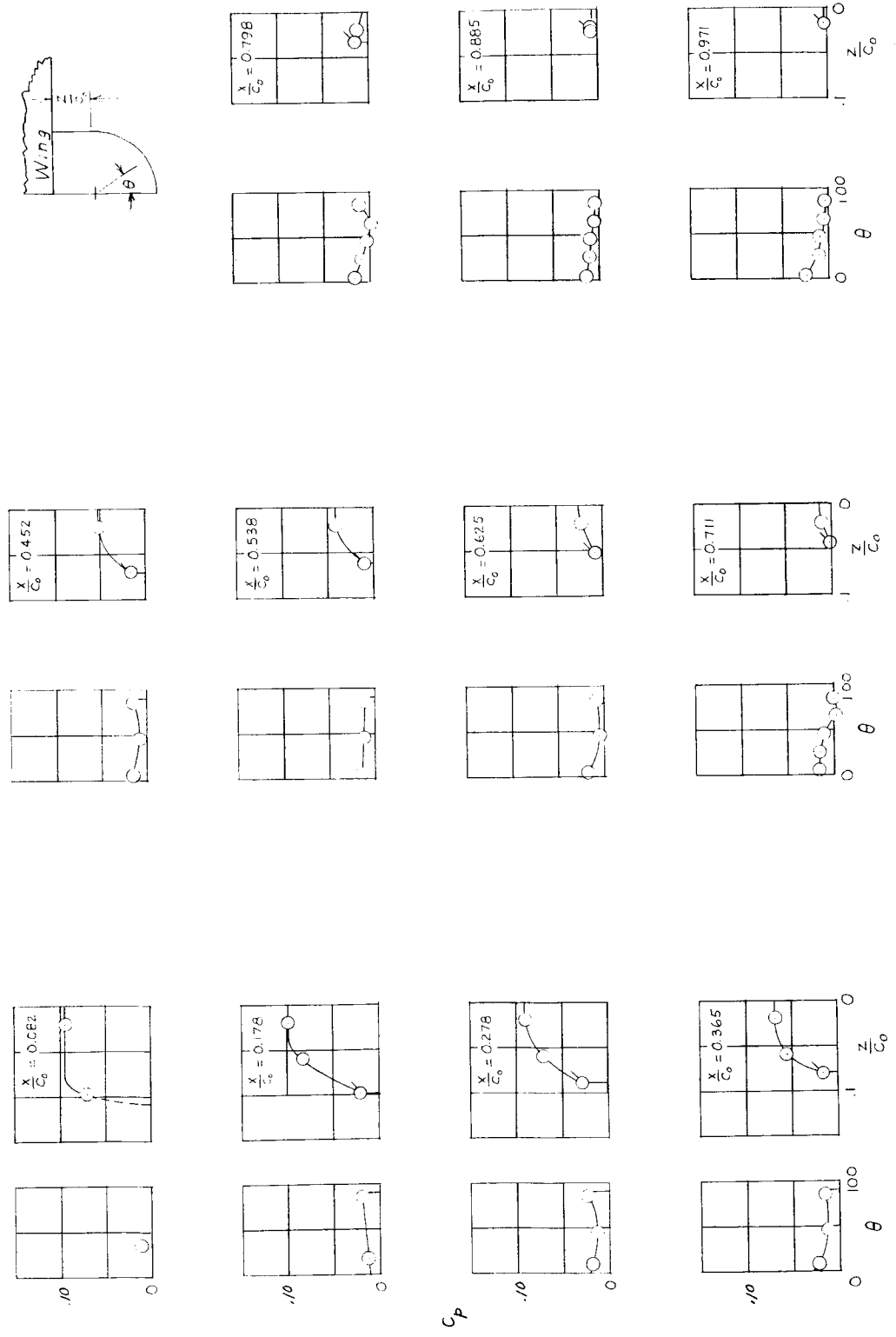
(k) Body 11.

Figure 16.- Continued.



(1) Body 12.

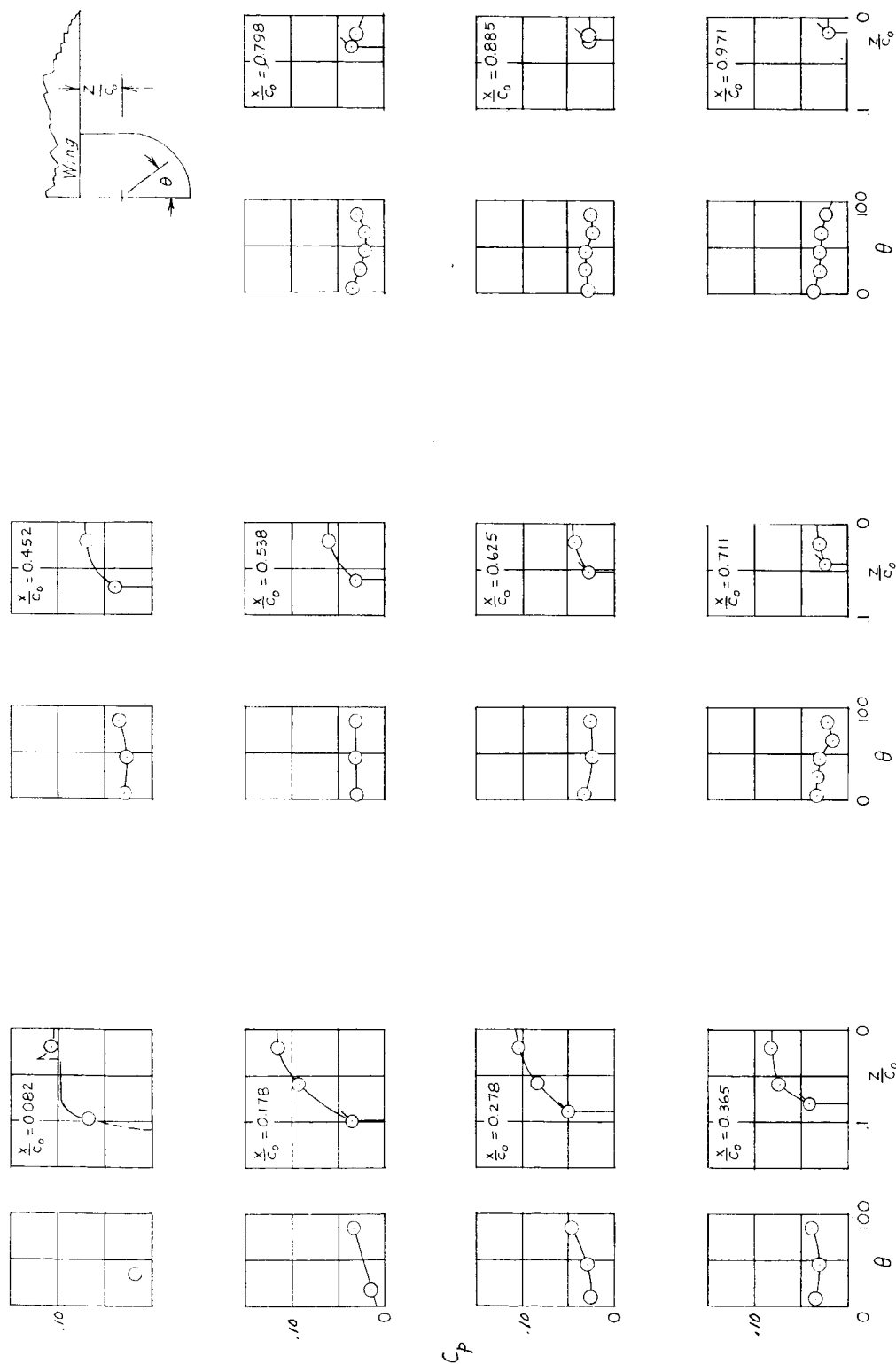
Figure 16.- Continued.



(m) Body 13; $\alpha = 0^\circ$; flagged symbols are from paired data at $\theta = 90^\circ$.

Figure 16.- Continued.

CONFIDENTIAL



(n) Body 13; $\alpha = 2^\circ$; flagged symbols are from faired data at $\theta = 90^\circ$.

Figure 16.- Continued.



CONFIDENTIAL

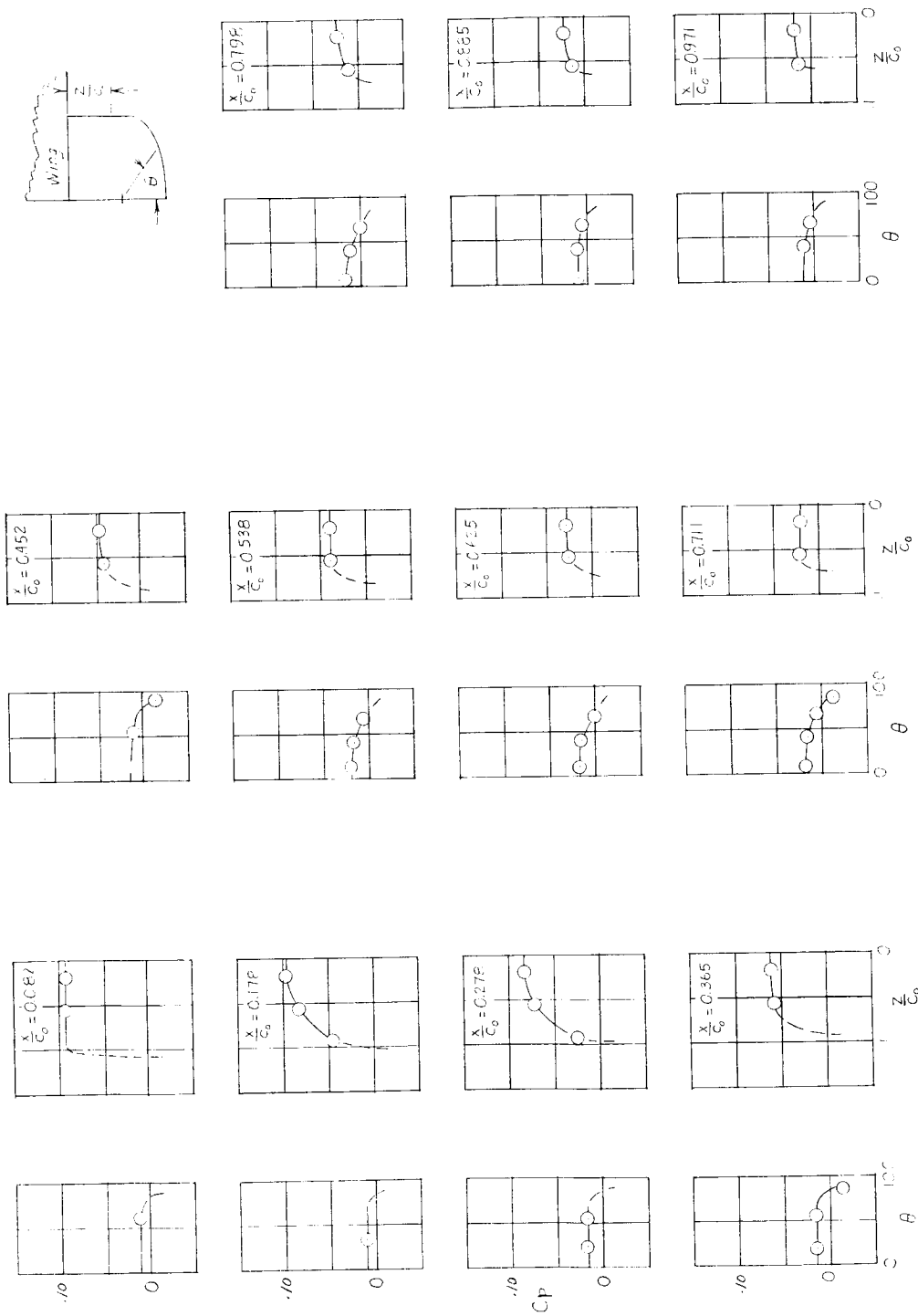
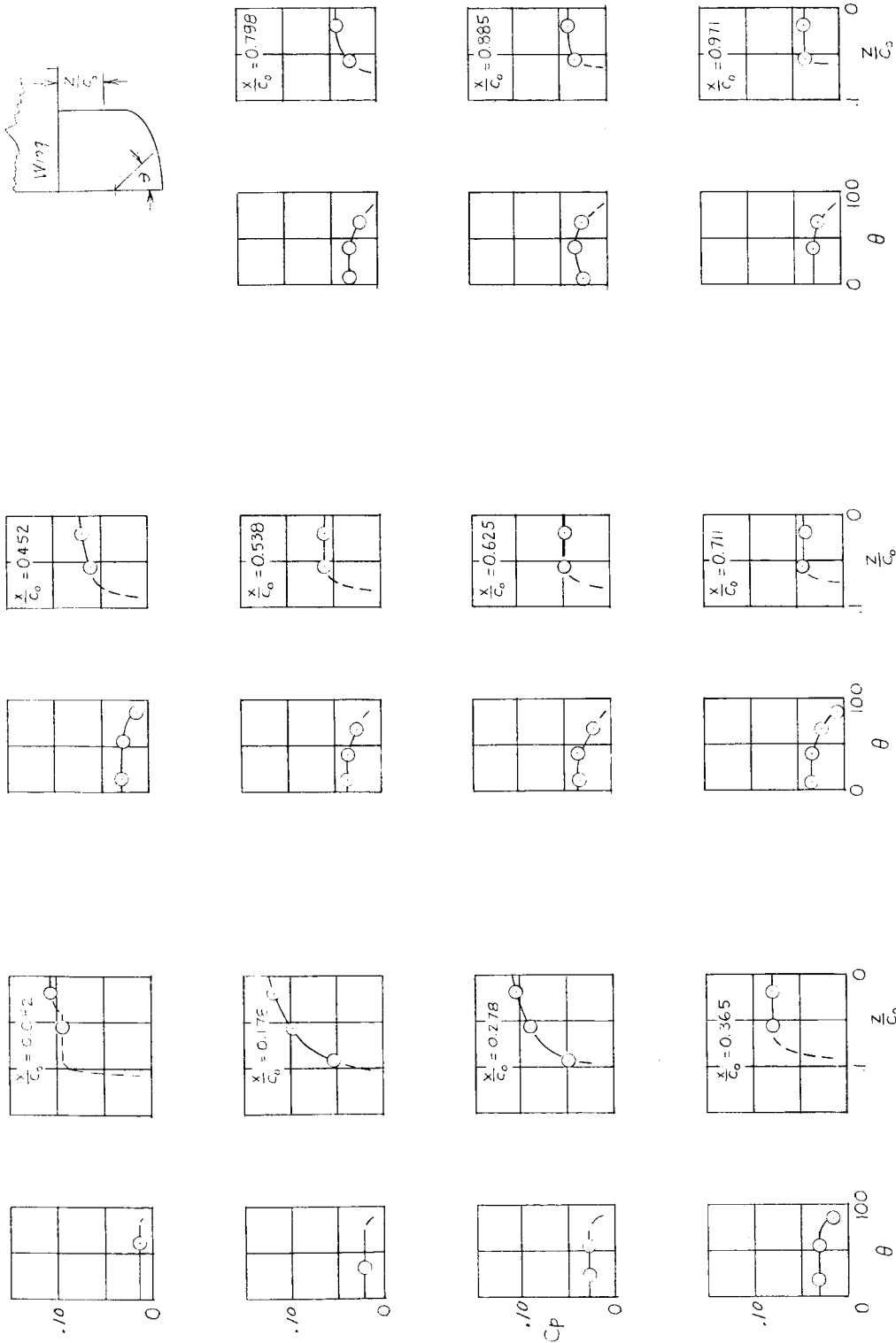
(q) Body 14; $\alpha = 0^\circ$.

Figure 16.- Continued.

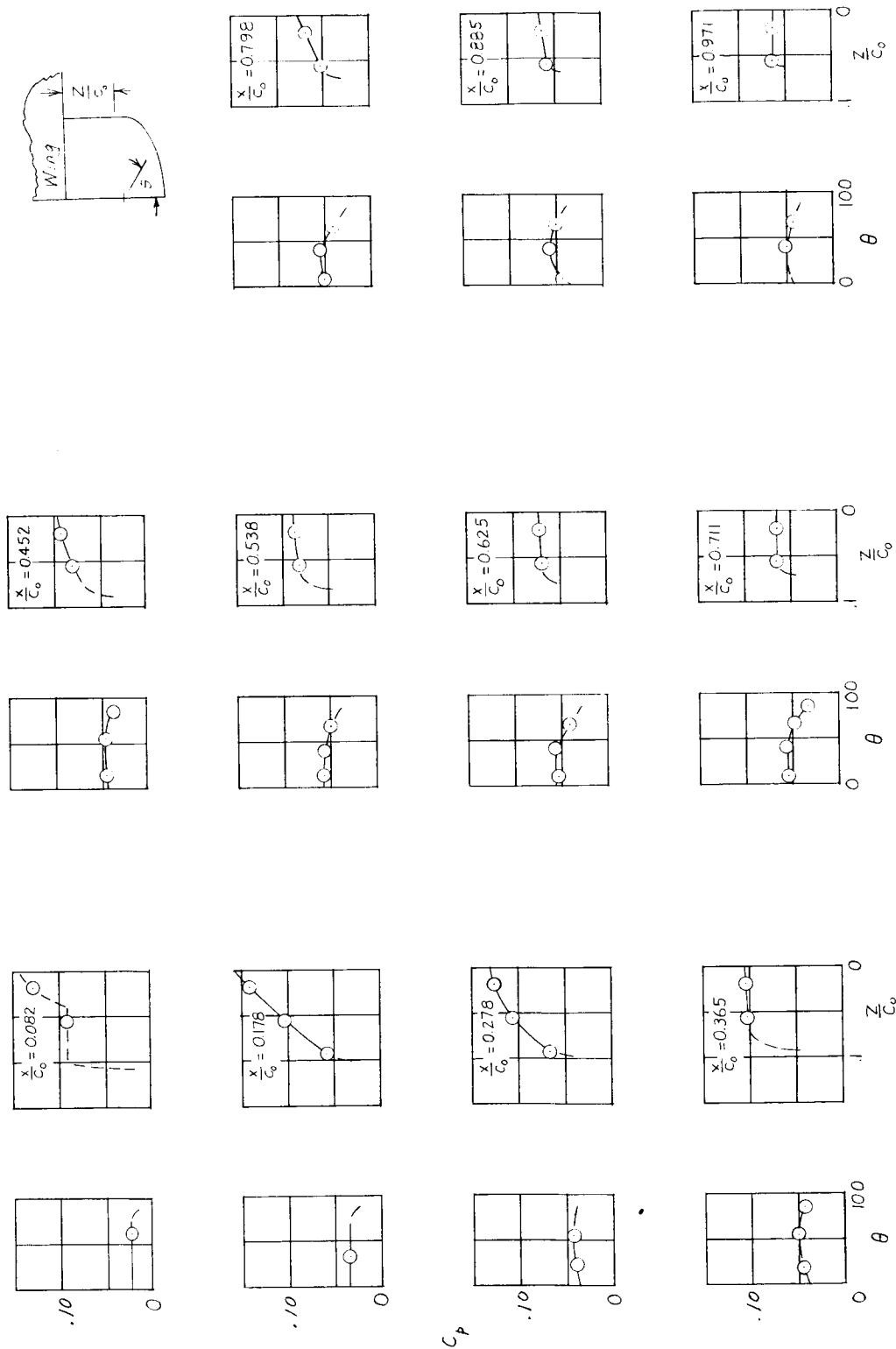
CONFIDENTIAL



(r) Body 14; $\alpha = 2^\circ$.

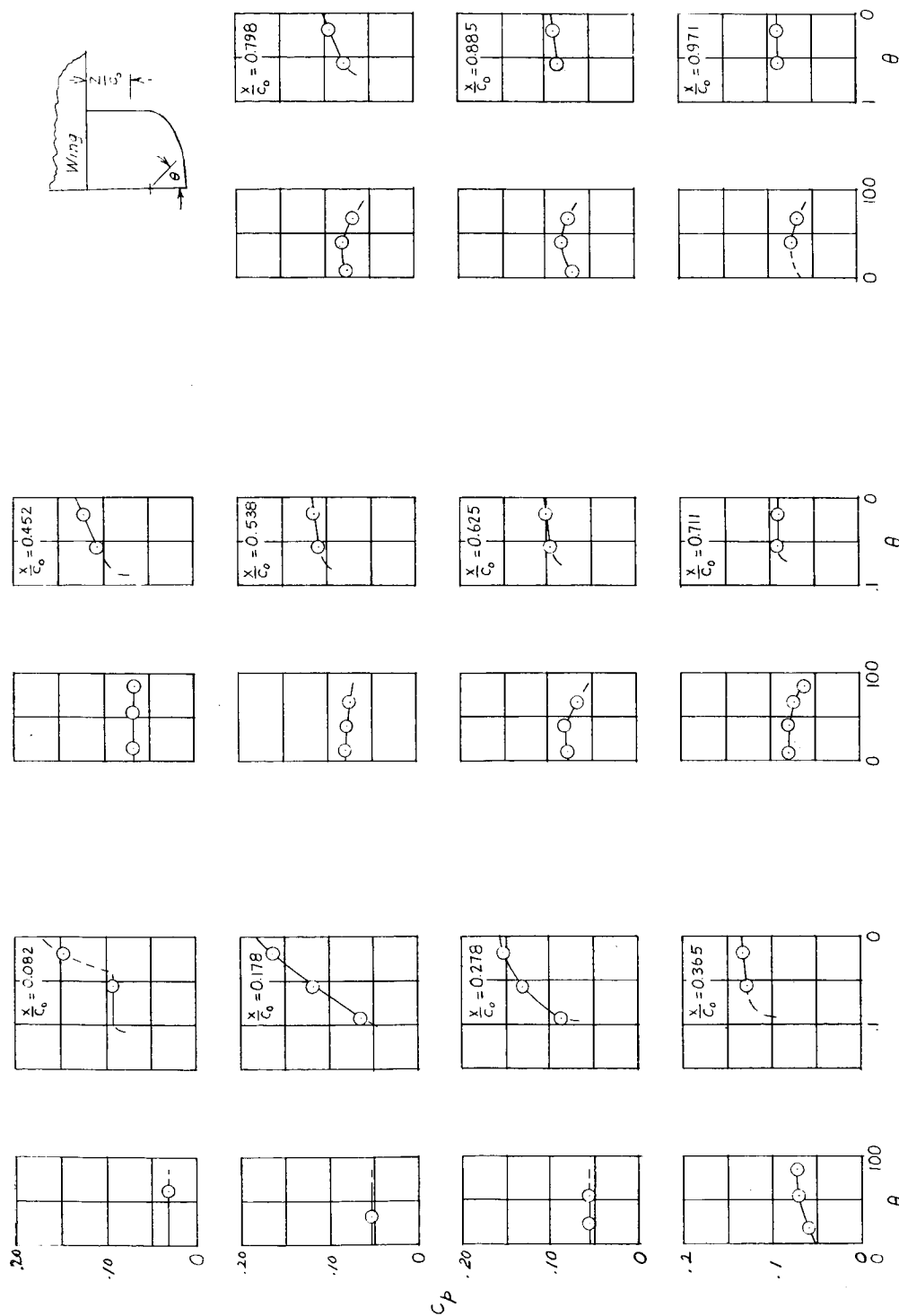
Figure 16.- Continued.

~~CONFIDENTIAL~~



(s) Body 14; $\alpha = 4^{\circ}$.

Figure 16.- Continued.



(t) Body 14; $\alpha = 6^\circ$.

Figure 16.- Concluded.

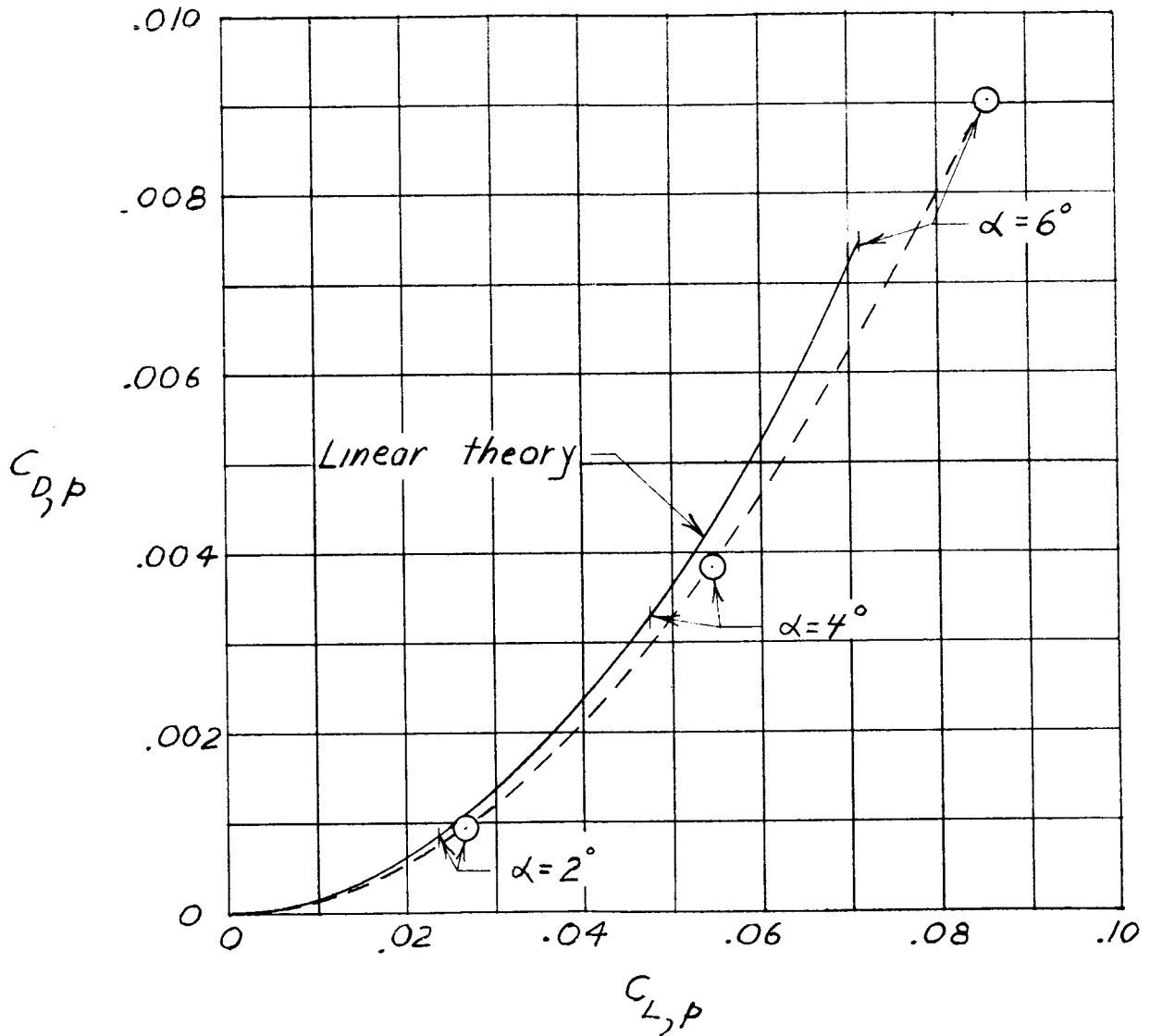


Figure 17.- Comparison of linear theory with experimental results for wing-alone configuration. Upper wing surface not considered.

CONFIDENTIAL

δ	Linear theory	Experiment
3	—————	○
6	- - - - -	□
9	—————	◇

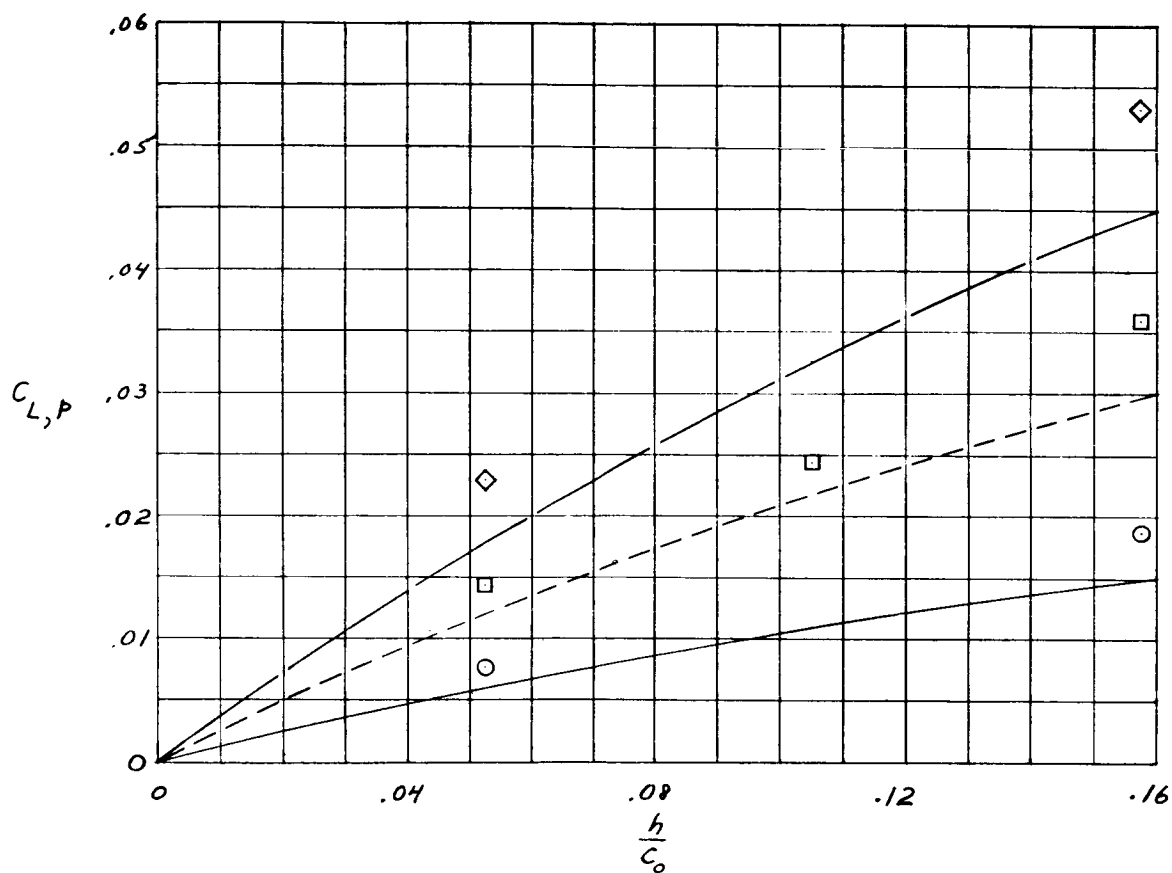
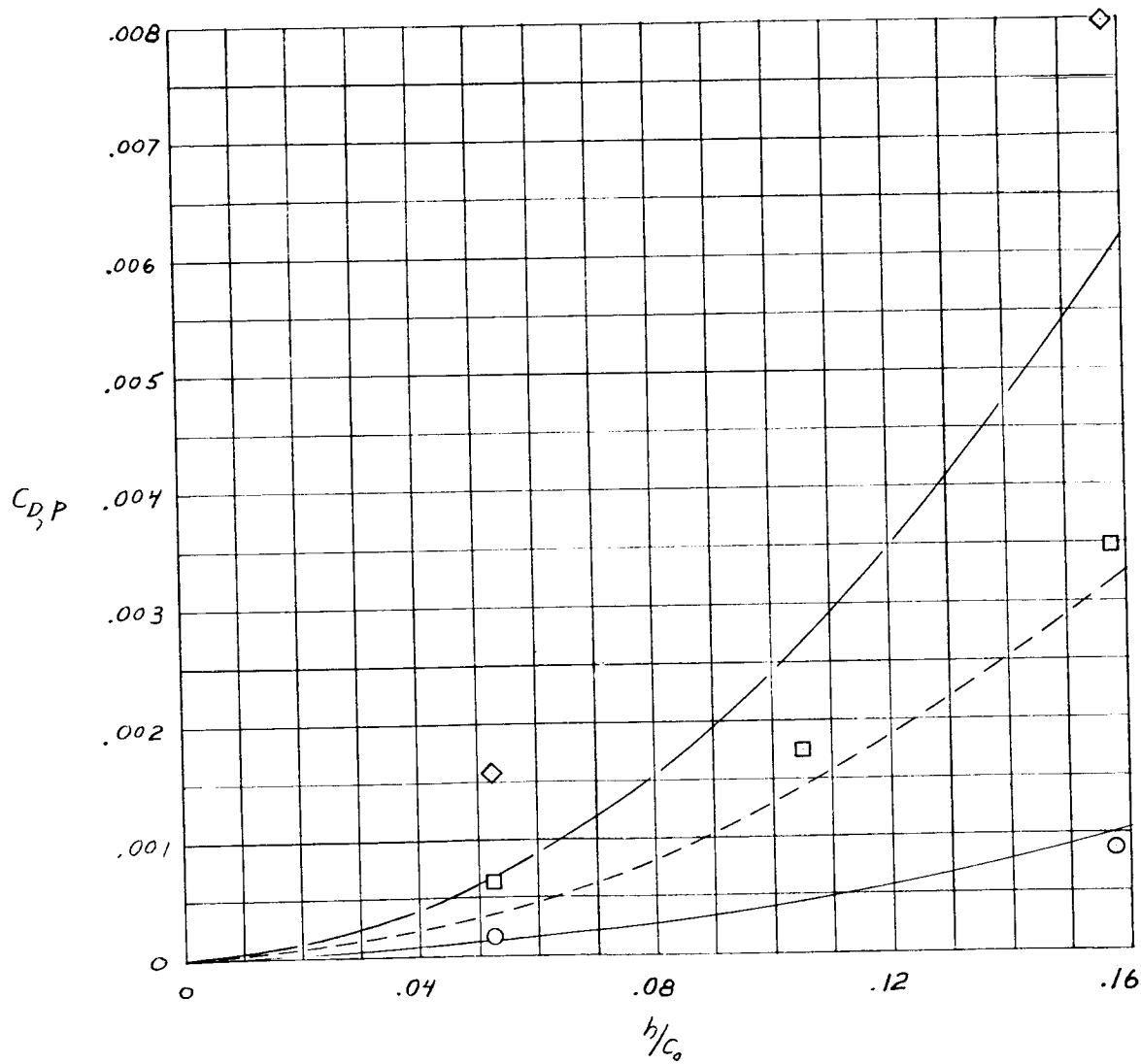
(a) $C_{L,p}$.

Figure 18.- Effect of wedge half-angle and height on experimental and theoretical variation of pressure forces at $\alpha = 0^\circ$. Upper wing surface not considered.

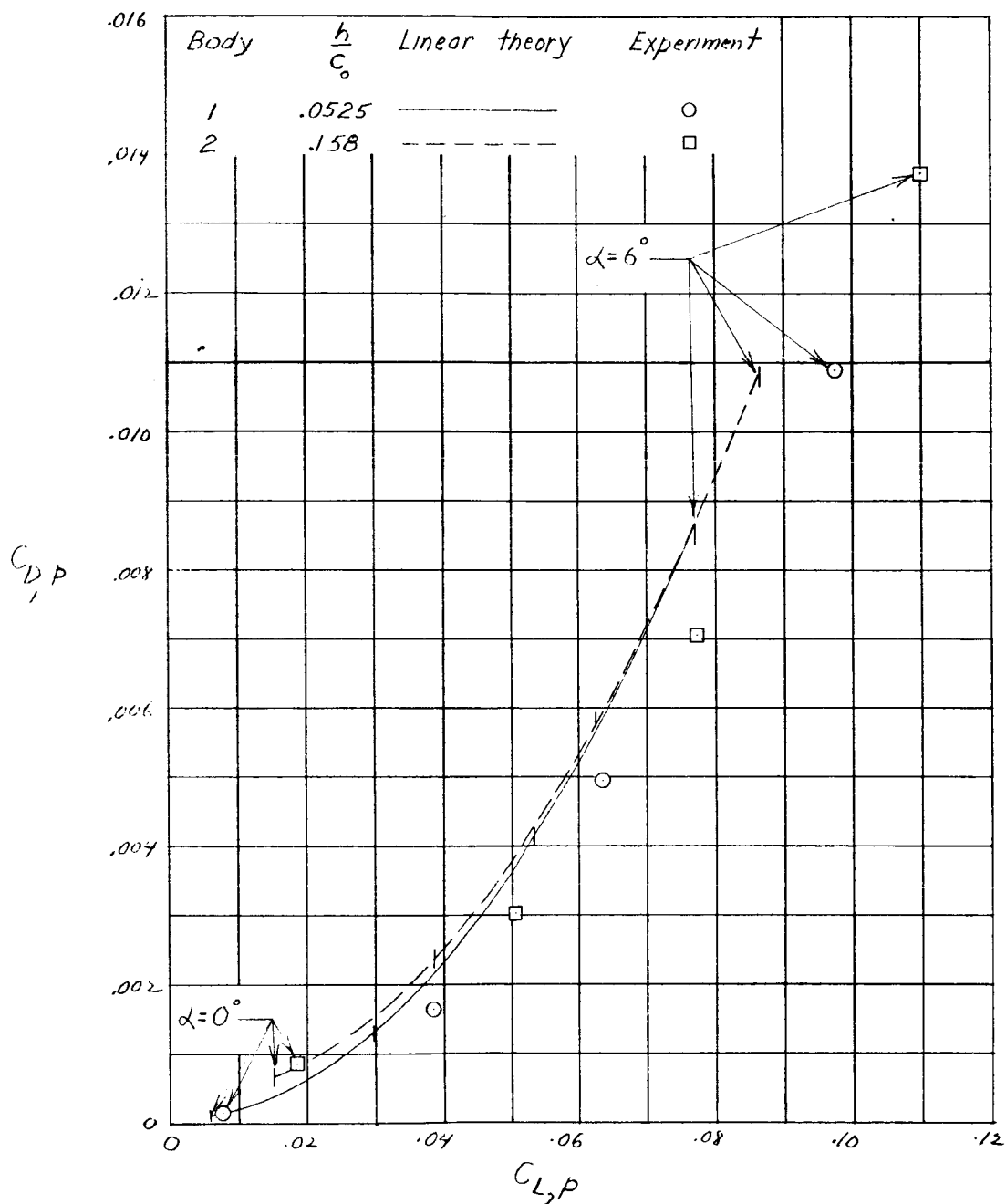
CONFIDENTIAL

δ	Linear theory	Experiment
3	—————	○
6	- - - - -	□
9	—————	◇



(b) $C_{D,p}$.

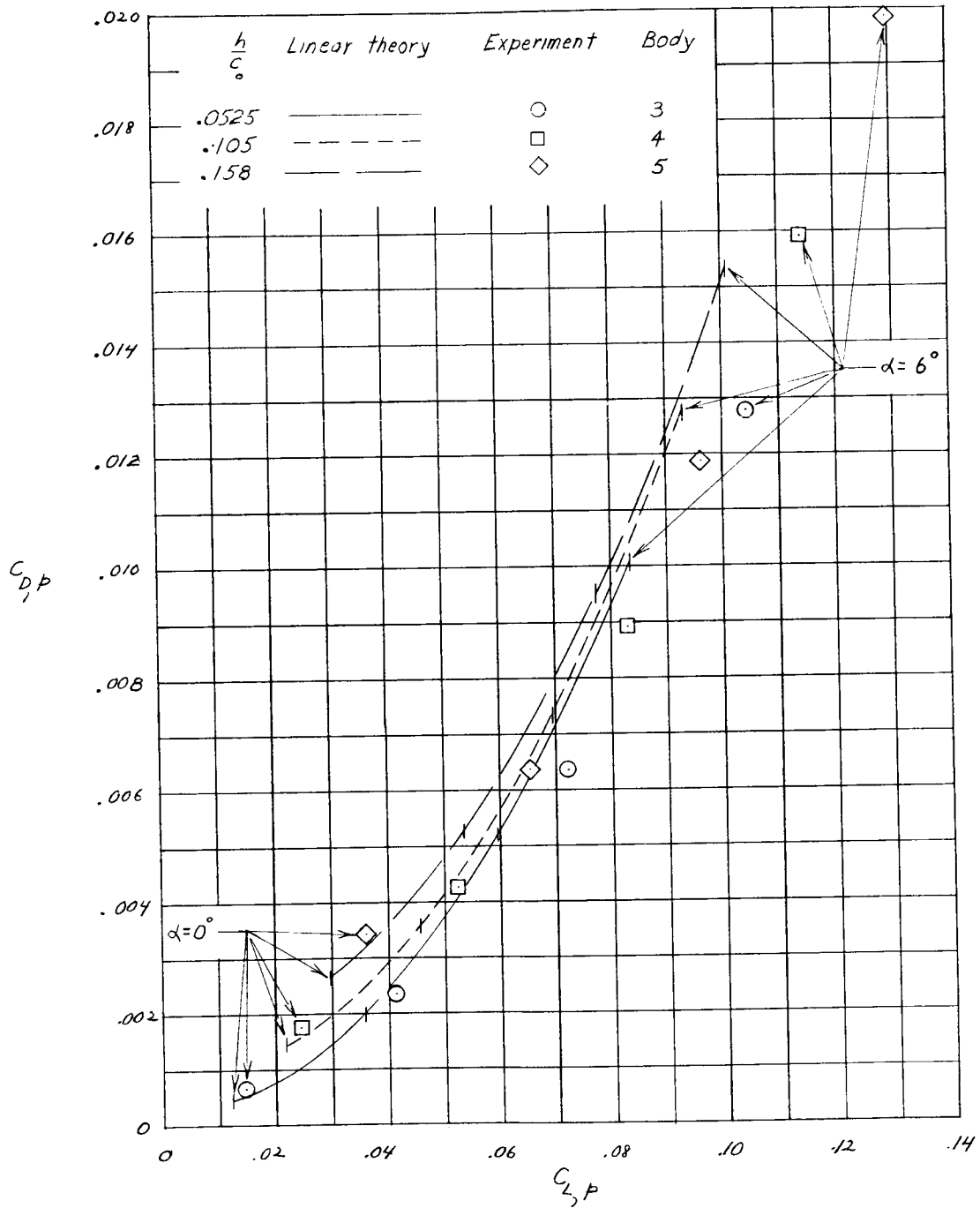
Figure 18.- Concluded.



(a) $\delta = 3^\circ$.

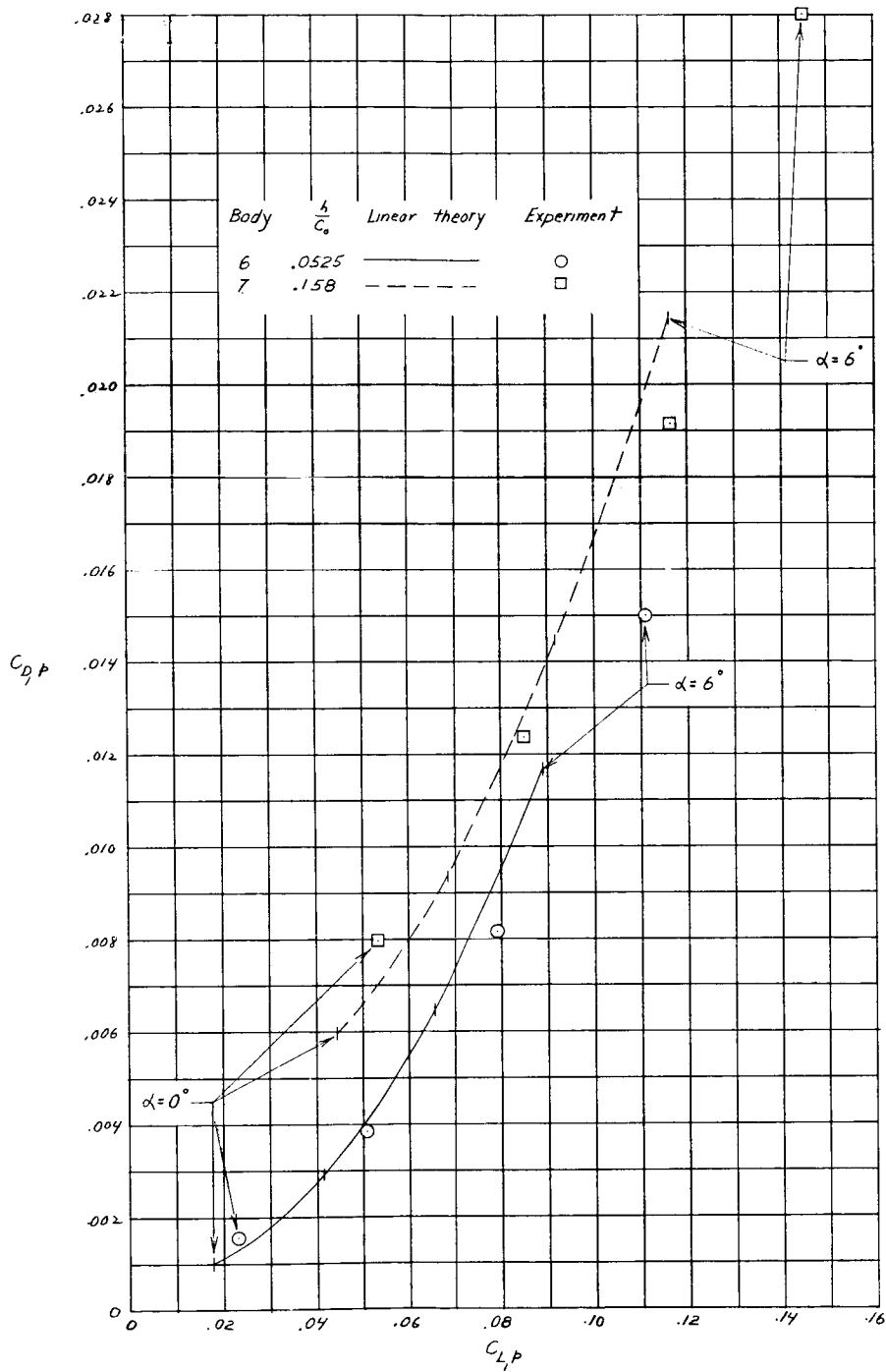
Figure 19.- Comparison of linear theory and experimental results for wing-body configurations. Upper wing surface not considered.

CONFIDENTIAL



(b) $\delta = 6^\circ$.

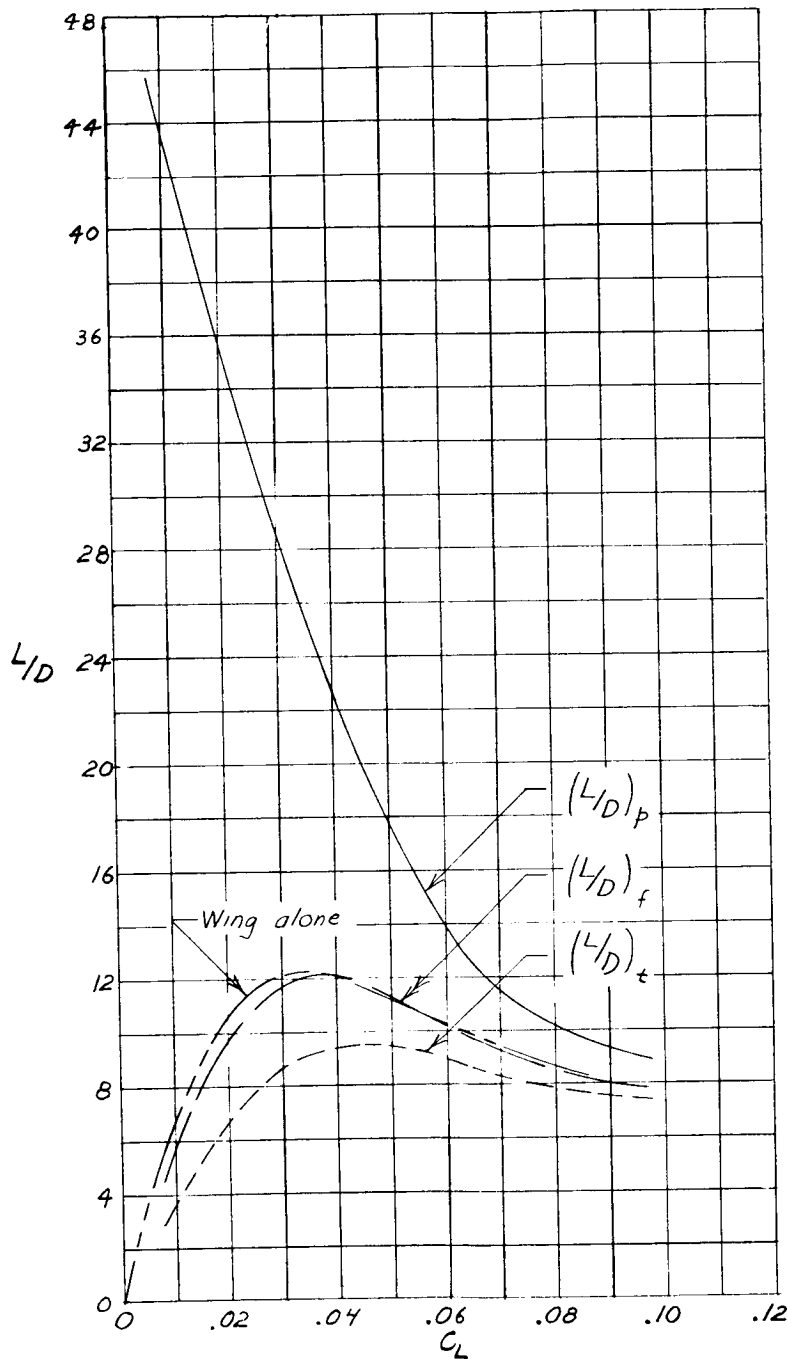
Figure 19.- Continued.



(c) $\delta = 9^\circ$.

Figure 19.- Concluded.

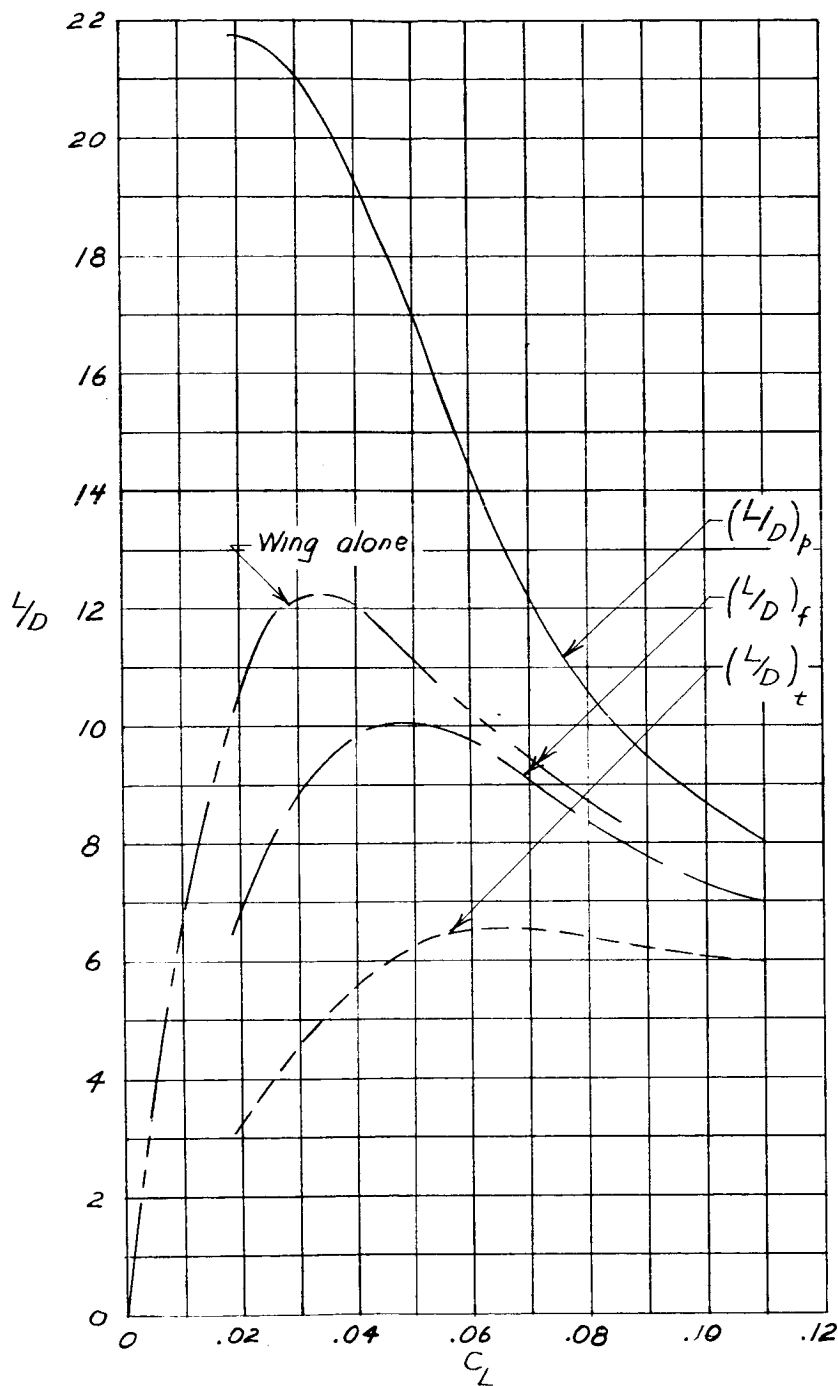
CONFIDENTIAL



(a) Body 1.

Figure 20.- Lift-drag characteristics of wing-alone and wing-body configurations. $C_f = 0.0013$. Upper wing surface not considered.

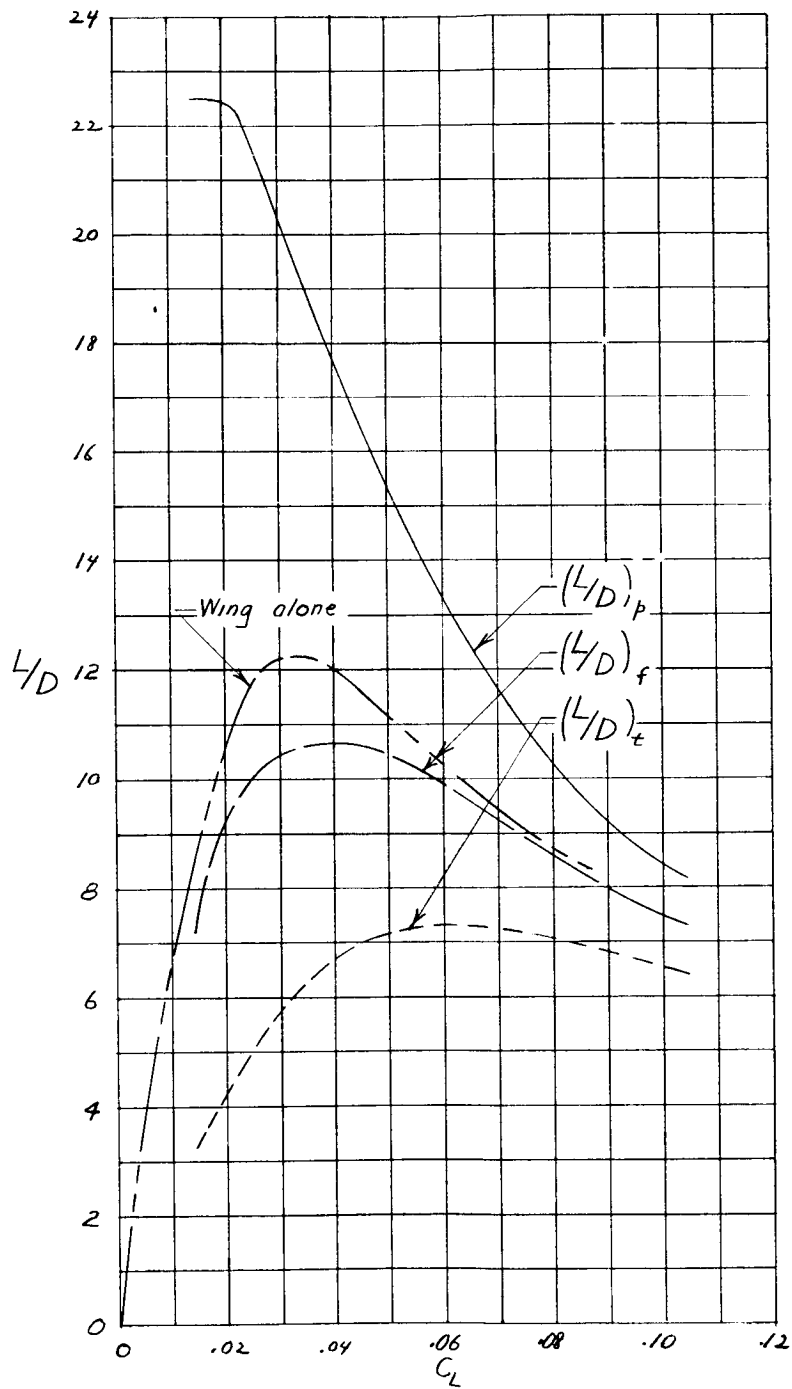




(b) Body 2.

Figure 20.- Continued.

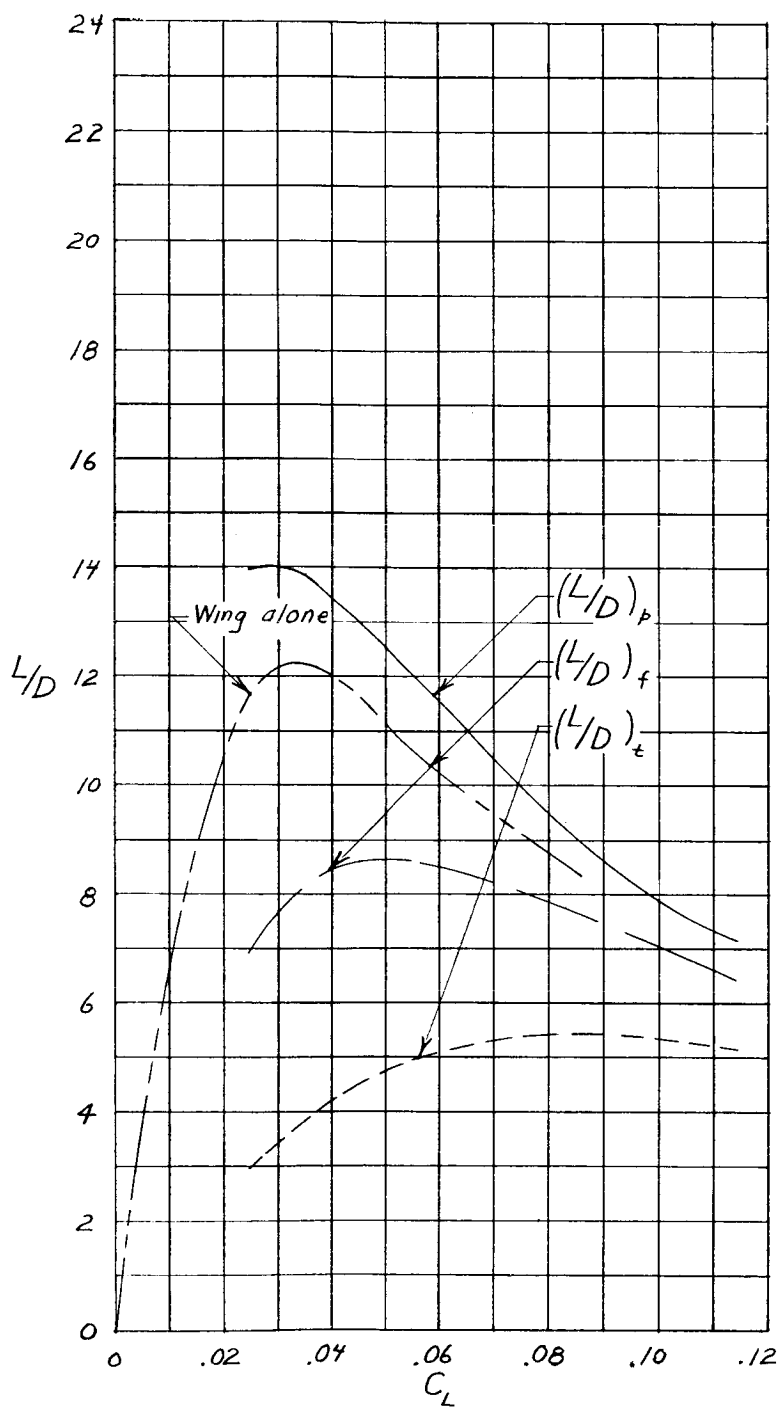
CONFIDENTIAL



(c) Body 3.

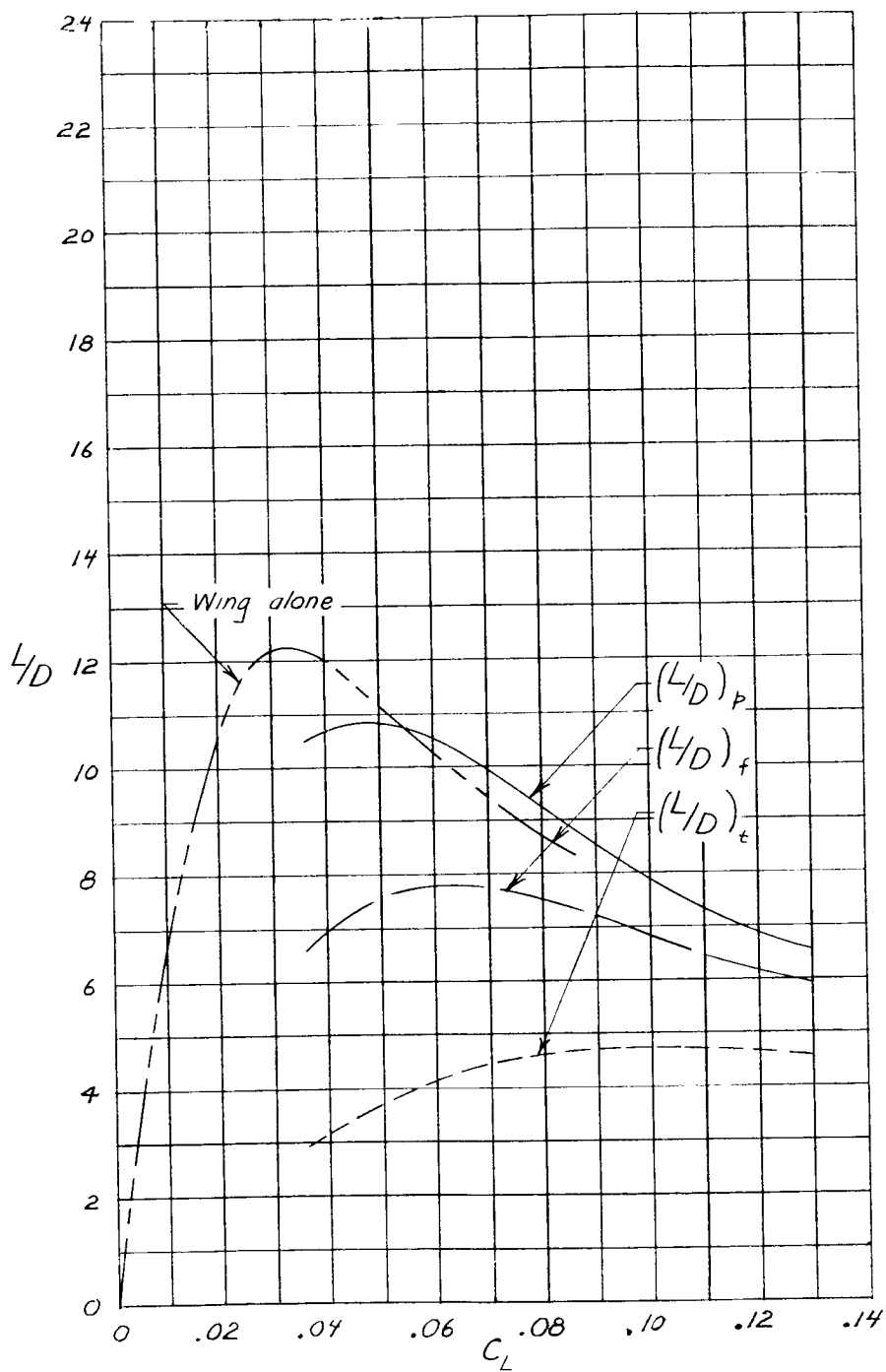
Figure 20.- Continued.

CONFIDENTIAL



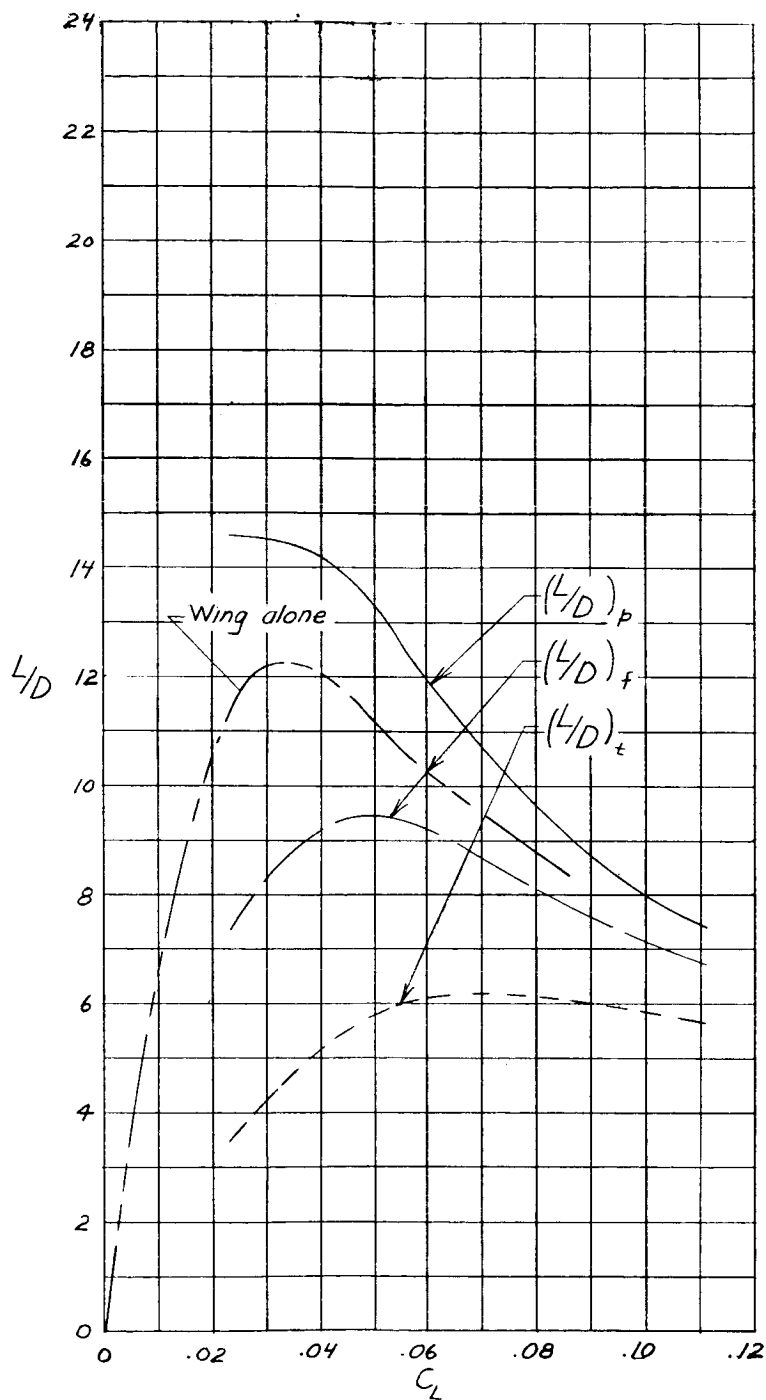
(d) Body 4.

Figure 20.- Continued.

03:17:28.030
CONFIDENTIAL

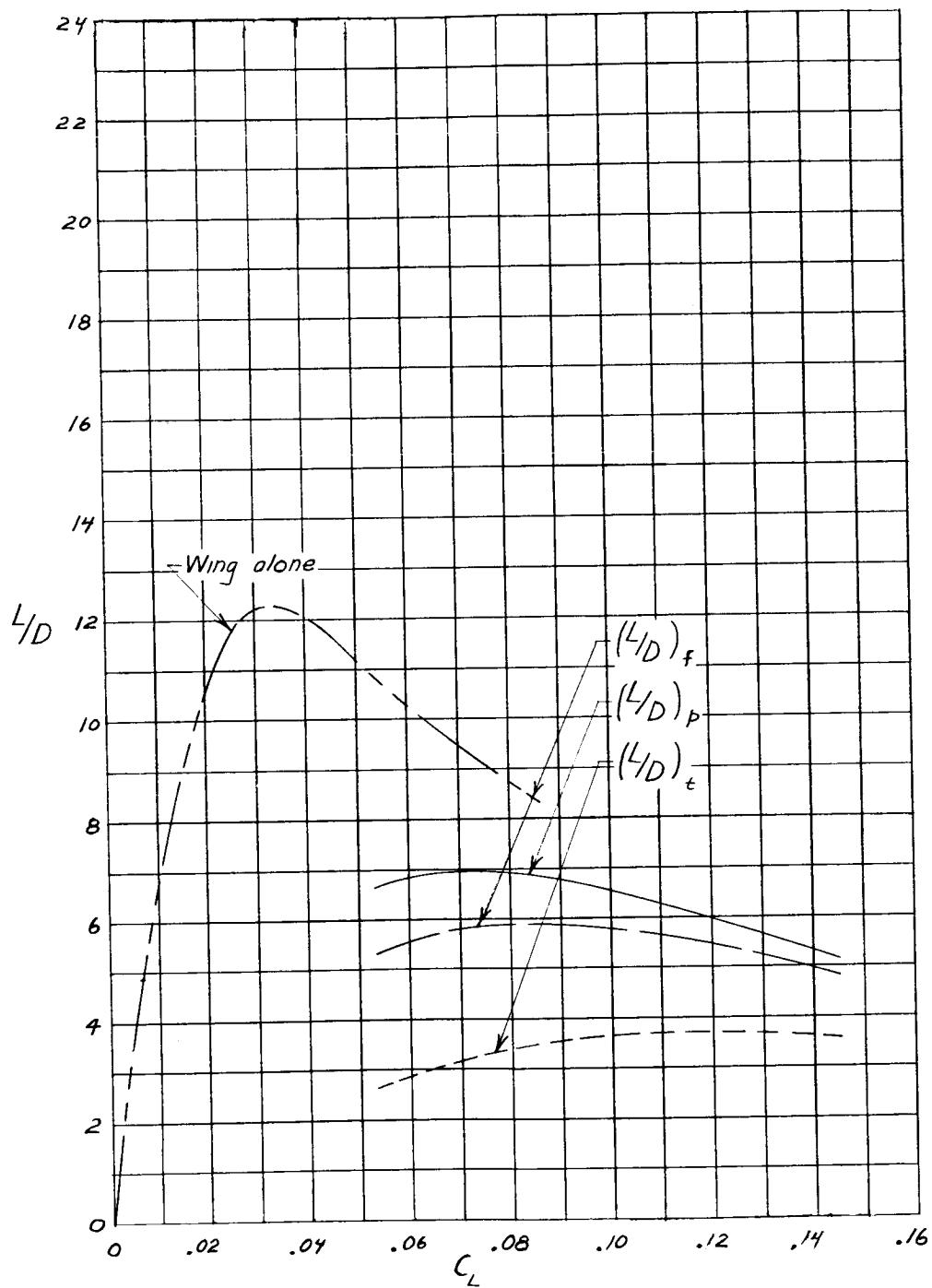
(e) Body 5.

Figure 20.- Continued.



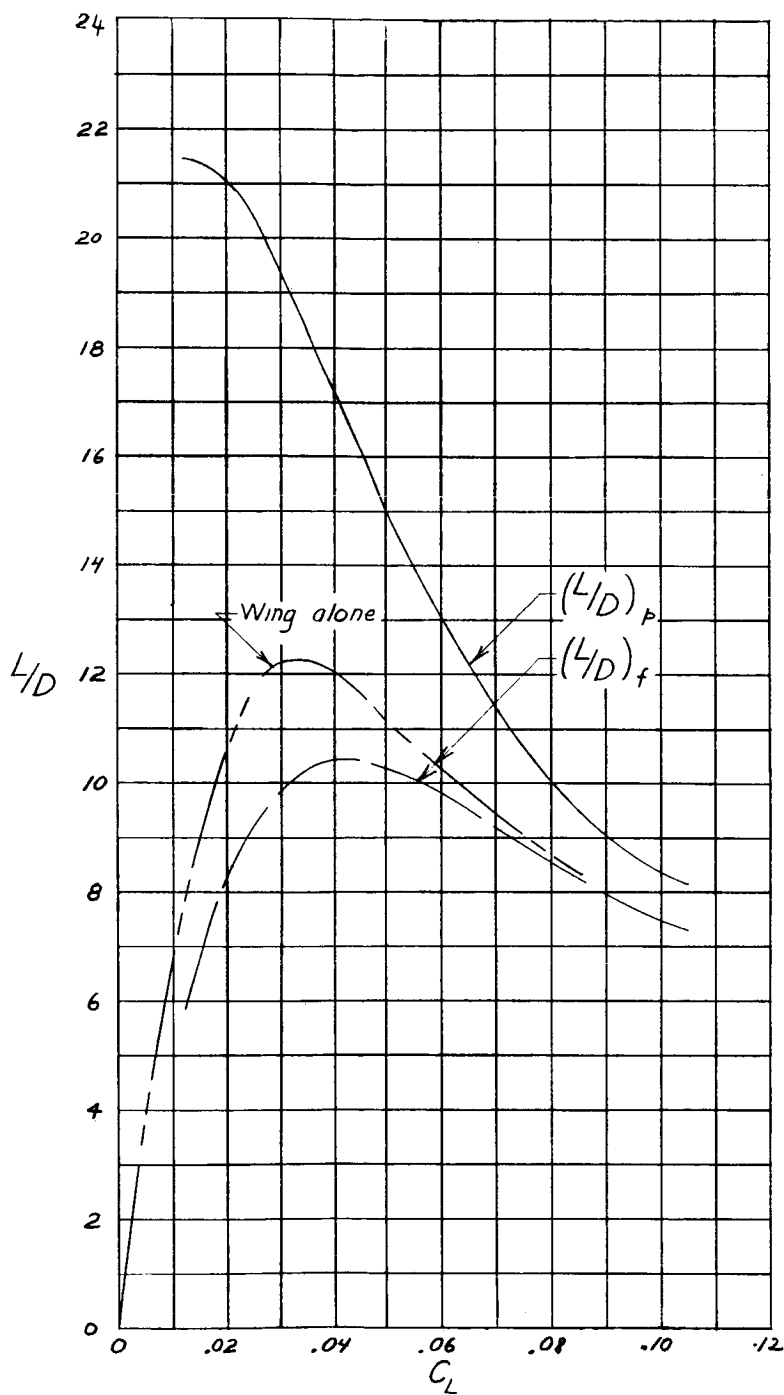
(f) Body 6.

Figure 20.- Continued.

03710291030
CONFIDENTIAL

(g) Body 7.

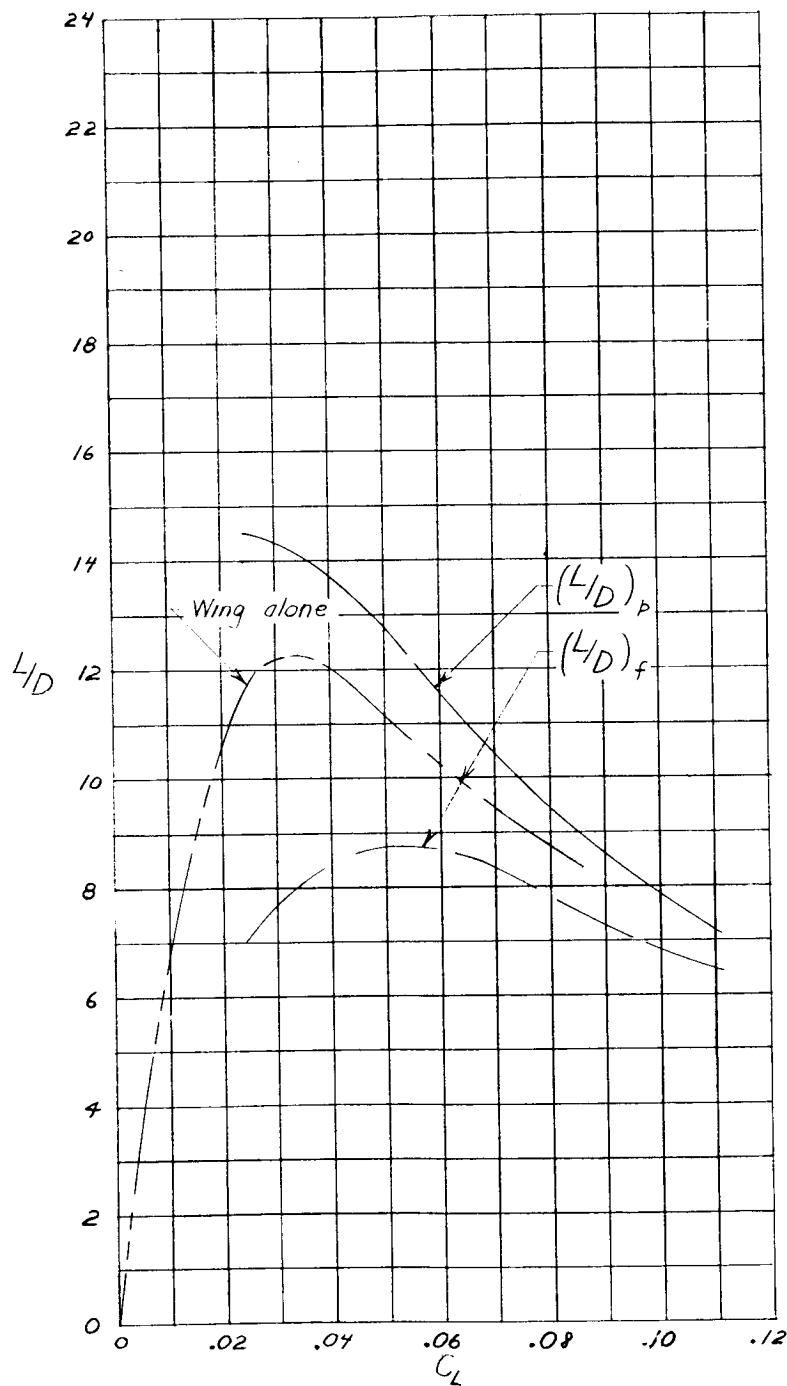
Figure 20.- Continued.



(h) Body 8.

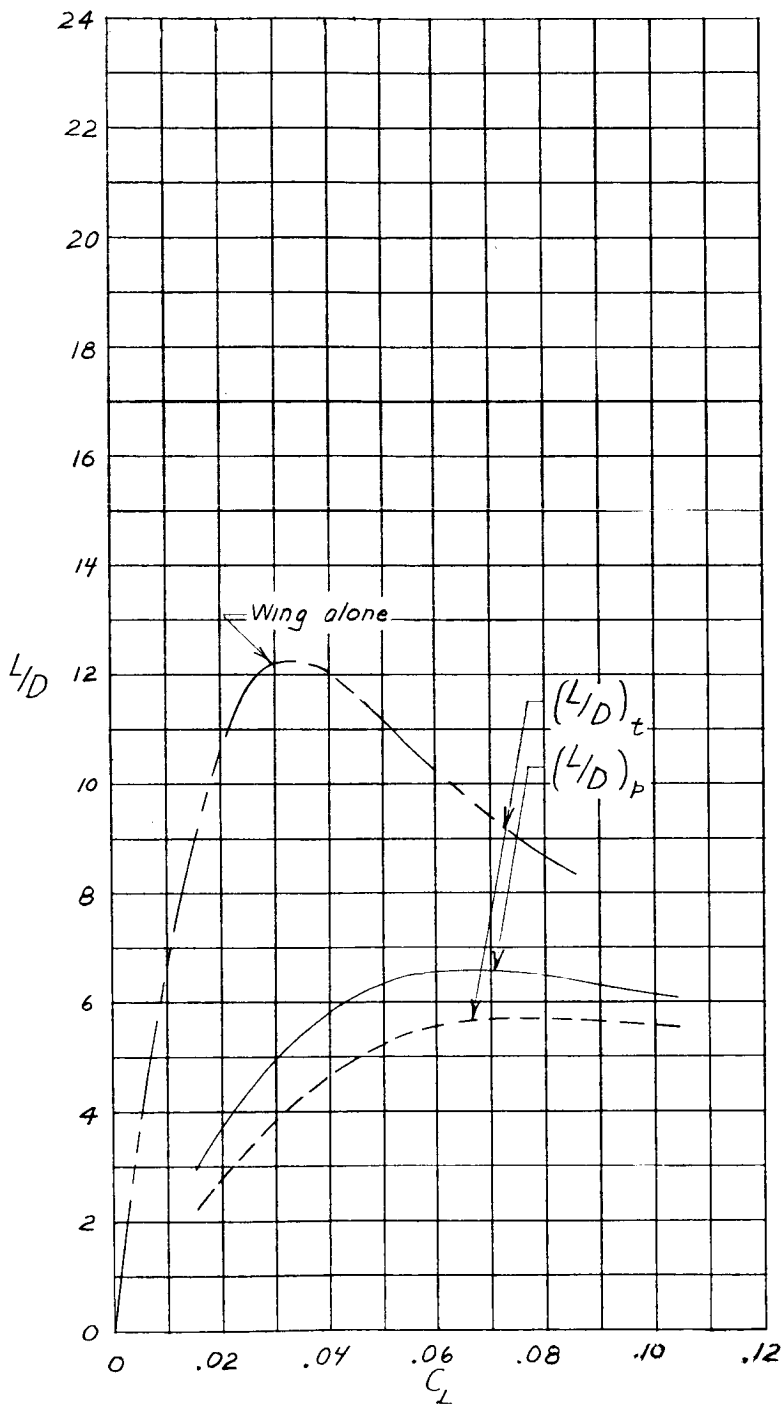
Figure 20.- Continued.

03:713:28:1030
CONFIDENTIAL



(i) Body 9.

Figure 20.- Continued.

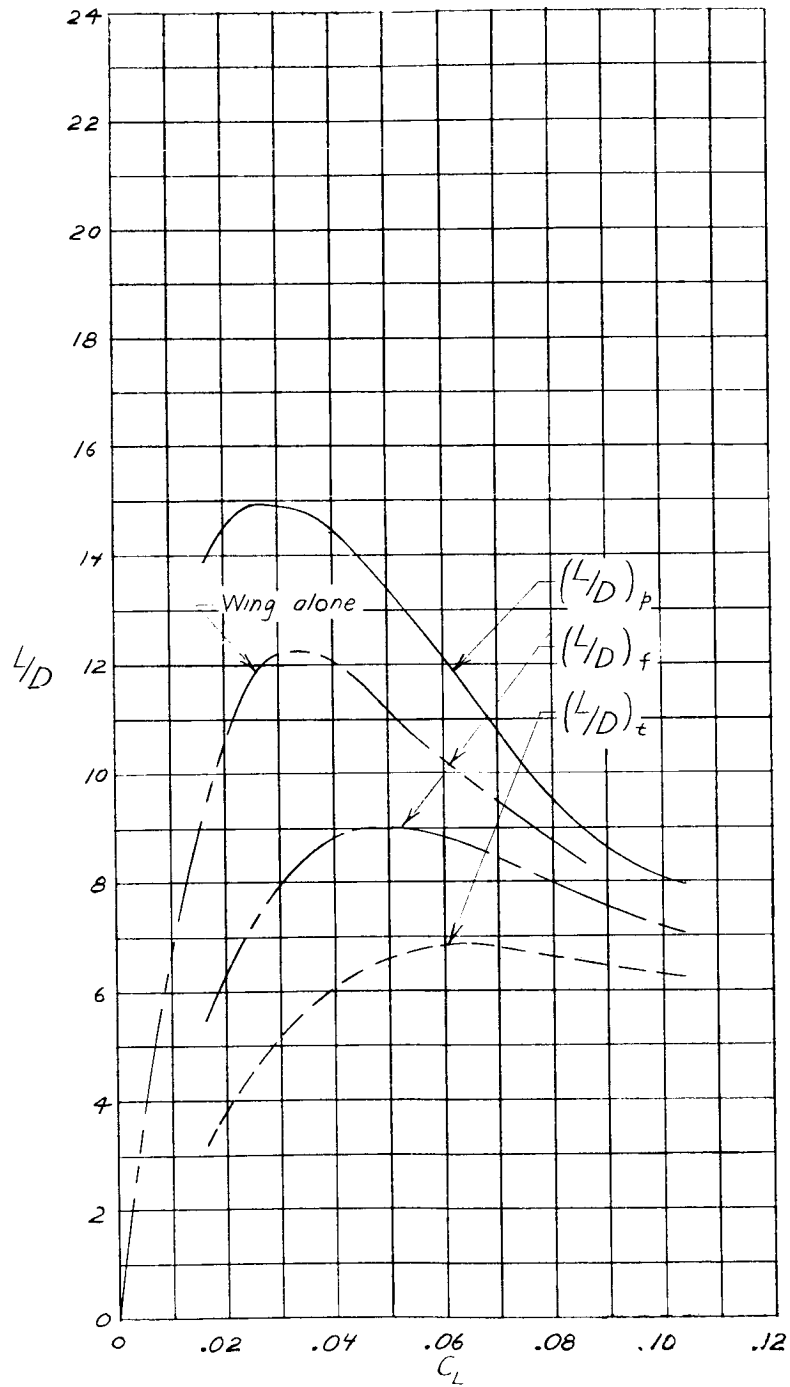


(j) Body 10.

Figure 20.- Continued.

CONFIDENTIAL

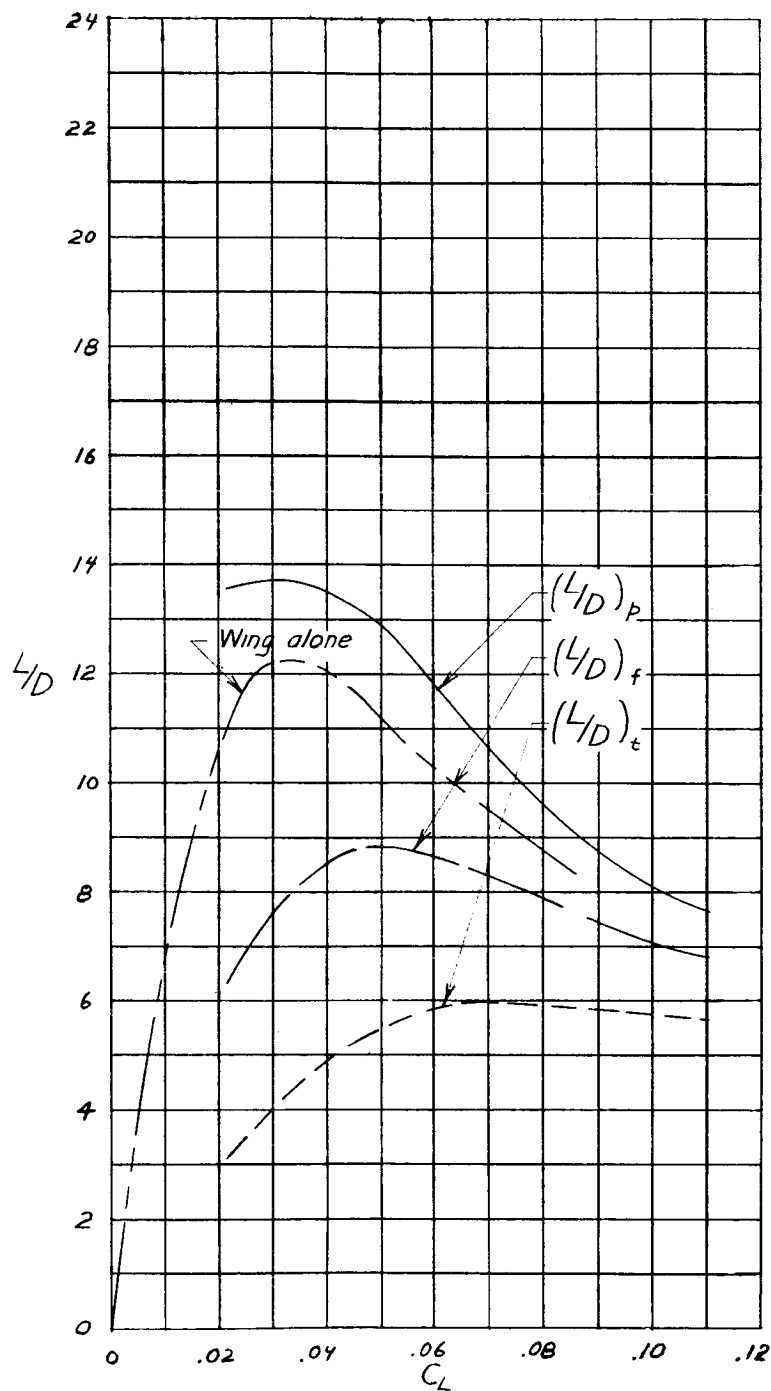
CONFIDENTIAL



(k) Body 11.

Figure 20.- Continued.

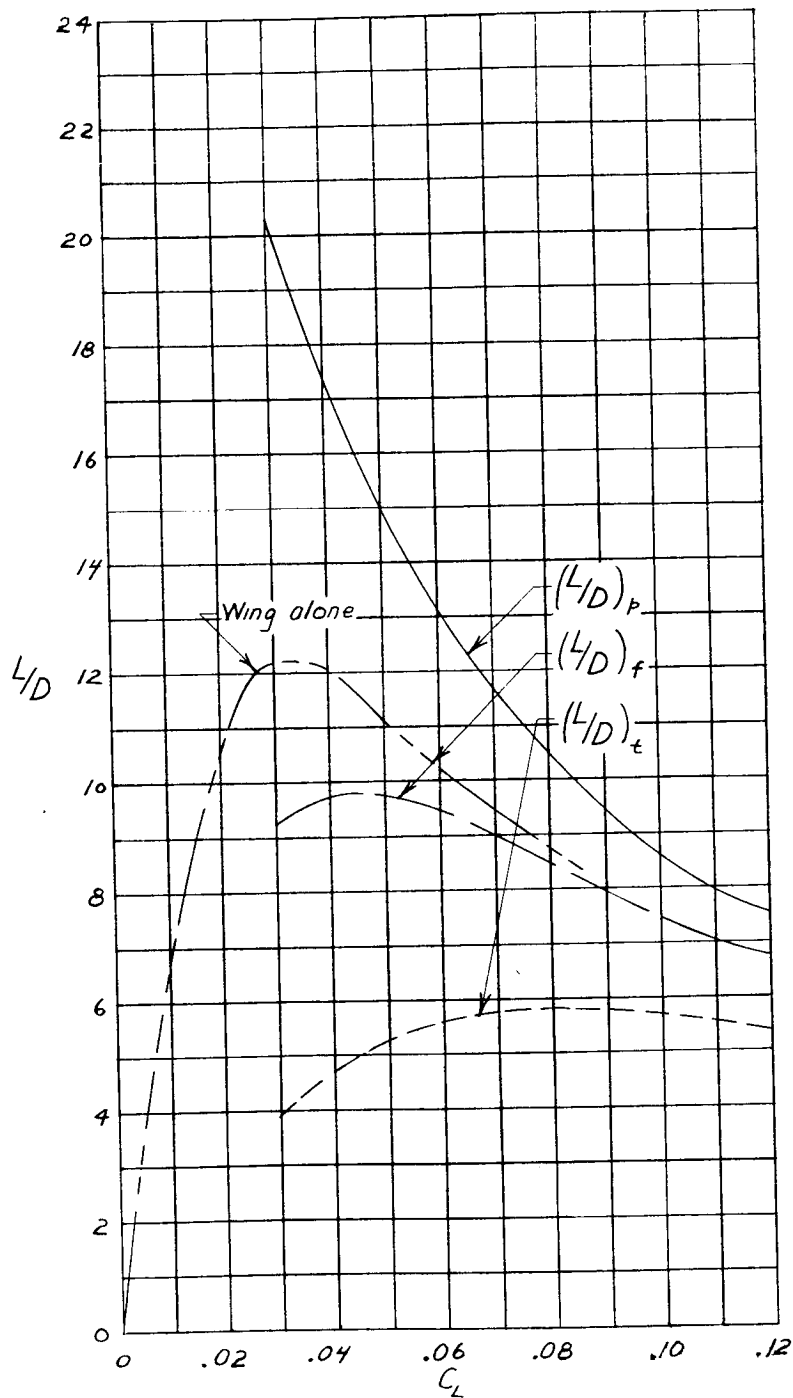
CONFIDENTIAL



(1) Body 12.

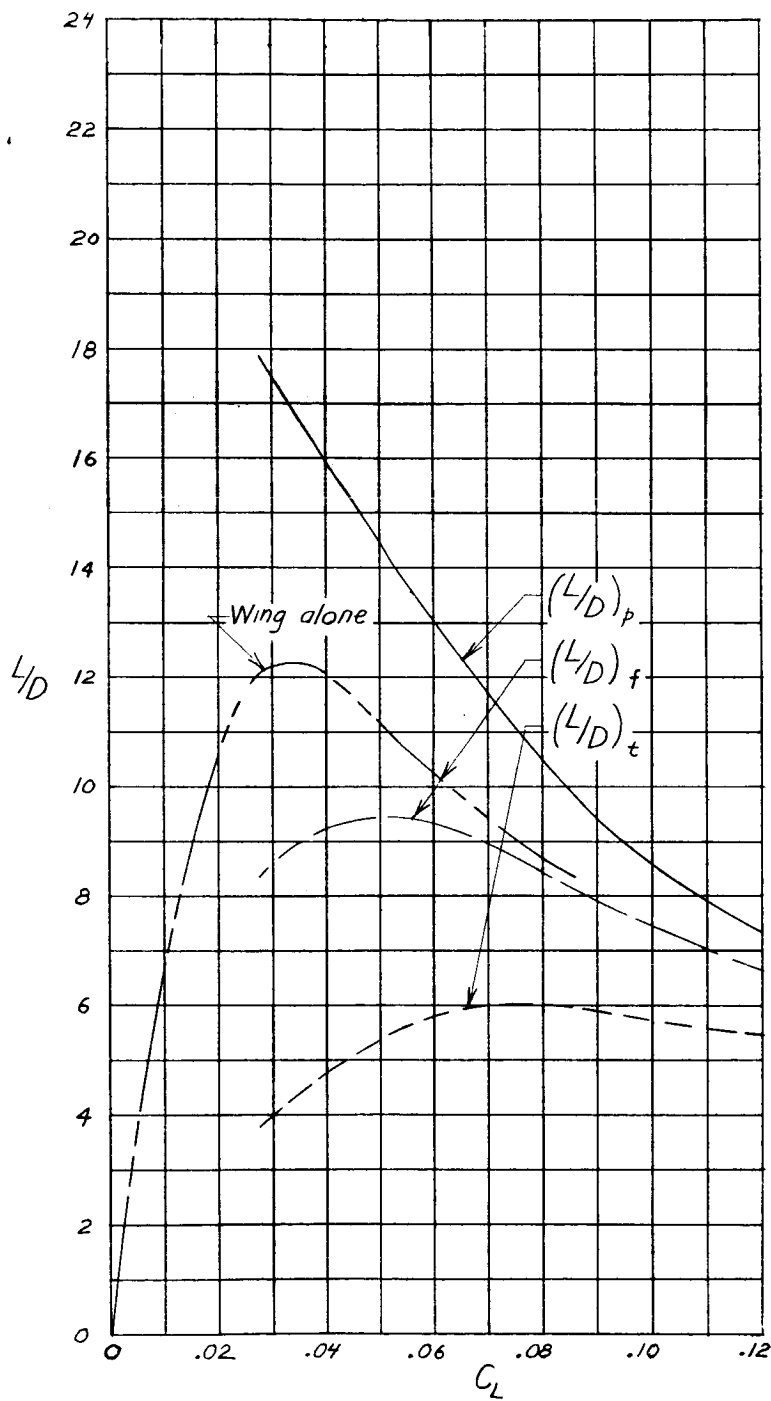
Figure 20.- Continued.

CONFIDENTIAL



(m) Body 13.

Figure 20.- Continued.



(n) Body 14.

Figure 20.- Concluded.

CONFIDENTIAL

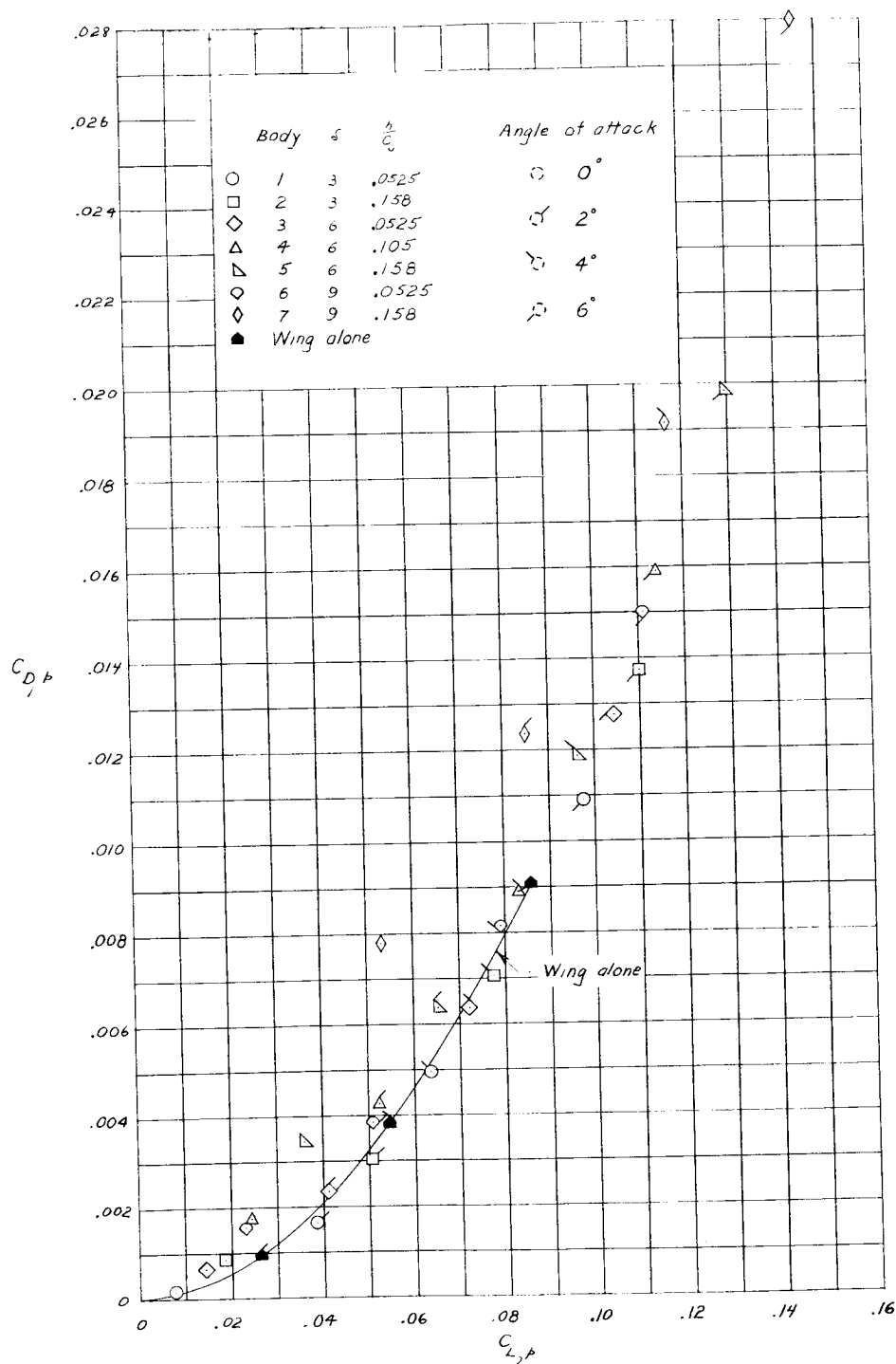


Figure 21.- Comparison of pressure forces of wing-alone and wing-body configurations. Upper wing surface not considered.

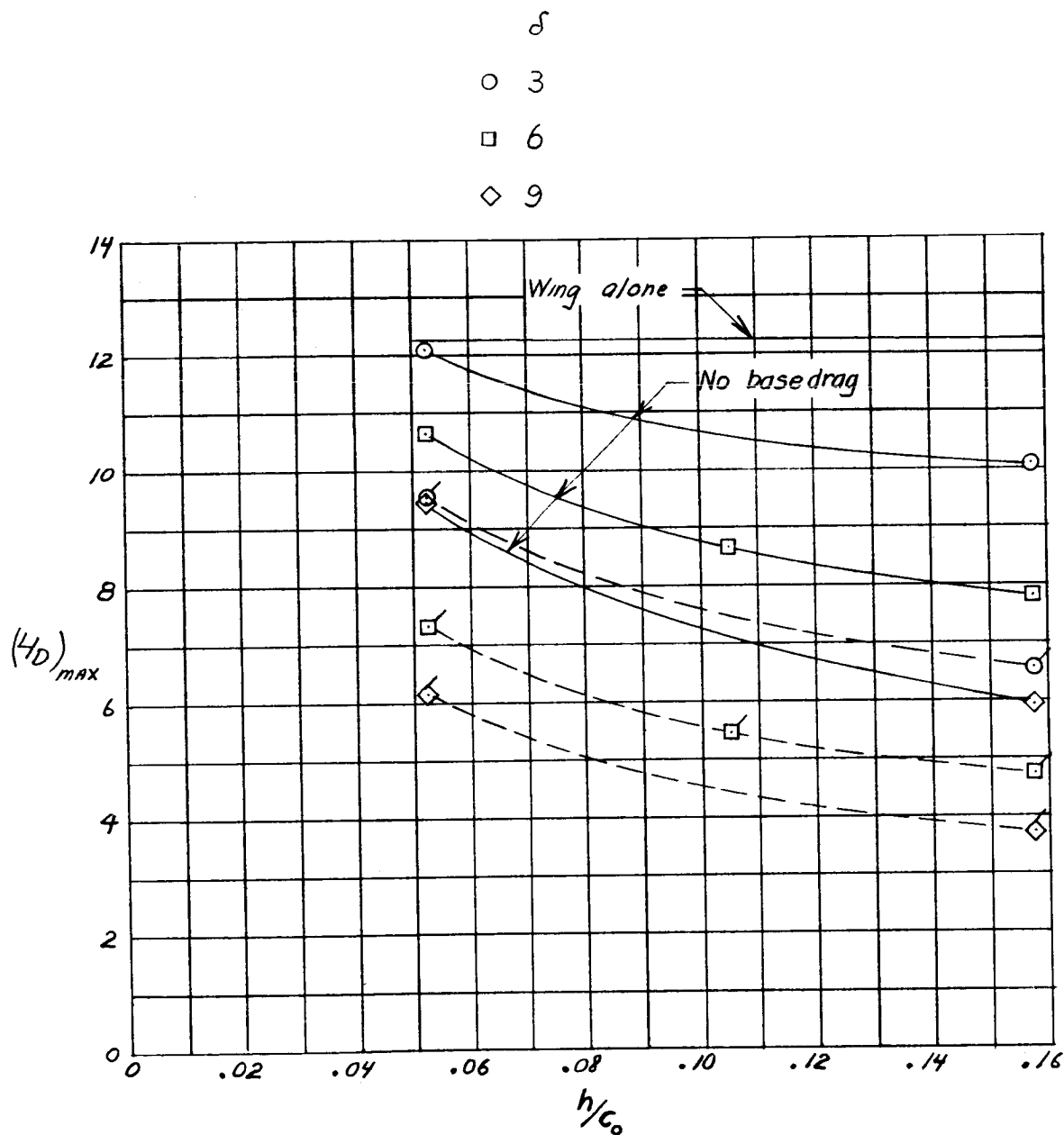


Figure 22.- Effect of wedge half-angle, body height, and base pressure on maximum lift-drag ratio of wing-body configurations 1 and 7. $C_f = 0.0013$. Upper wing surface not considered.

03710281030
CONFIDENTIAL

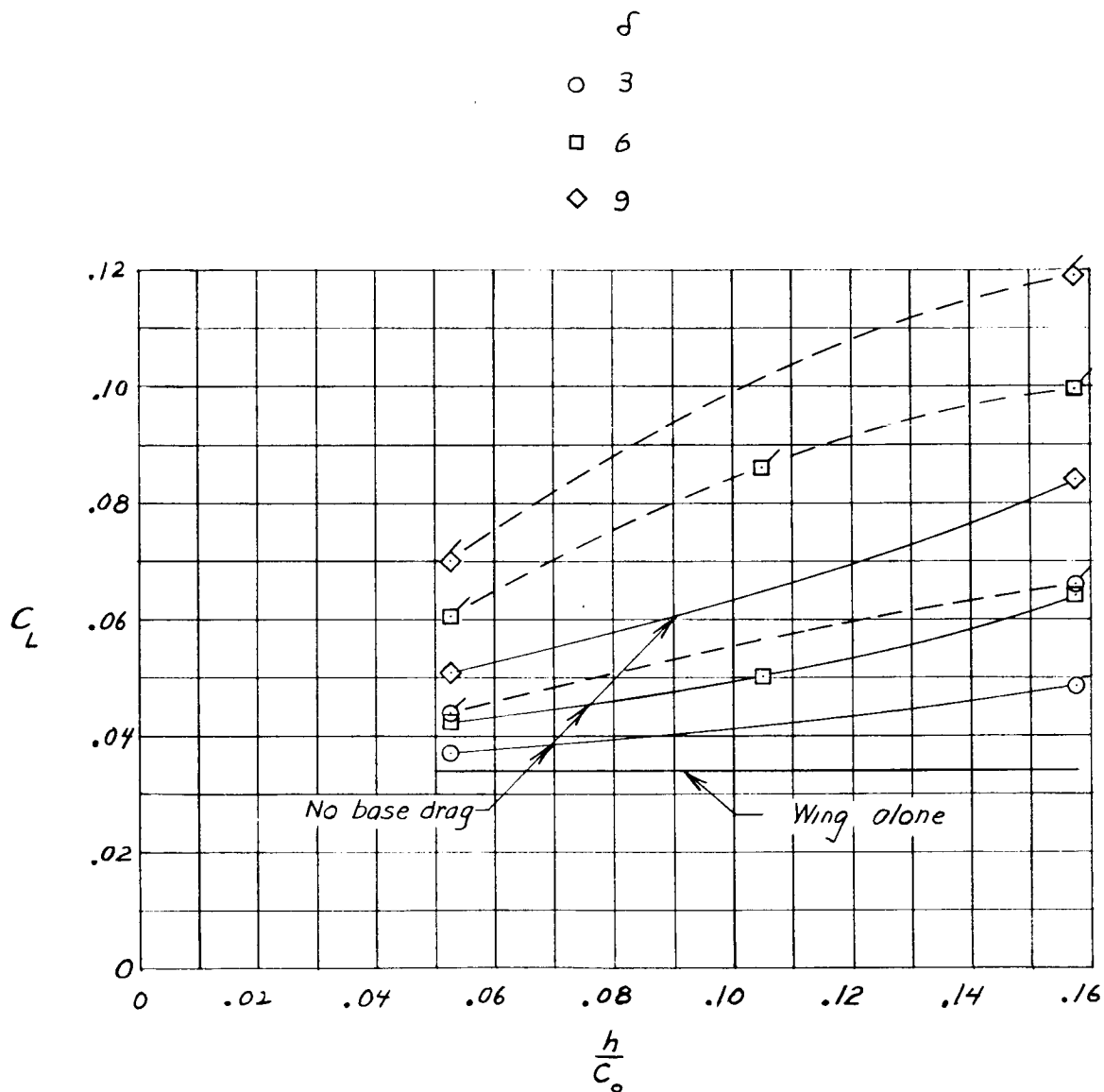


Figure 23.- Effect of wedge half-angle, body height, and base pressure on lift coefficient at maximum lift-drag ratio of wing-body configurations 1 to 7. $C_F = 0.0013$. Upper wing surface not considered.

	Body	δ	$\frac{h}{C_0}$	Air flow
○	3	6	.0525	No
□	8	6	.0525	Yes
◇	4	6	.105	No
△	9	6	.105	Yes

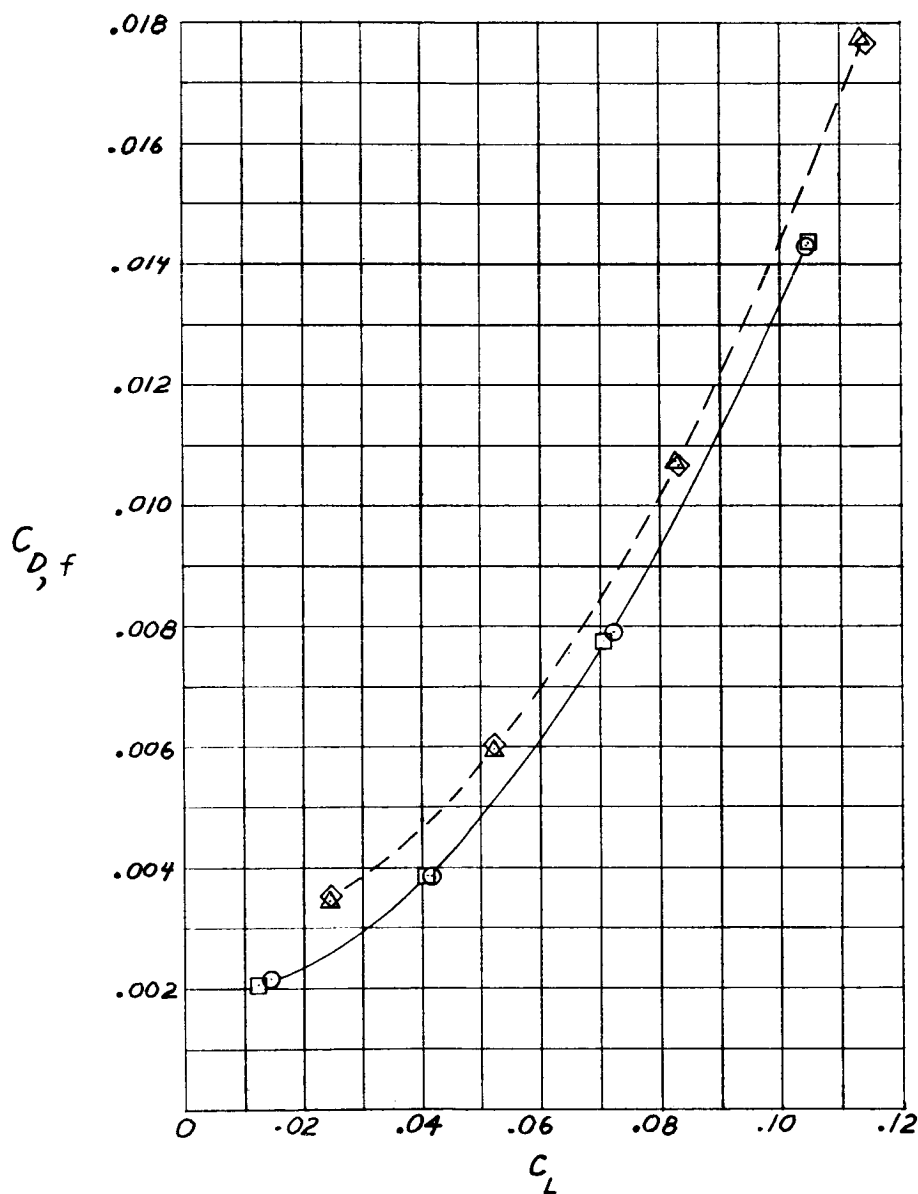


Figure 24.- Effect of air flow on force characteristics of wing-body configurations. Upper wing surface not considered.

CONFIDENTIAL

	Body	Edge shape	h/c_o
—————	4	Square	.105
—— ———	13	Circular	.120
- - - - -	14	Elliptical	.112

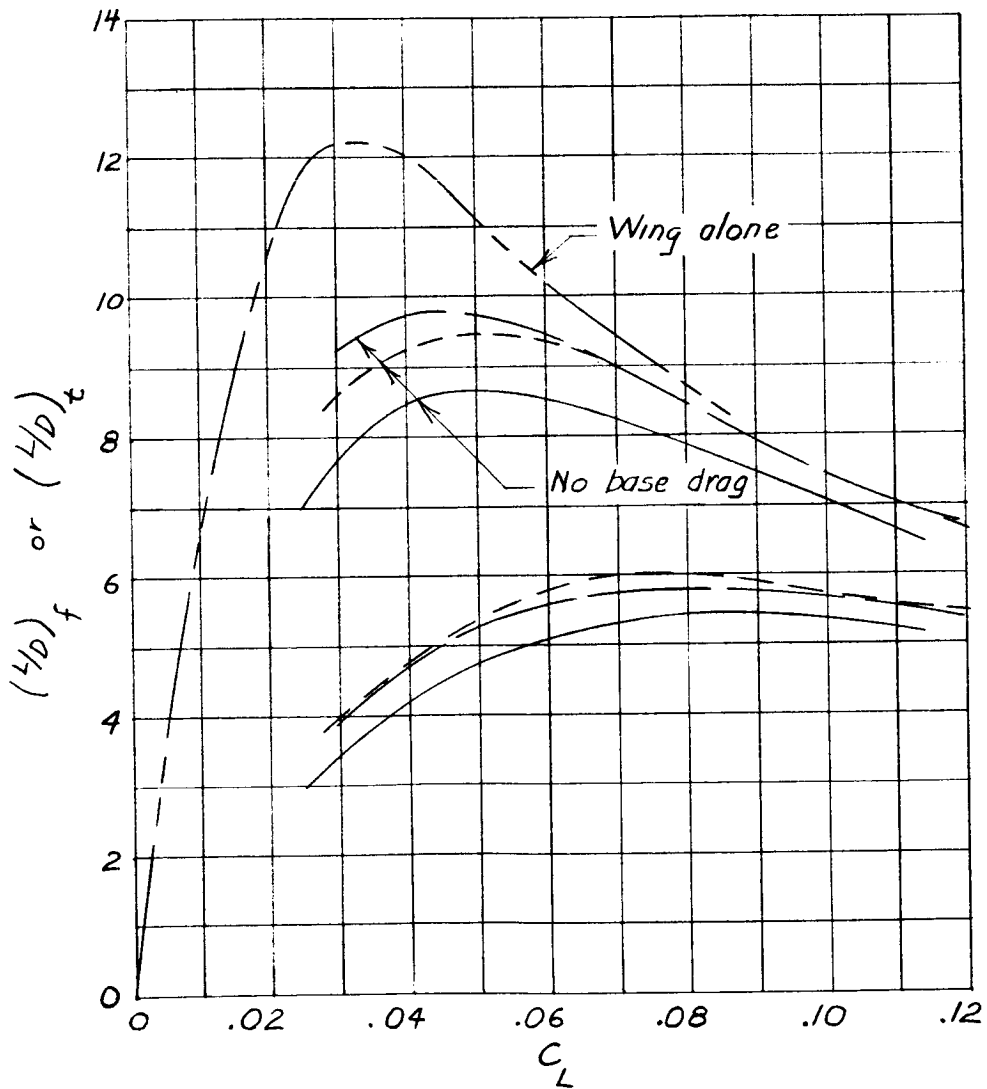
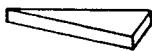


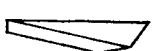



Figure 25.- Effect of edge-shape modifications on force characteristics of configuration 4. $C_f = 0.0013$. Upper wing surface not considered.

CONFIDENTIAL

	Body	δ	$\frac{h}{C_o}$	
————	4	6	.105	
- - - - -	12	6	.105	
— · — · —	11	6	.105	
- - - - -	10	6	.105	
·· — · —	13	6	.105	

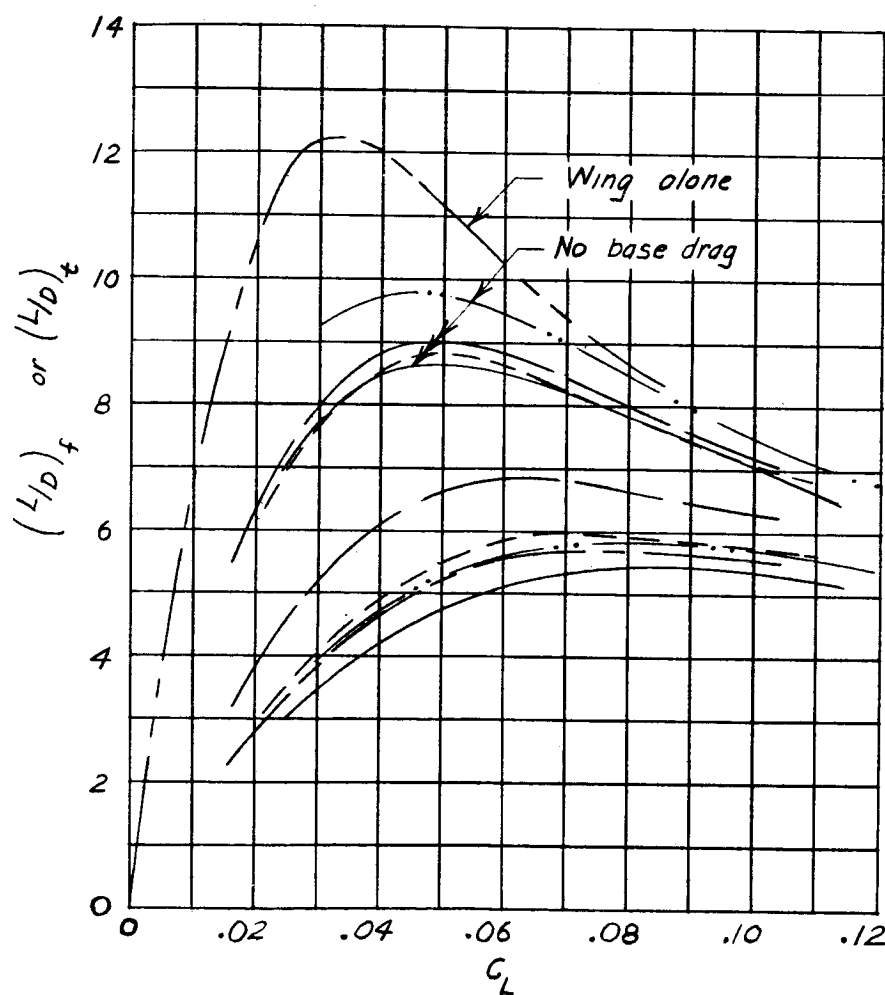


Figure 26.- Effects of various modifications to basic body 4 on maximum lift-drag ratio. Upper wing surface not considered. $C_f = 0.0013$.

CONFIDENTIAL

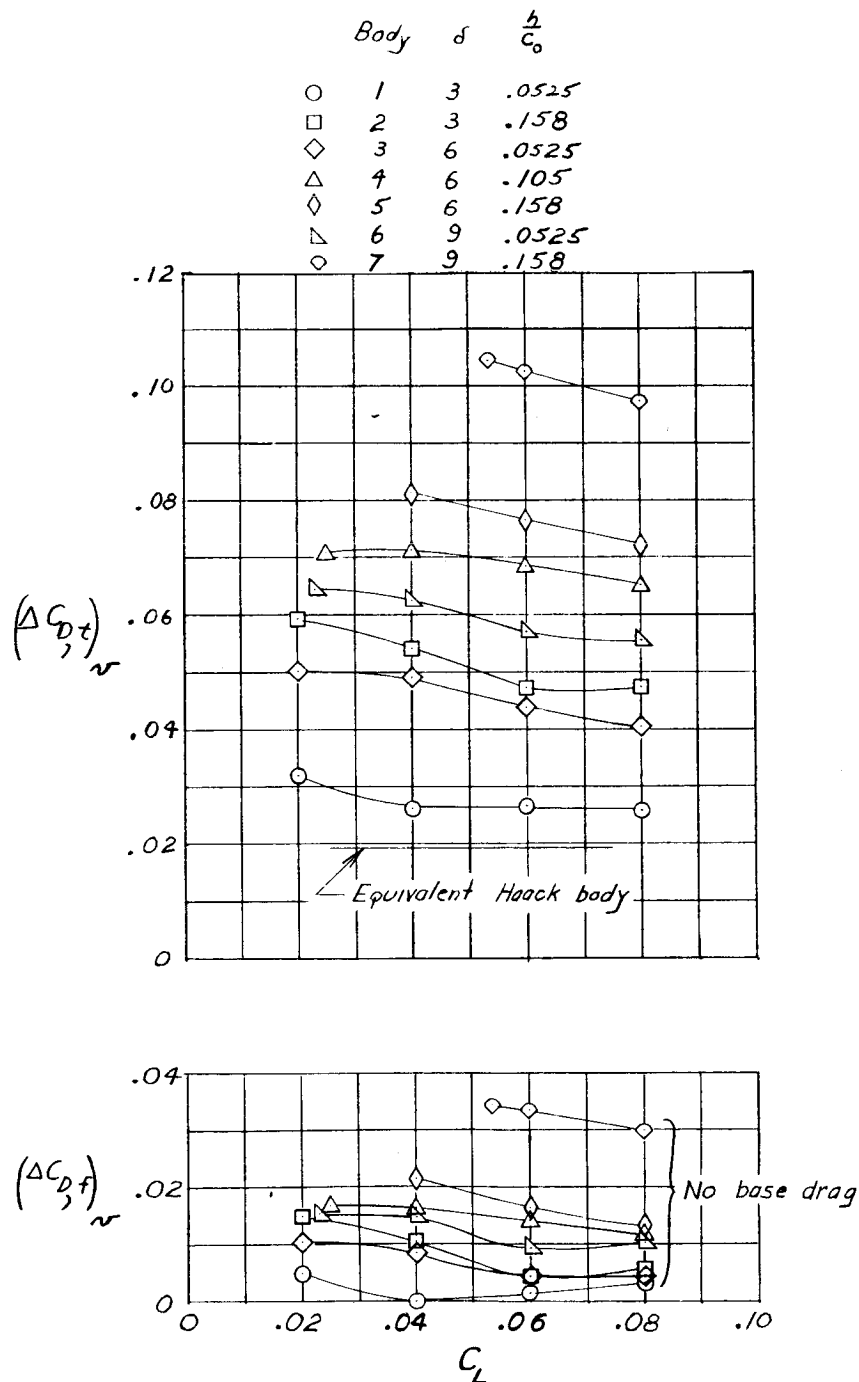
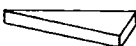


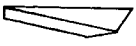
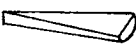


Figure 27.- Effect of body height and half-angle on the incremental volume-drag coefficients of basic body configurations. Upper wing surface not considered.

○ —————	4	6	.105	
◇ - - - - -	12	6	.105	
□ —————	11	6	.105	
△ - - - - -	10	6	.105	
▽ .. ———	13	6	.105	

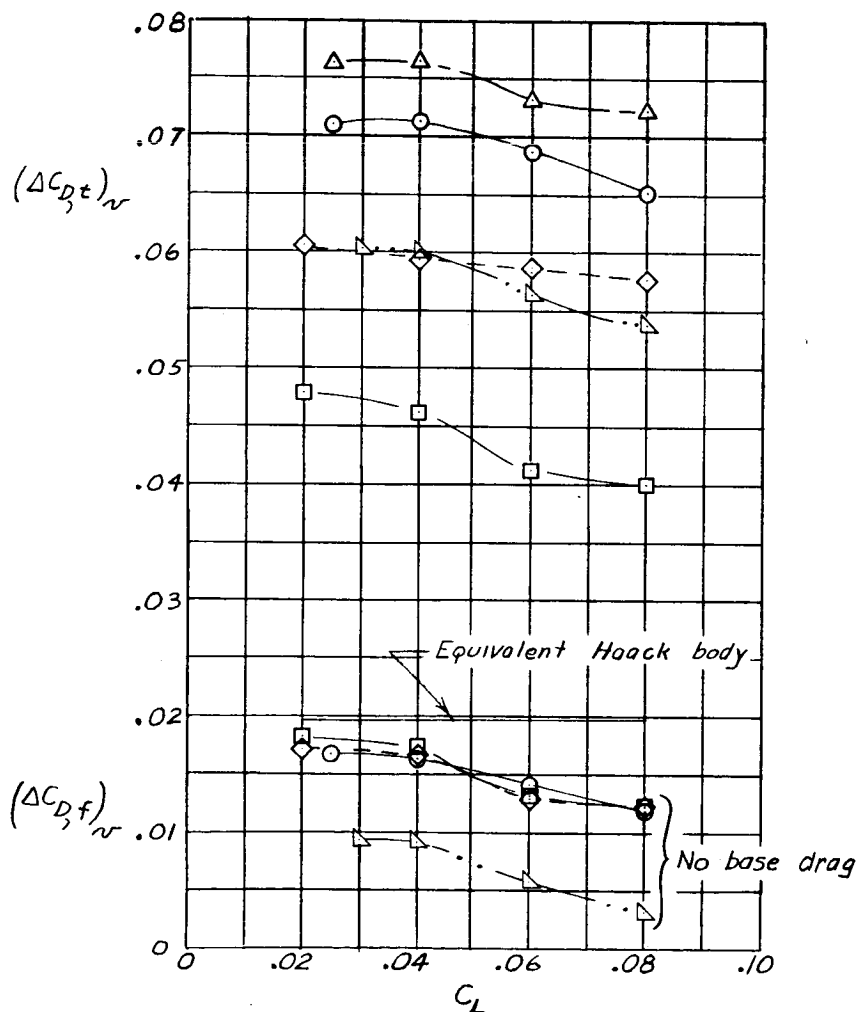

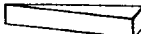

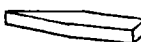




Figure 28.- Effects of various body modifications on the incremental volume drag coefficients of several configurations. Upper wing surface not considered.

CONFIDENTIAL

		δ	$\frac{h}{c_o}$	Body	
	○	3	.158	2	
	□	6	.105	11	
	◇	9	.0525	6	

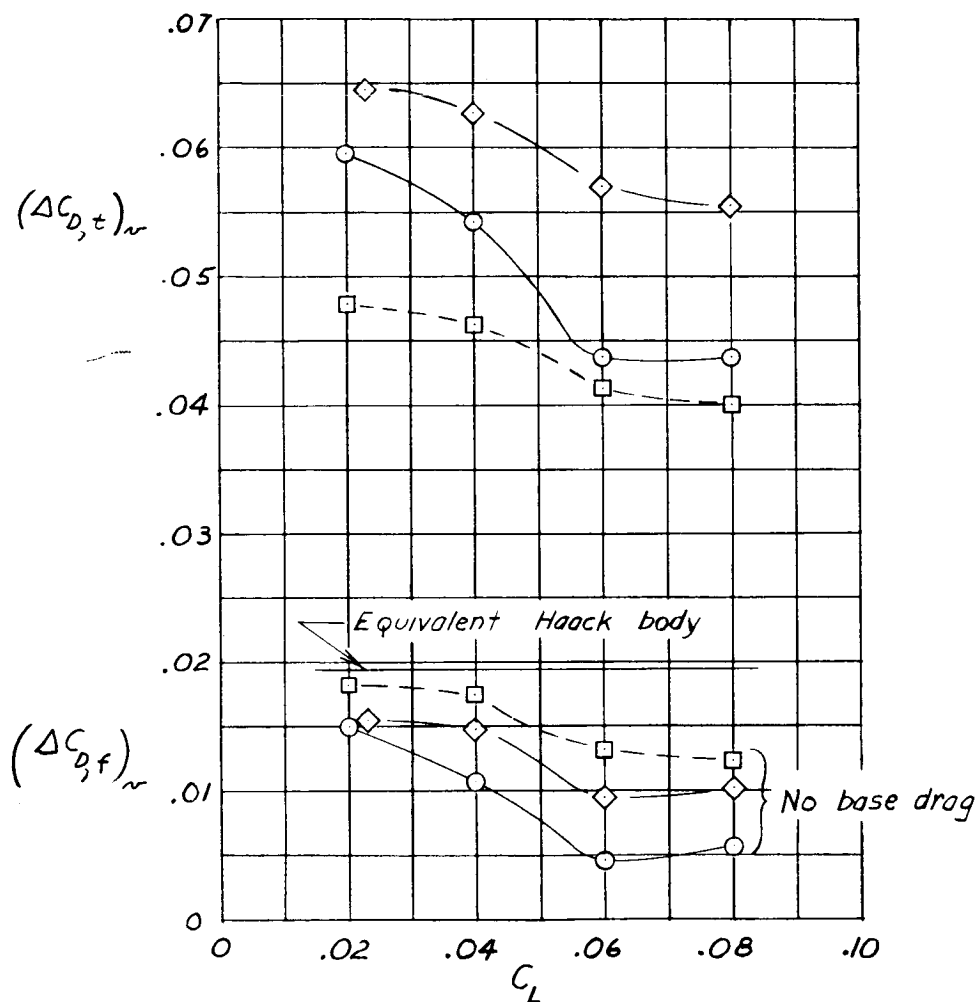


Figure 29.- Incremental volume-drag coefficients of three configurations with bodies of equal volume. Upper wing surface not considered.